A FEASIBILITY STUDY ON THE EFFECT OF AN AL-C MASTER ALLOY ON THE MICROSTRUCTURE AND MECHANICAL PROPERTIES OF THE B319 CAST ALUMINUM ALLOY

by

Levi Charles Lafortune

BASc., The University of British Columbia, 2016

A THESIS SUBMITTED IN PARTIAL FULFILLMENT OF
THE REQUIREMENTS FOR THE DEGREE OF
MASTER OF APPLIED SCIENCE

in

THE COLLEGE OF GRADUATE STUDIES

(Mechanical Engineering)

THE UNIVERSITY OF BRITISH COLUMBIA

(Okanagan)

May 2019

The following individuals certify that they have read, and recommend to the college of graduate studies for acceptance, a thesis entitled:

A FEASIBILITY STUDY ON THE EFFECT OF AN AL-C MASTER ALLOY ON THE MICROSTRUCTURE AND MECHANICAL PROPERTIES OF THE B319 CAST ALUMINUM ALLOY

submitted by Levi Charles Lafortune in partial fulfillment of the requirements of

the degree of MASTER OF APPLIED SCIENCE

Dr. Lukas Bichler, School of Engineering

Supervisor

Dr. Dimitry Sediako, School of Engineering

Supervisory Committee Member

Dr. Abbas Milani, School of Engineering

Supervisory Committee Member

Dr. Liwei Wang, School of Engineering

University Examiner

ABSTRACT

Aluminum alloys have a high strength to weight ratio (x2 of most steel alloys) and are therefore excellent candidates for use in dynamic weight-sensitive designs (e.g. the aerospace, marine, and automotive industries). The B319 aluminum alloy is currently used in complex cast automotive parts, such as the engine block or cylinder head, due to its excellent castability and heat treatability. Improvements to the B319 alloy's strength and casting characteristics can lead to further weight reduction of parts, which translates to improved vehicle efficiency, lower cost, and reduced green house gas emissions. Grain refinement is a method of increasing material properties without significantly altering the parent alloy. However, production of well dispersed and consistent master alloys to achieve effective grain refinement remains an industrial challenge.

This research investigated the effectiveness of a novel Aluminum(Al)-Carbon(C) master alloy for grain refinement of the B319 alloy. The master alloys were synthesized via the spark plasma sintering (SPS) powder metallurgy process, and subsequently characterized by microstructural analysis. Casting experiments were then carried out with the B319 alloy, and the resultant as-cast materials were analyzed.

The results showed that a well dispersed Al-C master alloy could be synthesized by SPS, with carbon black powder equally distributed at the aluminum particle boundaries. The carbon was seen to diffuse at the Al-C interface at sintering temperatures of <500°C. Low concentration (1wt% C) and high concentration (2wt% C) master alloys were added to B319 alloy castings at 0.03wt% total C content. Thermal analysis and microscopy showed no change in the solidification reactions, solidification profiles, or microstructure of the B319 alloy after master alloy addition. Grain size evaluation showed a maximum grain size decrease of 17% when a high concentration master alloy was used. Mechanical and fluidity tests further showed either no improvement or marginal property decreases associated with Al-C addition.

LAY SUMMARY

The B319 aluminum alloy is a popular alloy used in automotive metal-casting applications, such as the manufacturing of engine blocks. If the strength of this alloy can be further improved, automotive producers will be able to make lighter parts and therefore make more fuel efficient, cheaper, and environmentally friendly vehicles.

This research focused on the production of an additive that could be mixed into the molten B319 alloy immediately before casting, which would lead to potential strengthening or general improvement of the metal's characteristics. Experiments were performed and then studies were done to evaluate differences in the samples with additives versus the plain cast B319 alloy samples. Results showed that the trial additive was unable to produce any significant beneficial effects; however, the research brought up additional questions and areas of further research that may lead to a better understanding or strengthening of the B319 alloy in the future.

PREFACE

This research thesis titled “A feasibility study on the effect of an Al-C master alloy on the microstructure and mechanical properties of the B319 cast aluminum alloy” was written for the partial fulfillment of the Masters of Applied Science (MASc) degree at the University of British Columbia.

The contributions from the author and other collaborators are listed below:

Spark plasma sintering (SPS) and powder mixing experiments were carried out in the SPS laboratory at the University of British Columbia Okanagan (UBCO) in Kelowna, BC, Canada by Levi Lafortune with assistance from Anil Prasad. Metal casting experiment were carried out in the metal casting laboratory at UBCO by Levi Lafortune with assistance from Justin Mok, Anil Prasad, and Tyler Davis. Sample preparation for microscopy (cutting, mounting, and polishing) was carried out in the metallurgical laboratory at UBCO by Levi Lafortune. Metallographic surface etching was carried out in the metallurgical laboratory at UBCO by Levi Lafortune with assistance from Justin Mok, Anil Prasad, and under the supervision of Michelle Tofteland. Machining of tensile and Charpy samples was carried out in the machine and weld shop at UBCO by Levi Lafortune with assistance from Anil Prasad, Sebastian Lemus Fonseca, and Kris Mackowiak, while under the supervisor of Durwin Bossy and Raymond Seida. Fabrication of the fluidity mold was done in the machine and weld shop at UBCO by Justin Mok with assistance from Levi Lafortune. Scanning electron microscopy (SEM) and energy-dispersive X-ray spectroscopy (EDXS) analysis was carried out in the Charles Fipke SEM laboratory at UBCO by Levi Lafortune with assistance from Dr. Mathew Smith and under the supervision of David Arkinstall and Dr. Mark Button. X-ray powder diffraction (XRD) was carried out in the XRD laboratory at the University of British Columbia Vancouver (UBCV) in Vancouver, BC, Canada by Anita Lam. Optical microscopy, grain size measurements, and fluidity measurements were carried out in the metallurgical laboratory at UBCO by Levi Lafortune. Tensile and Charpy testing was carried out in the high-head laboratory at UBCO by Levi Lafortune with assistance and supervisor from Alec Smith and Kim Nordstrom. Microhardness testing was carried out in the Survive & Thrive Applied Research (STAR) centre at UBCO by Levi Lafortune. All other experimental measurements and preparations were made in the metallurgical laboratory at UBCO by Levi Lafortune. Manuscripts for this thesis were compiled and written by Levi Lafortune under the supervision of Dr. Lukas Bichler. Manuscripts for partially or fully published results related to this work (noted in the next paragraph) were co-authored with Anil Prasad, Justin Mok, and Dr. Lukas Bichler.

The following is a list of publications, submissions, or conference presentations arising from or related to work in this thesis:

- A. Prasad, L. Lafortune, J. Mok, and L. Bichler (2019). An Investigation on Spark Plasma Sintering of a Carbon Black Grain Refiner for B319 Aluminum Alloy, Transactions of Indian Institute of Metallurgy, February 2019, pp 1-5.
  DOI: https://doi.org/10.1007/s12666-019-01573-8
- A. Prasad, L. Lafortune, J. Mok, and L. Bichler (2018). An Investigation on Spark Plasma Sintered Carbon Black Grain Refiner for B319, International Conference on Advanced Materials and Manufacturing Process for Strategic Sectors (ICAMPS 2018), Trivandrum, India, October 2019.
  DOI: 10.13140/RG.2.2.22120.11520.

All copyrighted images contained in this thesis are reprinted with permission of the copyright owner. These are:

- Figure 2.1: The University of Cambridge, “Phase Diagrams,” 2018. [Online]. Available: https://www.doitpoms.ac.uk/miclib/phase_diagrams.php. [Accessed: 22-May-2018].
- Figure 2.2: D. S. MacKenzie and G. E. Totten, *Analytical Characterization of Aluminum, Steel and Superalloys*. CRC Press (Taylor & Francis Group), 2006.
- Figure 2.4: The University of Cambridge, “Phase Diagrams,” 2018. [Online]. Available: https://www.doitpoms.ac.uk/miclib/phase_diagrams.php. [Accessed: 22-May-2018].
- Figure 2.5: F. C. Robles-hernandez, J. M. Herrera Ramírez, and R. Mackay, *Al-Si Alloys: Automotive, Aeronautial, and Aerospace Applications*. Springer International Publishing, 2017.
- Figure 2.6: M. Tash, F. H. Samuel, F. Mucciardi, and H. W. Doty, “Effect of metallurgical parameters on the hardness and microstructural characterization of as-cast and heat-treated 356 and 319 aluminum alloys,” *Mater. Sci. Eng. A*, vol. 443, no. 1–2, pp. 185–201, 2007.
- Figure 2.7: K. P. Shah, “Practical Maintenance: Crystallization.” [Online]. Available: http://practicalmaintenance.net/?p=1085. [Accessed: 15-Jun-2018].
- Figure 2.8: W. D. J. Callister and D. G. Rethwisch, *Material Science and Engineering An Introduction*, 9th ed. Wiley, 2014.
- Figure 2.9: W. D. J. Callister and D. G. Rethwisch, *Material Science and Engineering An Introduction*, 9th ed. Wiley, 2014.

- Figure 2.10: International Carbon Black Association, “Carbon Black User’s Guide,” *International Carbon Black Association*. p. 36, 2016.
- Figure 2.11: A. Prasad, “Spark Plasma Sintering of Cerium Dioxide and its Composites,” The University of British Columbia Okanagan, 2017.
- Figure 2.12: Z. Fu *et al.*, “The SPS Process : Characterization and Fundamental Investigations,” in *Pulse Electric Current Synthesis and Processing of Materials*, Z. A. Munir, M. Ohyanagi, and M. Tokita, Eds. The American Ceramics Society, 2006, pp. 3–21.

TABLE OF CONTENTS

LIST OF TABLES

LIST OF FIGURES

LIST OF EQUATIONS

LIST OF ABBREVIATIONS

AH	Alpha Aesar carbon black high concentration master alloy
AL	Alpha Aesar carbon black low concentration master alloy
ASTM	American Society for Testing and Materials
BCC	Body-centred cubic
BCT	Body-centred tetragonal
CC	Cold casting
CS	Conventional sintering
CNC	Computer numerical control
DAQ	Data acquisition
DAS	Dendritic arm spacing
DC	Direct current
DCP	Dendritic coherency point
DMF	Dimethylformamide
DSC	Differential scanning calorimetry
EDXS	Energy-dispersive X-ray spectroscopy
FCC	Face-centred cubic
GGE	Green house gas emissions
GRF	Growth restriction factor
HP	Hot pressing
HPSC	High precision sand casting
PAl	Pure aluminum master alloy

PECAS	Pulsed electric current assisted sintering
PM	Powder metallurgy
RH	Recycled carbon black high concentration master alloy
RL	Recycled carbon black low concentration master alloy
SDAS	Secondary dendritic arm spacing
SEM	Scanning electron microscope/microscopy
SPS	Spark plasma sintering
TA	Thermal analysis
UBCO	University of British Columbia, Okanagan Campus
UBCV	University of British Columbia, Vancouver Campus
XRD	X-ray powder diffraction

LIST OF SYMBOLS

%	Percent
at%	Atomic weight percentage
wt%	Weight percent / percentage by weight
MPa	Mega-pascals
HB	Brinell hardness
GPa	Giga-pascals
°C	Degrees Celsius
ΔG	Change in free energy
r (or R)	Radius
G_V	Gibbs free energy per unit volume
γ	Gibbs free energy per unit area
T	Temperature
T_M	Melting temperature
γ_{S-L}	Solid-liquid interfacial energy
γ_{S-I}	Solid-interface interfacial energy
γ_{I-L}	Interface-liquid interfacial energy
θ	Angle in degrees
nm	Nano-meter
ppm	Parts per million
dT	Change in temperature
dt	Change in time

mm	Milli-meter
g	Gram
"	Inch
OD	Outer diameter
ID	Inner diameter
H	Height
Ø	Diameter
min	Minute
s	Second
Hz	Hertz
W_H	Weight of master alloy high concentration
W_{B319}	Weight of the B319 alloy
W_L	Weight of master alloy low concentration
mm^2	Square millimeters
kg	Kilogram
N	Newton
HV	Vickers hardness
ft*lbs	Foot pounds
g/cm^3	Grams per cubic centimeter
t	Time (seconds in this work)
T_L	Liquidus temperature
T_S	Solidus temperature

$T_{N\ \alpha\text{-Al}}$	Temperature of nucleation for the α-Al phase
$T_{G\ \alpha\text{-Al}}$	Temperature of growth for the α-Al phase
T_{UC}	Temperature of undercooling
$t_{G\ \alpha\text{-Al}}$	Time of growth for the α-Al phase
$T_{N\ Al\text{-}Si}$	Temperature of nucleation for the Al-Si region
$T_{G\ Al\text{-}Si}$	Temperature of growth for the Al-Si phase
$t_{G\ Al\text{-}Si}$	Time of growth for the Al-Si phase
$T_{N\ Al\text{-}Cu}$	Temperature of nucleation for the Al-Cu region
$T_{G\ Al\text{-}Cu}$	Temperature of growth for the Al-Cu phase
FR	Freezing range
t_S	Total solidification time
CR	Cooling rate
T_{DCP}	Temperature at the dendritic coherency point
$f_{S,\ DCP}$	Fraction solid at the dendritic coherency point
GS	Average sample grain size
D	Diameter
N_i	Number of total grain intercepts per intercept circle
kV	Kilovolt
mA	Milliamp
vol%	Percentage by volume
R^2_{Adj}	Adjusted coefficient of determination

LIST OF ELEMENTS AND INTERMETALLICS

Al	Aluminum
$Al_2Mg_3Zn_3$	Aluminum-magnesium-zinc intermetallic
Al_2MgC_2	Aluminum-magnesium-carbon intermetallic
Al_2OC	Aluminum oxycarbide
Al_3CuNi	Aluminum-copper-nickel intermetallic
Al_3Fe	Aluminum-iron intermetallic
Al_3Ni	Aluminum-nickel intermetallic
Al_4C_3	Aluminum carbide
$Al_5Cu_2Mg_8Si_6$	Aluminum-copper-magnesium-silicon intermetallic
AlB_2	Aluminum boride
AlO(OH)	Aluminum oxide hydroxide
π-$Al_8Mg_3FeSi_6$	π-phase aluminum-magnesium-iron-silicon intermetallic
α'-Al	Proeutectic aluminum
α-$Al_{15}(Fe,Mn,Cr)_3Si_2$	α-phase aluminum-iron-silicon intermetallic
α-Al_8Fe_2Si	α-phase aluminum-iron-silicon intermetallic
β-Al_5FeSi	β-phase aluminum-iron-silicon intermetallic
B	Boron
C	Carbon
CO_2	Carbon dioxide
Cr	Chromium
Cu	Copper

$CuAl_2$	Copper aluminide
Fe	Iron
H_2	Hydrogen
HCl	Hydrochloric acid
HF	Hydrofluoric acid
HNO_3	Nitric acid
Mg	Magnesium
Mg_2Si	Magnesium silicide
$MgZn_2$	Dizinc magnesium
Mn	Manganese
Ni	Nickel
Si	Silicon
SiO_2	Silicon dioxide (silica sand)
Ti	Titanium
Ti_3AlC_5	Titanium-aluminum-carbon intermetallic
$TiAl_3$	Titanium aluminide
TiB_2	Titanium boride
TiC	Titanium carbide
$TiSi_2$	Titanium silicide
Zn	Zinc
Zr_2O	Zirconium dioxide

ACKNOWLEDGEMENTS

I would like to first express my genuine gratitude to my supervisor, Dr. Lukas Bichler. Thank you Dr. Bichler for your support and guidance throughout this project. You have the invaluable trait of making all your students feel respected and listened to, which each and everyone of us deeply appreciates. Your calm and optimistic manner of thinking has been extremely helpful at times where I needed research input or guidance. Thank you for your patience while I have struggled to complete this thesis in a timely matter, among my travels to Asia and departing early to begin my career in industry. Most of all thank you for the opportunity and encouragement to have begun my graduate studies in the first place. The university is lucky to have a you!

I would also like to sincerely thank all the phenomenal technicians and staff at UBCO who help to either facilitate parts of my research or offered great friendships. Durwin, Ray, Praveen, Ryan, Alec, Michelle, David, Mark, Russell, Tim; much of this work would not have been possible without your help and input. More importantly, my time at UBCO would have been much more boring without your company – Thank you!

Last but certainly not least. I must thank all my colleagues from the metallurgical lab group. Over the course of my time at UBCO and in the EME 1205 lab, I had the absolute pleasure of working and socializing with this group. The “High Society Nerdz”.

Siddarth Siddhu, it was a pleasure to get to know you and spend time outside the lab with you.

Kyle Lessoway, thank you for opening your home up along with Kris to have all us over for fun and games. You showed up shortly before I left, and I wish we would have had you in the lab with us earlier.

Mathew Smith, thank you for the time you spent helping me in the SEM lab and for taking the time to help review this thesis, it has been immensely helpful.

Tyler Davis, I like to think of you as the laboratory “jack of all trades”, you know something about almost every piece of equipment in our facility! Thank you for showing me the ropes when I first arrived and for contributing to the fun outside the lab.

Somi Doja, you are always a valuable contributor to our discussions around the lab and tons of fun at the group outings. Thank you for introducing me to true Indian sweets and the UBCO-MSA's awesome cuisine!

Rafael Torres, you have an awesome sense of humour! Thank you for weighing in on some of the discussions around the lab and for helping to make our group get-togethers as much fun as they were.

Kris Mackowiak, I am still amazed that you find the time to do your Ph.D. work amidst bag-pipe shows, violin lessons, piano, etc. You are always learning new things, both in the areas of music and science! Thank you for opening your home for most of our potlucks and gatherings. You make a mean chilli!

Sebastian Lemus-Fonseca, "C-Bass", I truly appreciated the time we were able to spend together working on our vehicles. Thank you for the many great chats, help in the lab, and jokes we shared!

Justin Mok, we spent a lot of time working side-by-side and I thoroughly enjoyed it all. It makes even tedious tasks fun when your laughing and working with good people. Thank you for all the support in the lab and the great discussions related and unrelated to our research!

Anil Prasad, I had a blast shopping for vehicles, working out, and teaming up with you in our AOE brawls. I am so hugely thankful for all the help you gave me on my research, especially near the end stages when we were quite often working late together in the office/lab. Thank you!

To you all: I've never laughed so much and had some much fun doing work. It truly "takes a village" and I feel so fortunate to have had the pleasure of being included in our lab group. It wouldn't have been the same without any of you. Thank you for the life long friendships!

DEDICATION

“ Well here we are!

…Where are we? ”

To my family, who have shaped me into the man I am today.

How blessed I am to have you in my life.

CHAPTER 1: INTRODUCTION

This chapter provides a general introduction to aluminum alloys for the automotive sector. The research objectives and research scope are also summarized at the end of this chapter.

1.1 BACKGROUND

Over the last 60 years, climate change and the reduction of greenhouse gas emissions (GGE) has become an important topic of research, design, and engineering. The reduction of GGE has been highlighted by environmental scientists as an effective way to counteract global human-caused climate change [1]. In 2016, passenger and commercial road vehicles accounted for over 20% of Canada's total GGE [2]. For internal combustion engines, GGE can be reduced by decreasing fuel consumption or by increasing fuel efficiency. An effective way to increase the fuel efficiency of vehicles is by reducing vehicle weight. This can be achieved by replacing heavy steel parts with lighter aluminum alloys.

Aluminum was first introduced into the automotive industry as early as 1895, when inventor and automaker Elwood Haynes first experimented with aluminum as a lighter and more corrosion resistant crank case material [3]. Since then, aluminum alloys have continued to replace steel in automotive component manufacturing, with the aluminum content of vehicles expected to reach nearly 20wt% by 2028 [4], [5]. Aluminum alloys can exhibit strength-to-weight rations twice that of steel, and therefore not only contribute to increased vehicle fuel efficiency, but also increase road safety by lowering the collision forces between vehicles during an accident [6], [7].

Of the many aluminum alloy families, the aluminum alloy B319 has become a popular alloy for cast components, such as the engine block, crank case, or cylinder head. The B319 alloy has been found to be well suited for these applications due to its high degree of castability, heat treatability, high temperature stability, and overall high strength [6]–[8].

To continue reducing vehicle weight and materials manufacturing costs, auto part makers are continually searching for ways to improve the mechanical properties and castability of alloys, such as the B319 alloy (e.g. higher alloy strength and improved fluidity can yield thinner cast cross sections). Although methods such as quenching or heat treatment are known to successfully improve alloy properties, sometimes casting complexity or cost prohibits the use of these technologies. In these circumstances, either a chemical grain refinement or grain

modification, referred to as inoculation, can be used to improve alloy properties without any addition processing stages. Inoculation is the process of adding a small amount of a foreign material to an alloy during the casting process, which works to either arrest grain development (yielding smaller grains) or modify certain intermetallic or eutectic phases (creating stronger intergranular compounds) [6]. Inoculation of aluminum alloys is an area of burgeoning exploration, with a large portion of past research having been successfully adopted into regular industrial practice (e.g. the use of titanium-boride grain refiners) [9]. In recent decades, some research has been conducted on the efficacy of nano-scale and carbon based inoculants in magnesium and aluminum alloys, which saw some positive results and prompts further research [10]–[12].

1.2 RESEARCH OBJECTIVE AND SCOPE

The research objective of this work was to study the effect of carbon inoculation on the B319 alloy. An Aluminum(Al)-Carbon(C) master alloy was fabricated using the spark plasma sintering (SPS) powder metallurgy process and using nano-scale carbon black powder.

To achieve this objective three stages of research, outlined in Figure 1.1, were completed: (i) master alloy synthesis, (ii) casting experiments, and (iii) characterization of as-cast materials. Each of these stages will be further explained in the following chapters.

This document has been organized as follows:

Chapter 2 contains a comprehensive literature review of past and current research on aluminum alloys, the B319 alloy, grain refinement and inoculation, as well as the SPS process. Chapter 3 provides a detailed summary of the research methods used in this thesis, as well as the equipment and materials used. Chapter 4 presents the research results and provides an in-depth discussion on the experimental observations. Finally, Chapter 5 summarizes key conclusions of this research and suggests future work.

The appendices are attached following Chapter 5 and contain supplementary data and figures, referenced in the preceding chapters.

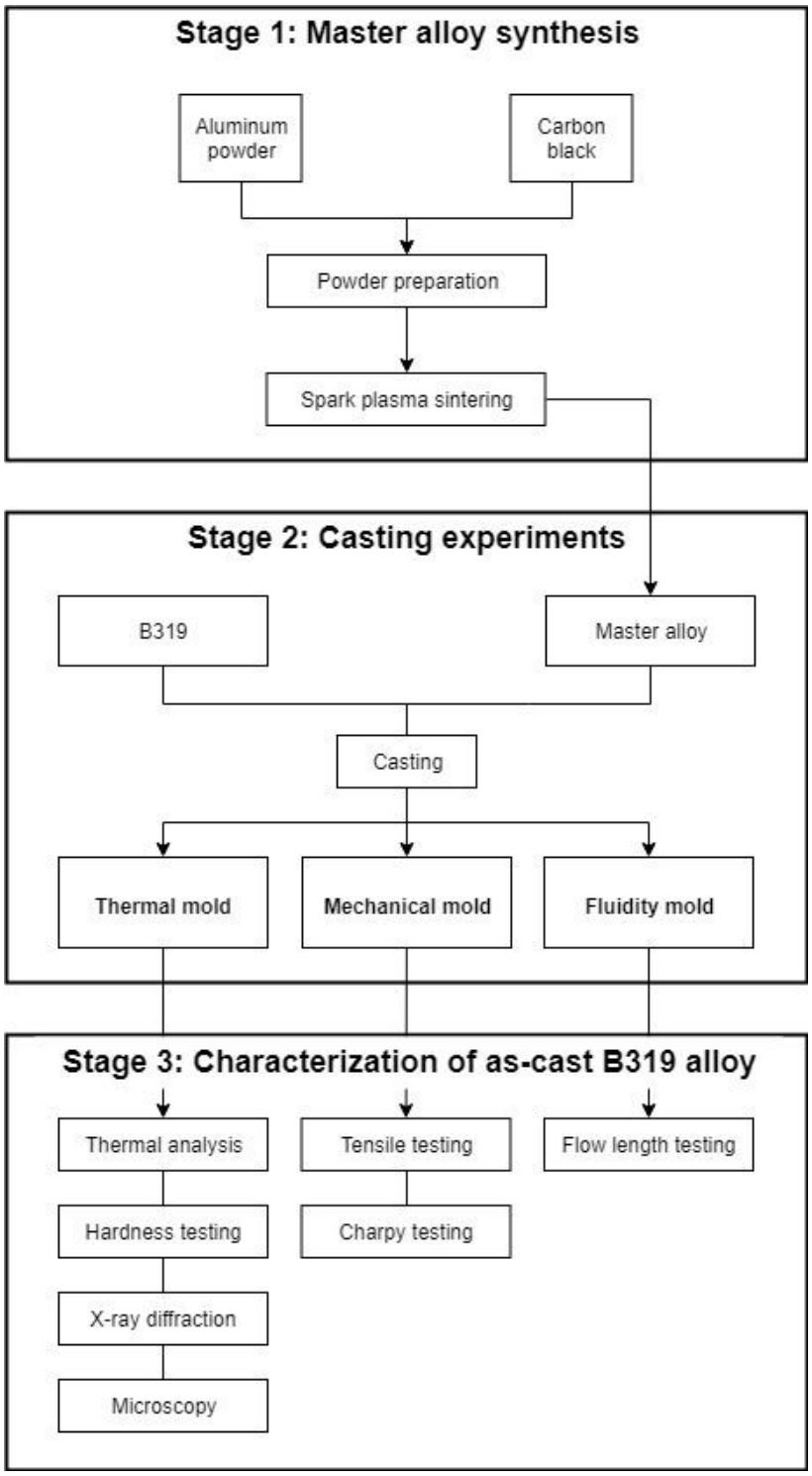

Figure 1.1: Scope of research

CHAPTER 2: LITERATURE REVIEW

This chapter provides a review of published literature relevant to the scope of this thesis: aluminum and aluminum alloys, the B319 alloy, casting of aluminum alloys, solidification and grain refinement, and spark plasma sintering.

2.1 ALUMINUM AND ALUMINUM ALLOYS

Aluminum and its alloys can be designed with a variety of material properties to suit a broad range of engineering applications, spanning from food packaging (Al 1100) to truck frames (Al 6061) [7], [13]. Aluminum is widely popular for static structural applications like furniture frames, as well as dynamic applications such as vehicle parts. This is due to aluminum's high strength-to-weight ratio compared to other materials such as steel [7]. Aluminum is well suited for parts requiring basic corrosion resistance, since it does not readily react and forms a nano oxide layer preventing subsequent oxidation and chemical erosion [7]. Many aluminum alloys also have excellent electrical conductivity, twice that of copper's on an equivalent weight basis, which makes aluminum suitable for electrical applications such as high-voltage power cables (Al 1350) [13]. Other types of industrial aluminum alloys have exceptional thermal conductivity, also nearly twice that of copper's on an equivalent weight basis, making these alloys well suited for engine components and heat exchangers [7], [13]. Furthermore, aluminum and aluminum alloys are generally non-ferromagnetic (important for electronic applications) and non-pyrophoric (crucial for safety applications and explosive or flammable environments) [7], [13].

In addition to the wide range of applications above, one of the alloy family's most desirable qualities from an economic standpoint is its high degree of workability. Aluminum can be easily cast, rolled, stamped, drawn, spun, extruded, hammered, or forged [7], [8], [13], [14]. Depending on the manufacturing process, aluminum alloys can be split into two categories: wrought or cast alloys.

2.1.1 CAST ALLOYS

A cast alloy is melted and then poured into a mold, producing a replica of the mold cavity. With the increased development of molding technology, cast alloys are commonly used for the mass production of high complexity parts to a near-net-shape finish (engine blocks, turbine wheels, tire rims, etc.) [7]. Therefore, ideal casting alloys will have desirable properties such as a low

melting temperatures and a high liquid fluidity [8]. Cast alloys are typically weaker than wrought alloys, since work hardening is not introduced in the process; however, to help compensate for the strength disparity, cast alloys are often subjected to heat-treatment or grain refinement to increase their strength [7].Like wrought alloys, cast alloys in North America are most commonly identified by a four-digit nomenclature adopted by the Aluminum Association. The first digit (***X***xx.x) denotes the primary alloying element; the second and third digits (x***XX***.x) are the alloy's specific identifier; and the fourth digit (xxx.***X***) shows the form (casting {0}, standard ingot {1}, or ingot of high compositional tolerance {2}) [7], [8], [15], [16]. Also, a casting or ingot with only a small compositional difference to the original alloy is identified by a preceding serial letter (ex. 356.0, A356.0, B356.0, etc.) [7], [8], [15], [16]. Table 2.1 below lists the Aluminum Associations nomenclature for cast aluminum alloys.

Table 2.1: Aluminum cast alloy nomenclature, the Aluminum Association [7], [8], [15]

Alloy series	Principal alloying element	Common applications
1*xx.x*	None (pure aluminum)	Large electric rotors (100.0)
2*xx.x*	Copper	Aerospace housings (201.0)
3*xx.x*	Silicon, copper	Engine components (319.0)
4*xx.x*	Silicon	Street lamp housings (A413.0)
5*xx.x*	Magnesium	Chemical fittings (514)
7*xx.x*	Zinc	Pumps, large mining equipment (713.0)
8*xx.x*	Tin	Railroad journal bearings (850.0)
9*xx.x*	Other	-
6*xx.x*	Unused series	-

2.2 ALUMINUM ALLOY B319

The B319 alloy is a variation of the silicon-copper cast aluminum alloy 319; Table 2.2 below shows the composition of the 319 and B319 alloys according to the American Society for Testing and Materials (ASTM) standards [17]. The following sections will discuss the applications and properties of the B319 alloy and the 319 alloy family, as well as the effects of each of the alloying elements.

Table 2.2: Chemical compositions of the aluminum alloys 319.1 and B319.1 [17]

Elements	Si	Cu	Zn	Fe	Mn	Ni	Ti	Mg	Other	Al
319.1 wt%	5.5-6.5	3.0-4.0	1.0	0.8	0.5	0.35	0.25	0.1	0.5	Balance
B319.1 wt%	5.5-6.5	3.0-4.0	1.0	0.9	0.8	0.5	0.25	0.15-0.5	0.5	Balance

2.2.1 PROPERTIES

The 319 alloy family of aluminum have various desirable properties frequently sought for many high strength-to-weight ratio components and general cast components in the automotive industry. These properties include: (i) adequate strength at ambient and elevated temperatures, (ii) excellent castability, (iii) heat treatability, (iv) pressure tightness, and (v) good corrosion resistance [7], [8], [18]. Therefore, the 319 alloy family of aluminum alloys is commonly used for complex casting applications such as engine blocks, cylinder heads, and other automotive drive train parts. For strength comparison, the aluminum alloy 319.0T6 has a tensile yield strength of 185 MPa, which is more then twice the yield strength of 44W mild steel when compared on an equivalent weight basis [8]. Table 2.3 below shows the mechanical properties for the 319 alloy.

Table 2.3: Mechanical properties of aluminum 319.0 [8]

	Tension						
Temper	Ultimate strength (MPa)	Yield strength (MPa)	Elongation (%)	Hardness (HB)	Shear ultimate strength (MPa)	Fatigue endurance limit ($5x10^8$ cylces) (MPa)	Modulus of elasticity (GPa)
Sand casting							
F	185	125	2	70	150	70	74
T5	205	180	2	80	165	75	74
T6	250	165	2	80	200	75	74
Permanent mold casting							
F	235	130	3	85	165	…	74
T6	275	185	3	95	…	…	74

The physical properties and mechanical behavior of the B319 alloy depends heavily on the system's alloying elements and microstructure. Each element, whether purposefully added or found as an impurity, contributes to the final alloy's microstructure, which will affect the alloy's mechanical properties.

2.2.2 ALLOYING ELEMENTS AND MICROSTRUCTURE

The B319 alloy contains eight different alloying elements (Table 2.2) as well as several trace impurities. The B319 alloy microstructure usually consists of three main microconstituents: a primary α-Al matrix, an Al-Si eutectic phase, and an Al-Cu second-phase intermetallic. Additionally, most 319 alloys contain notable iron impurities that also form second-phase Al-Fe intermetallics. The following text summarizes each of the alloying elements in the B319 alloy.

2.2.2.1 SILICON

The B319 alloy contains 5.5-6.5wt% silicon and therefore the alloy is considered a hypoeutectic Al-Si system, as shown in Figure 2.1 (<12.6wt% Si) [8], [19].

Silicon is added primarily to improve the molten metal fluidity and castability of the B319 alloy by lowering the liquidous temperature of aluminum (as seen in Figure 2.1) [7], [8], [20]–[22]. This works to improve feeding characteristics and minimize casting voids or incomplete mold filling.

However, in addition to fluidity improvement, Silicon addition in the B319 alloy helps to decrease casting shrinkage, reduce hot-tearing, and improve casting soundness; due to the fact that Si expands up to 2.9% during solidification [6], [8]. Silicon addition has also been found to increase the tensile strength and hardness of aluminum alloys through precipitation strengthening and two-phase solidification. These effects increase alloy strength up to the eutectic composition (11-13wt% Si), beyond this point the primary phase changes to Si and decreases the alloy strength and hardness [6], [20], [23]. Alloy ductility is observed to show a nearly linear negative correlation to strength and hardness for this range below the eutectic composition [23].

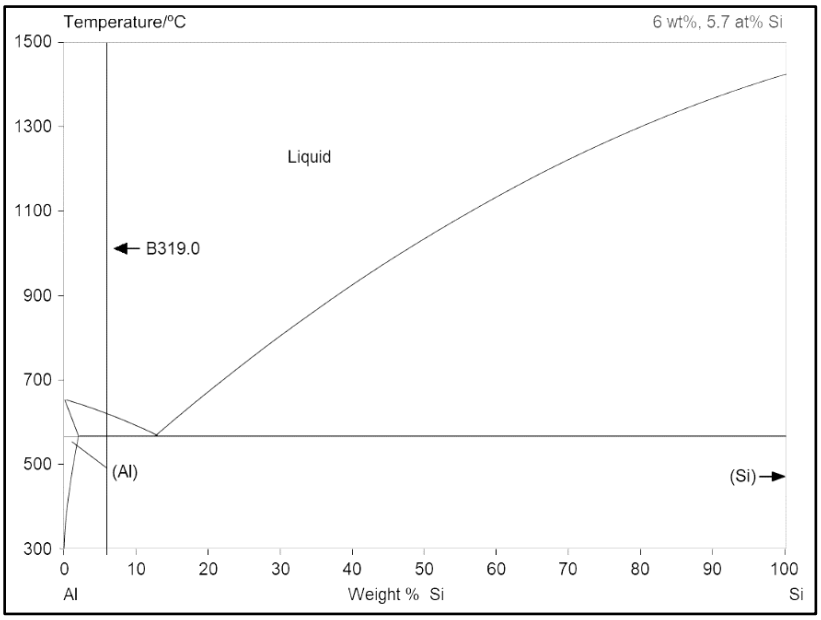

Figure 2.1: Al-Si phase diagram [24]

Silicon has a relatively low solid solubility in aluminum (1.65wt% at the eutectic temperature (577°C) and 0.01wt% at room temperature) [20]. Therefore, silicon is mostly found in a nearly pure phase, taking a eutectic form of coarse acicular particles alongside eutectic aluminum. During solidification, the primary α-Al forms first as dendrites, followed by the solidification of the

Al-Si eutectic in the interdendritic regions. Figure 2.2 shows the microstructure of a 319 alloy, where the silicon eutectic phase is the dark grey script phase denoted in boxes.

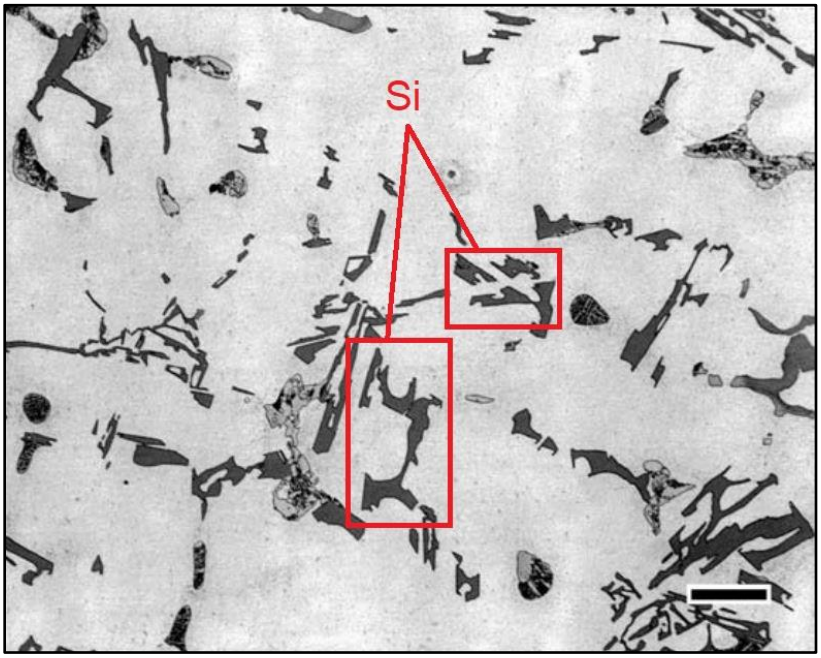

Figure 2.2: As-cast AA319 (micro bar length is 50µm) [25]

Studies have shown that the morphology of the silicon eutectic can be effectively modified by heat treatment or the addition of strontium or sodium. This has a significant impact on increasing the mechanical properties of Al-Si alloys [26]–[28]. This modification is referred to as spheroidization and changes the acicular silicon to a more fibrous form, the mechanisms of which are still largely debated [27].

2.2.2.2 COPPER

Copper is the second dominant alloying element in the 319 aluminum alloy. Copper serves to increase the as-cast and high temperature mechanical properties through precipitation hardening, which is most effectively done through aging heat treatments. In general, copper addition to Al-Si alloy systems has been found to increase the strength and hardness, but also decrease ductility and corrosion resistance [29]–[31]. Figure 2.3 below shows a ternary phase diagram of the Al-Cu-Si system, which shows that the addition of copper to Al-Si also functions to slightly lower the alloy's liquidus point.

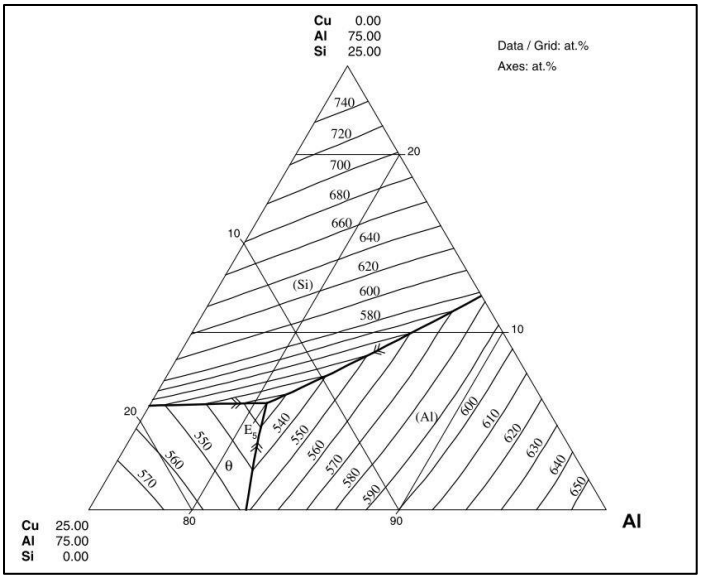

Figure 2.3: Al-Cu-Si Ternary phase diagram, liquidus projection of the Al-rich corner

The B319 alloy contains 3.0-4.0wt% Cu, which is known to be an effective range to achieve precipitation hardening, since copper has a maximum solubility of 5.65wt% in Al at the eutectic temperature (548°C) (Figure 2.4) [6], [8], [21].

Copper in 319 alloys is typically found in the body-centered tetragonal (BCT) $CuAl_2$ phase, which forms either a blocky $CuAl_2$ morphology or an Al-$CuAl_2$ eutectic lamellar morphology [6], [25], [32]. Figure 2.4 and Figure 2.5 show the B319 alloy on the binary Al-Cu phase diagram and SEM images of common Al-Cu eutectic phase morphologies found in Al-Si alloys.

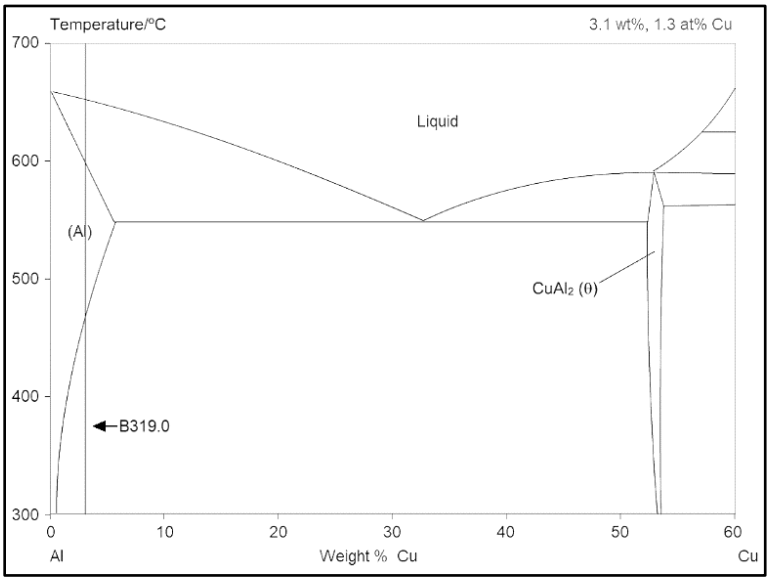

Figure 2.4: Al-Cu phase diagram [24]

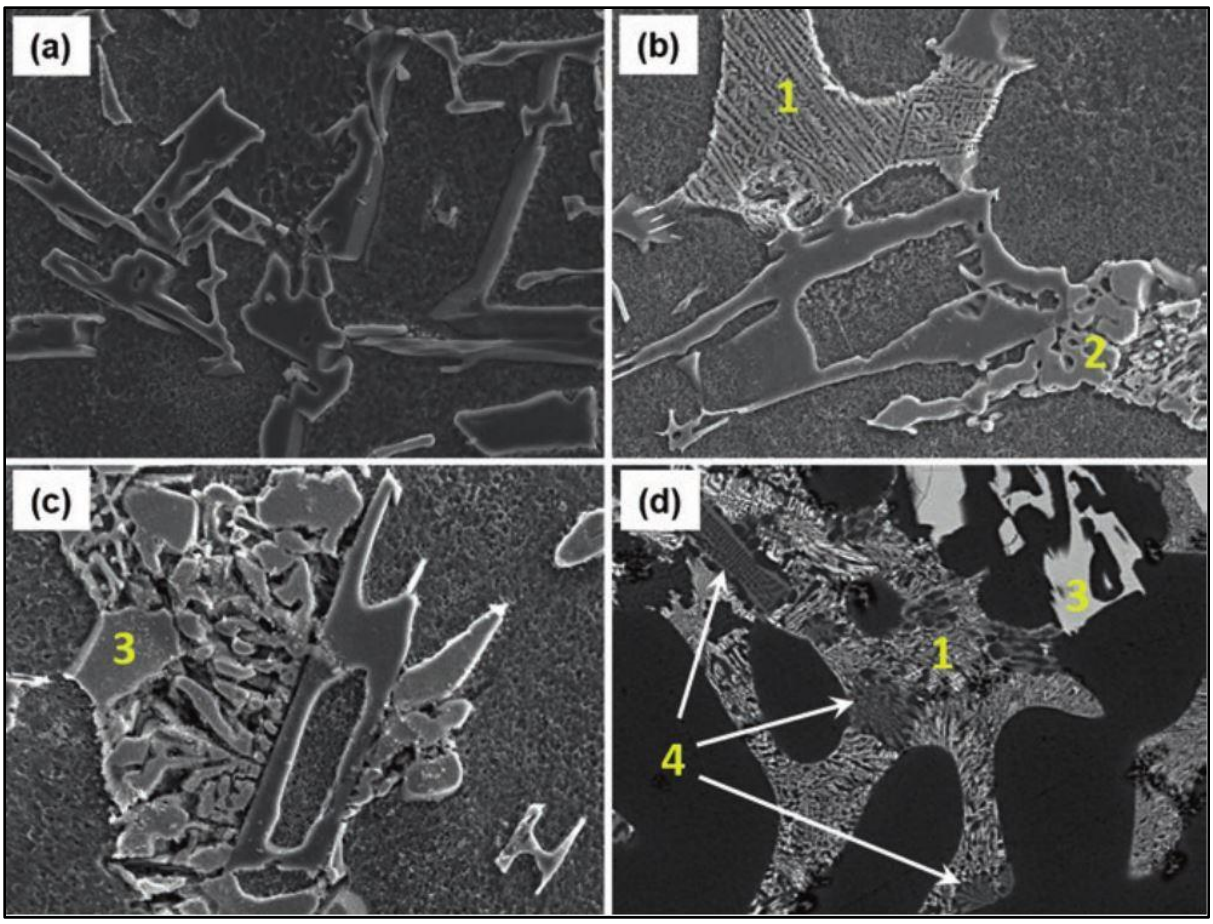

Figure 2.5: SEM images of Al-Si alloys showing various eutectic phases; (a) Al-Si, (b) Al-Cu, (c) Al-Cu-Ni, (d) mix; (1) fine eutectic Al-Cu, (2) blocky Al-Cu, (3) Al_3CuNi, (4) Mg_2Si [6]

For the 319 alloys, the Al-Cu phases form in a multicomponent eutectic phase after the Al-Si eutectic reaction [32], [33]. In this case, the iron intermetallic β-Al_5FeSi first precipitates and then acts as a nucleant for the $CuAl_2$ precipitate [32].

Wu *et al* [30] found that in high-Cu Al-Si alloys (4.65wt% Cu), excess copper attracts magnesium to form the fine multi-phase $Al_5Cu_2Mg_8Si_6$ intermetallic. While the $Al_5Cu_2Mg_8Si_6$ phase does provide limited strengthening (compared to $CuAl_2$), a lack of available Mg atoms then causes Fe atoms to precipitate out in the acicular β-Al_5FeSi phase rather then the less deleterious π-$Al_8Mg_3FeSi_6$ intermetallic. The presence of acicular β-Al_5FeSi was found to cause tensile strength loss, but can be reduced by heat treatment and the spheriodization of the surrounding $CuAl_2$ [32].

2.2.2.3 IRON

Iron is a common impurity in aluminum alloys. It is typically introduced during the refinement and smelting of bauxite in the Bayer and Hall-Héroult processes [7]. In Al-Si alloys, iron is often present in higher percentages due to additional contamination during recycling (i.e. when engine blocks are recycled without removal of the iron bore liner) [6]. Iron has been found to improve hot-tear resistance and elevated temperature strength of aluminum, but these improvements come at the cost of lower ductility and castability [8], [34]. Research by Hetke found that doubling Fe levels from 0.15wt% to 0.30wt% decreased the ductility of aluminum 356 by a factor of two [35]. Therefore, iron is considered a deleterious element in the 3*xx* aluminum alloy series.

There is up to 0.9wt% Fe in the B319 alloy [6]. Iron has a maximum solid solubility of 0.05wt% in aluminum, but can reach levels as high as 5.0wt% Fe at 800°C [7], [36], [37]. Consequently, in solid state, aluminum iron is precipitated out in Fe intermetallic phases. In alloys with low silicon content, iron is almost entirely present in the monoclinic phase Al_3Fe [38]. At higher silicon contents, such as in the case of the B319 alloy, iron forms two main intermetallic phases: α-Al_8Fe_2Si (α-Fe) and β-Al_5FeSi (β-Fe) [7], [34], [36], [37], [39].

The α-Fe phase has a cubic script morphology, while the β-Fe phase has a orthorhombic needle-like platelet morphology [40]. Figure 2.6 shows micrographs of the various phases of Al-Si-Fe systems.

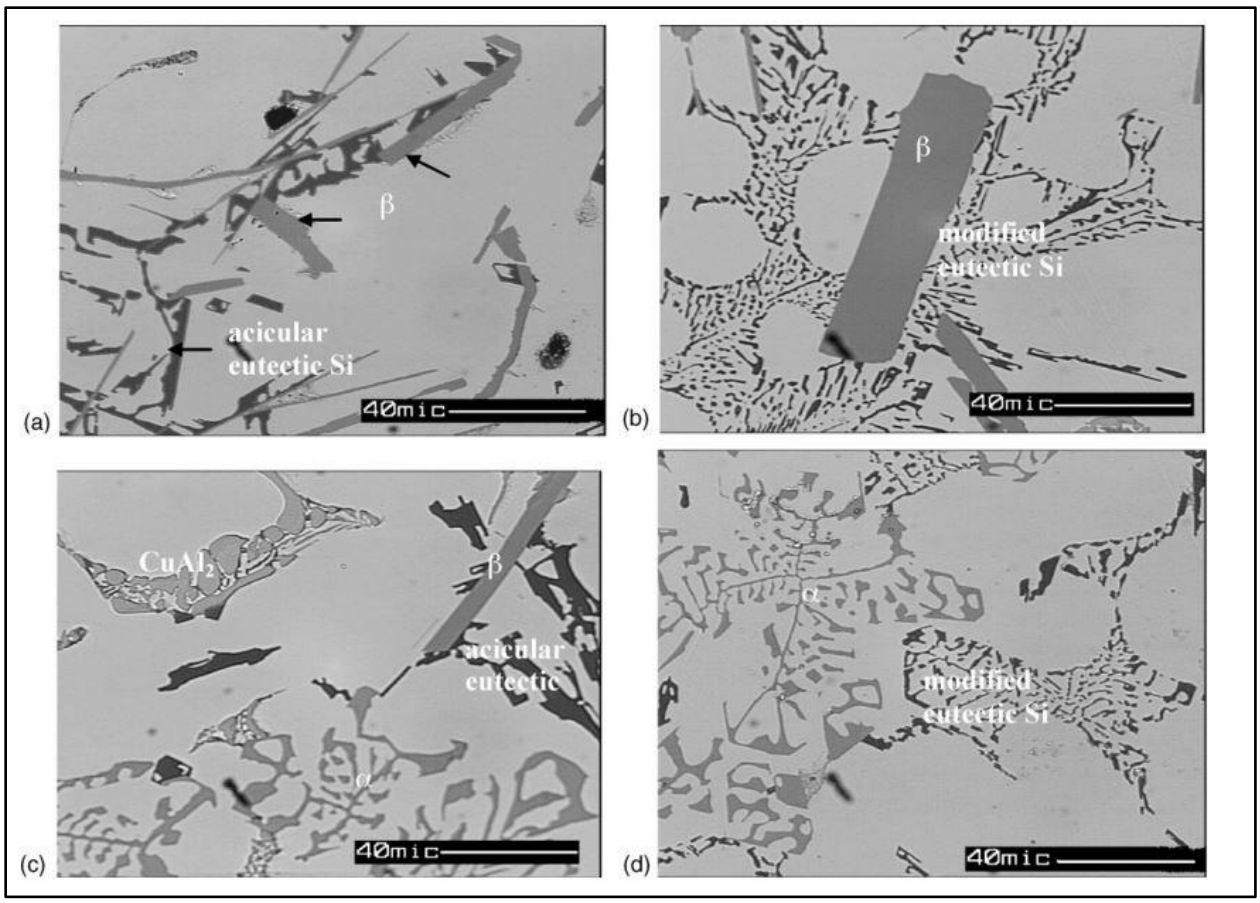

Figure 2.6: Optical micrographs from as-cast aluminum 319; (a) eutectic Si and β-Fe, (b) modified eutectic Si and β-Fe, (c) $CuAl_2$ and β-Fe, (d) modified eutectic Si and α-Fe [41]

The β-Fe phase is more deleterious to mechanical and casting properties and thus the formations of the α-Fe phase is desirable. There are three industrial methods to convert harmful β-Fe acicular phases to less harmful α-Fe script phases: (1) rapid solidification, (2) melt superheating, and (3) addition of elements.

1. Rapid solidification interrupts the formation of large β-Fe platelets and instead creates smaller and more dispersed platelets [35], [36].
2. Melt superheating (≥850°C) transitions γ-alumina(γ-Al_2O_3) to α-alumina(α-Al_2O_3), which is a poor nucleant for the β-Fe phase and indirectly causes the formation of the α-Fe phase instead [34].
3. Addition of elemental Mn or Mg has been found to help control unfavourable Fe intermetallics by “conversion” from β-Fe to α-Fe type phases. If Mg is present in Al-Si-Fe systems, an alternate script-like phase π-$Al_8FeMg_3Si_6$ will precipitate. If Mn is also added, then the α-FeMn script phase α-$Al_{15}(Fe,Mn)_3Si_2$ will precipitate. The α-FeMn

phase is distinguishable from the standard α-Fe due to its more compact and "blocky" formation [36], [37], [41].

2.2.2.4 MANGANESE

Manganese is often considered an impurity in aluminum castings; however, as discussed in the previous section, for Al-Si casting alloys with high iron concentrations, manganese is added to control the Fe intermetallics [8]. Manganese controls Fe intermetallic formation by precipitating α-Fe type phases rather than the β-Fe type phases (seen in Figure 2.6), and hence significantly increases the alloy's tensile strength and ductility [42].

The B319 alloy contains 0.8wt% Mn, which has a very low solubility in aluminum. It typically forms as a cubic α-$Al_{15}(Fe,Mn)_3Si_2$ script phase [36], [41], [42]. Research by Hwang *et al* [42], Taylor [36], and Narayanan *et al.* [34] found that Mn should be added to Al-Si alloys at a Fe/Mn ratio of ~1.2. Excess amounts of Mn were found to deteriorate mechanical properties by the formation of a coarse polyhedral α-$Al_{15}(Fe,Mn,Cr)_3Si_2$ "sludge" in the liquid stage, which caused fluidity problems and later solid state weakness or embrittlement.

2.2.2.5 MAGNESIUM

Magnesium is often added to Al-Si alloys to reduce the solidification range, improve heat treatability, and provide strengthening through precipitate hardening [6], [8]; yet, ductility is reduced with increased magnesium content [43]. The precipitate hardening effects of Mg has been attributed to the formation of complex intermetallics involving Si, Cu, and Fe.

There is between 0.15-0.5wt% Mg present in the B319 alloy. Typically, three Mg-rich intermetallic phases form: (i) Mg_2Si, (ii) $Al_5Cu_2Mg_8Si_6$, or (iii) π-$Al_8FeMg_3Si_6$.

The Mg_2Si phase is seen to crystalize primarily in a spheroidal and elongated spheroidal morphology in regions adjacent to the Si eutectic [44]. Work by Ouelett and Samuel [45] revealed that the hardening of 319 alloys develops by the cooperative precipitation of the $CuAl_2$ and Mg_2Si phases during solution heat treatment.

The $Al_5Cu_2Mg_8Si_6$ phase is often seen to solidify in branched crystals or fine irregular eutectic growing from excess copper around $CuAl_2$ particles [30], [46], [47]; however, Samuel *et al* discovered that Mg content in excess of 0.4wt% caused solidification of a separate script morphology before $CuAl_2$ precipitation [48].

The π-$Al_8FeMg_3Si_6$ phase takes the form of script and was seen to strengthen Al-Si-Fe systems by forming the π-Fe phase in favour of the unfavourable β-Fe phase [36], [41].

In addition to the strengthening provided by the above three phase, Samuel *et al.* [48] observed that the general addition of Mg to 319 alloys resulted in the modification of the Al-Si eutectic. It has been reported that Mg addition decreased the surface tension and solid-liquid interfacial energy of molten Al-Si alloy [44], [49]. A reduction of the interfacial energy improves the wetting angles between substrates and liquid Al, therefore promoting refinement of α-Al dendrites and Al-Si eutectic. Research by Li *et al.* [50] and Abedi *et al.* [49] verified that additions of Mg from 0.5-2.0wt% for a Al-7Si alloy caused refinement of both the α-Al and the Al-Si eutectic.

2.2.2.6 TITANIUM

Titanium is added to Al-Si-Cu alloys as both an alloying element and as a grain refiner – the grain refining purposes of titanium in the B319 alloy will be discussed in section 2.4.2. Titanium is used as an alloying element to increase both the ductility and strength of castings, as well as to reduce cracking [8], [51]. There is 0.25wt% Ti present in the B319 alloy, which typically partitions to the α-Al solid solution or $TiAl_3$ phase [8]. Ji *et al.* [51] studied the effect of Ti addition on an Al-Mg-Si-Mn alloy and found that an addition of 0.2wt% Ti was able to increase the yield strength by 15% and the percentage elongation from 11% to 18%.

2.2.2.7 NICKEL

Nickel is commonly added to Al-Si-Cu alloys to increase tensile and yield strength at elevated temperatures (250-375°C operating range), while also lowering the coefficient of thermal expansion [6], [8]. The B319 alloy contains 0.5wt% Ni, which results in increased yield strengths of up to 50 MPa after heat treatment [52]. The phase responsible for this strengthening is the Al_3Ni intermetallic, which is complementary to the Al-Cu intermetallics. Figure 2.5*c* shows the morphology of the Al-Cu-Ni intermetallics.

Addition of more than 4.0wt% Ni is not common due to the number of brittle precipitates that form, which affect the casting soundness and increase the cracking susceptibility [6].

2.2.2.8 ZINC

Zinc is often present as an impurity due to the recycling of scrap 7*xxx* and 7*xx.x* alloys. For application in Al-Si-Cu alloys, research by Morinaga *et al.* [53] found that for Zn additions of up to 1.48wt% increased the tensile strength, but decreased to corrosion resistance. In the B319 alloy 1.0wt% Zn is added to improve the alloy's strength after T5 or T6 heat treatments [6].

The Al-Zn system within 319 alloys typically forms either the hexagonal $MgZn_2$ or body-centred cubic (BCC) $Al_2Mg_3Zn_3$ phases [7].

2.2.2.9 SOLIDIFICATION REACTIONS

The B319 alloy is a hypoeutectic Al-Si system, as well as a hypoeutectic Al-Cu system, and therefore exhibits three primary solidification reactions; the primary evolution of FCC α-Al dendrites (~608°C), and two eutectic reactions with Si (~561°C) and Cu (~507°C) [6], [52], [54]. In addition to the three primary reactions, there are several other secondary stages of solidification involving Fe, Mn, Mg, Cu, Ni, and Zn intermetallics. In general, the solidification reactions of the B319 alloy are exothermic and can be identified by differential scanning calorimetry (DSC) and thermal analysis (TA) as the points of increased system enthalpy. Depending on parameters such as the sample cooling rate, elemental composition, and equipment sensitivity; the various secondary phases of solidification may or may not be identifiable. Table 2.4 below lists possible solidification reactions occurring for 319 alloys according to Samuel *et al.* [55].

Table 2.4: Possible solidification reactions occurring for 319 alloys according to Samuel et al. [55]

Stage	Description	Reaction	Temp. (°C)
1	Solidification of course polyhedral Al-Fe-Mn-Cr-Si "sludge"	$L \rightarrow \alpha\text{-}Al_{15}(Fe,Mn,Cr)_3Si_2$	-
2	Formation of the α-Al dendritic network (liquidus point)	$L \rightarrow \alpha\text{-}Al$	608
3	Precipitation of pre-eutectic script α-Fe*	$L \rightarrow Al + \alpha\text{-}Al_{15}(Fe,Mn)_3Si_2$	591
4	Precipitation of pre-eutectic needle β-Fe with α-Fe*	$L \rightarrow Al + \alpha\text{-}Al_{15}(Fe,Mn)_3Si_2 + \beta\text{-}Al_5FeSi$	577
5	Eutectic Al-Si reaction	$L \rightarrow Al + Si$	556
6	Precipitation of post-eutectic β-Fe	$L \rightarrow Al + Si + \beta\text{-}Al_5FeSi$	548
7	Transformation of β-Fe to script π-Fe	$L \rightarrow Al + Si + \beta\text{-}Al_5FeSi + \pi\text{-}Al_8(Fe,Mg)_3Si_6$	530
8	Precipitation of Mg-Si intermetallic particles	$L \rightarrow Al + Si + \beta\text{-}Al_5FeSi + Mg_2Si$	527
9	Al-Cu eutectic reaction and precipitation of Al-Cu particles	$L \rightarrow Al + Si + \beta\text{-}Al_5FeSi + Mg_2Si + CuAl_2$	503
10	Precipitation of Al-Cu-Mg-Si** particles and final solidification (solidus point)	$L \rightarrow Al + Si + Mg_2Si + CuAl_2 + Al_5Cu_2Mg_8Si_6$	497

** The α-Fe phase can precipitate in the absence of Mn as script $\alpha\text{-}Al_8Fe_2Si$ and has been associated with melt superheating (≥850°C)* [34].

*** Precipitation of $Al_5Cu_2Mg_8Si_6$ particles has also been observed prior to the Al-$CuAl_2$ eutectic reaction* [48].

Reaction temperatures for the three central phase evolutions of the 319 alloy are well documented and average 608°C for α-Al dendritic growth, 561°C for Al-Si eutectic development, and 507°C for Al-Cu eutectic development [48], [52], [55]–[61]. However, as seen in Table 2.5 below, reaction temperatures and reaction order for the secondary solidification stages show variability. Table 2.6 shows the respective alloy compositions corresponding to the literature from Table 2.5. The compositional differences seen were thought to have been a driving factor behind the secondary intermetallic reaction ranges, as seen by Bäckerud *et al.* [52] where comparatively low levels of Si and Mg may have contributed to a high liquidus temperature.

Table 2.5: Solidification reaction temperatures of 319 alloys across literature [48], [52], [55]–[61]

Stage	Reaction temperatures (°C)							
	*Average or range**	Samuel *et al.* [48]	Samuel *et al.* [55]	Bäckerud *et al.* [52]	Samuel *et al*. [56]	Vandersluis [57]	Shabestari and Ghodrat [58]	Farian *et al.* [59]
1	-	-	-	-	-	-	-	-
2	608	601	608	609	610	608	611	607
3	610-562	-	591	590	-	-	610	-
4	610-562	-	577	575	562	-	610	-
5	561	562	556	575	562	560	553	557
6	560-510	-	548	525	510	-	-	-
7	554-530	-	530	-	554	-	552	-
8	554-527	-	527	-	554	-	-	-
9	548-503	504	503	525	510	-	503	494
10	507-484	494	497	507	490	485	490	484

Table 2.6: Alloy compositions corresponding to Table 2.5 [48], [52], [55]–[59]

	Element	Si	Cu	Fe	Mn	Mg
Composition (wt%)	Samuel *et al.* [48]	6.86	3.35	0.2	0.08	0.38
	Samuel *et al.* [55]	6.04	3.5	0.61	0.23	0.32
	Bäckerud *et al.* [52]	5.70	3.4	0.62	0.36	0.1
	Samuel *et al*. [56]	6.23	3.8	0.46	0.14	0.06
	Vandersluis [57]	6.37	3.35	0.66	0.34	0.4
	Shabestari and Ghodrat [58]	5.5	3.4	0.12	0.23	0.42
	Farian *et al*. [59]	5.54	3.06	1.0	0.5	0.2

2.3 ALUMINUM CASTING

Due to its relatively low melting point (e.g. compared to bronze or steel), desirable material properties, and broad application range; aluminum and its alloys have become one of the most popular casting metals in modern manufacturing [7]. The B319 alloy has several alloying

elements that improve the alloy's castability and heat treatability, therefore making it a popular alloy for automotive power train casting applications. Automotive parts casting involves one of two general processes: expendable mold casting and non-expendable casting processes. Each of these casting variations, as well as the process parameters are summarized below.

2.3.1 EXPENDABLE MOLD CASTING

The expendable mold casting processes involve the use of a mold that is destroyed after casting or during part removal. Some examples include plaster casting, shell mold casting, investment casting, sand casting, lost foam casting, vacuum mold casting, and high precision sand casting (HPSC). The most common process used for automotive applications is the HPSC process, in which the molds and internal cores are formed from a compacted or chemically bonded base sand, such as silica (SiO_2) or zircon (Zr_2O+SiO_2) [62]. HPSC is often used for automotive applications due to its low tooling costs and pattern flexibility. Additionally, HPSC can accommodate high complexity parts, such as engine blocks, with the use of internal mold cores. Some of the HPSC's disadvantages, however, are poor surface finish and a low mold thermal conductivity, which can lead to undesirable material properties or variable heat gradients at thick part sections [6], [8]. For some applications, a nonexpendable mold casting process may be more appropriate.

2.3.2 NONEXPENDABLE MOLD CASTING

Nonexpendable mold casting, also called permanent mold casting, is a casting process featuring a reusable mold, often machined from steel or copper [7]. Examples of permanent mold casting processes include low/high pressure die casting, vacuum casting, centrifugal casting, and squeeze casting. Permanent mold casting offers many advantages over expendable mold castings processes, namely the higher part production volume, high dimensional accuracy, better surface finish, and higher cooling rates. Disadvantages of permanent mold castings are high tooling costs, alloy interaction tolerance, and restrictions on part geometries. Although true permanent molds are unable to produce complex part geometries, internal sand cores can be used in conjunction with permanent molds (this is called a semi-permanent mold casting) [6], [8], [62].

2.3.3 PROCESS PARAMETERS OF CASTING

Common to either the expendable or permanent mold processes, the three primary casting process parameters are: melt treatment and composition, pouring temperature, and mold temperature.

Melt treatment is a processing parameter used to “clean” the material before or during pouring, by removing deleterious oxides, impurities, or gases. If the melt is not properly treated prior to pouring, then there is an increased chance that the final casting will suffer in soundness or strength due to gas entrapment or contaminant inclusion [8]. Oxides and impurities can usually be filtered mechanically or precipitated out of the molten metal by fluxing. Gases must be removed through degassing procedures, such as sparging or proper mold gating and runner design [8]. A major source of porosity in aluminum castings is caused by dissolved hydrogen (H_2). Molten aluminum has a high solubility for H_2, which increases with temperature and time at temperature. As solidification begins, H_2 solubility in aluminum rapidly decreases and gas pores are formed at dendritic boundaries (generally these pores are spherical and less than 0.5mm in diameter) [63]. The presence of high dissolved H_2 content will therefore lead to the dispersed formation of mircoporosity throughout the casting, which can be detrimental to casting soundness and material strength.

The casting’s pouring temperature and mold temperature are both parameters that directly affect a casting’s solidification rate. The solidification rate has a direct impact on other casting characteristics, such as fluidity and grain structure. For instance, a slower solidification rate may result in better fluidity, but will lead to larger grain structure (more on this in Section 2.4). Hetke [35] found that increasing the rate of solidification greatly reduced the alloy segregation and partitioning between dendrites, which in turn decreased the size and agglomeration of intermetallic phases. This was confirmed by Farina *et al.* [59] who found that increased solidification rates better dispersed Fe intermetallics, as well as increased the conversion of β-Fe phases to α-Fe phases. It has also been well documented in literature that increasing the rate of solidification reduces the final alloy grain size and improves microstructure homogeneity, thereby increasing mechanical properties [64]–[68].

In some instances of castings however, either the mold design, mold material, or other process constraints will impede a designer’s ability to change pouring temperatures or mold temperatures. Also, these parameters may already be tightly controlled, and additional grain size reduction or microstructure homogenization may still be required. For this, further grain size reduction or microstructure homogenization can be achieved with a method of chemical grain refinement.

2.4 GRAIN REFINEMENT AND SOLIDIFICATION

Grain refinement is a process by which a cast alloy's grain structure can be reduced into fine equiaxed grains. Grain size reduction has been found to improve feeding, reduce hot tearing, reduce porosity, and improve general mechanical properties of an as-cast alloy. Grain refinement can be done either thermally, by increasing the solidification rate; mechanically, by semi-solid vibration and stirring; or chemically, by the addition of grain refining elements [6]. This work studied, in part, the grain refinement of the B319 alloy via chemical treatment. Therefore, the following section focuses on the process of chemical grain refinement and how it affects the solidification of aluminum alloys. The mechanisms of grain refinement in relation to grain nucleation theory are presented first for background.

2.4.1 NUCLEATION

In general, solidification can be divided into two main stages: nucleation and growth. Nucleation is the first stage and signifies the initial self-arrangement of atoms into a new phase or structure. To begin nucleation in a metal, the material's solid state free energy (known as the Gibbs free energy, *G*) must be less than the liquid state free energy. At this threshold, liquid atoms will begin agglomerating together to form solid nuclei, of some critical size of stability, from which further development will drive solidification (growth) [69], [70].

The nucleation and growth process of metals can be generally described by a theoretical nonequilibrium cooling curve, seen in Figure 2.7. Cooling curves are produced with the placement of a thermocouple in molten metal as it solidifies. The thermocouple captures a temperature profile over time and can provide useful information on solidification behavior and phase evolution of an alloy.

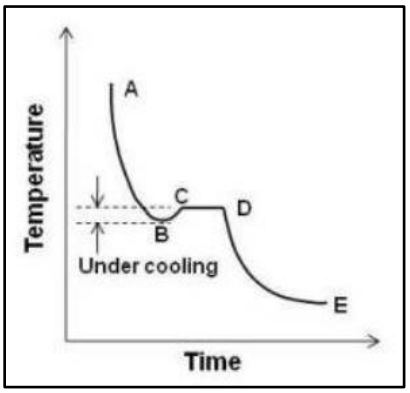

Figure 2.7: Illustration of a pure metal's cooling curve [71]

Points *A*-*E* of the cooling curve above represent temperatures and times of significance over the metal's solidification profile. Point *A* denotes pouring (or initiation of cooling), point *B* is the nucleation point, point *C* represents growth stabilization, point *D* denotes the end of phase transformation, and point *E* is the final resting temperature. Between points *B* and *C,* a sharp temperature increase can be seen, which represents the release of latent heat (called recalescence) from the initial nucleation. Between points *C* and *D,* latent heat is continually released, but the temperature levels off due to growth stabilization. The temperature difference between points *B* and *C* is known as undercooling, which is necessary to begin stable nucleation [70]. The magnitude of undercooling, however, is determined largely by whether nucleation is homogeneous or heterogeneous.

2.4.1.1 HOMOGENEOUS NUCLEATION

Homogeneous nucleation takes place when a solid spontaneously develops within cooling liquid metal. It is assumed that the precipitating solid takes the shape of a sphere, as seen in Figure 2.8(left), and therefore the Gibbs free energy for the particle can be expressed by Equation 2.1 [69], [70] below.

$$\Delta G = \frac{4}{3}\pi r^3 G_v + 4\pi r^2 \gamma \qquad \textbf{2.1}$$

where ΔG = change in free energy

r = radius of spherical nucleus

G_v = Gibbs free energy per unit volume; a $f(_{latent\ heat})$ and $f(_{undercooling})$

γ = Gibbs free energy per unit area

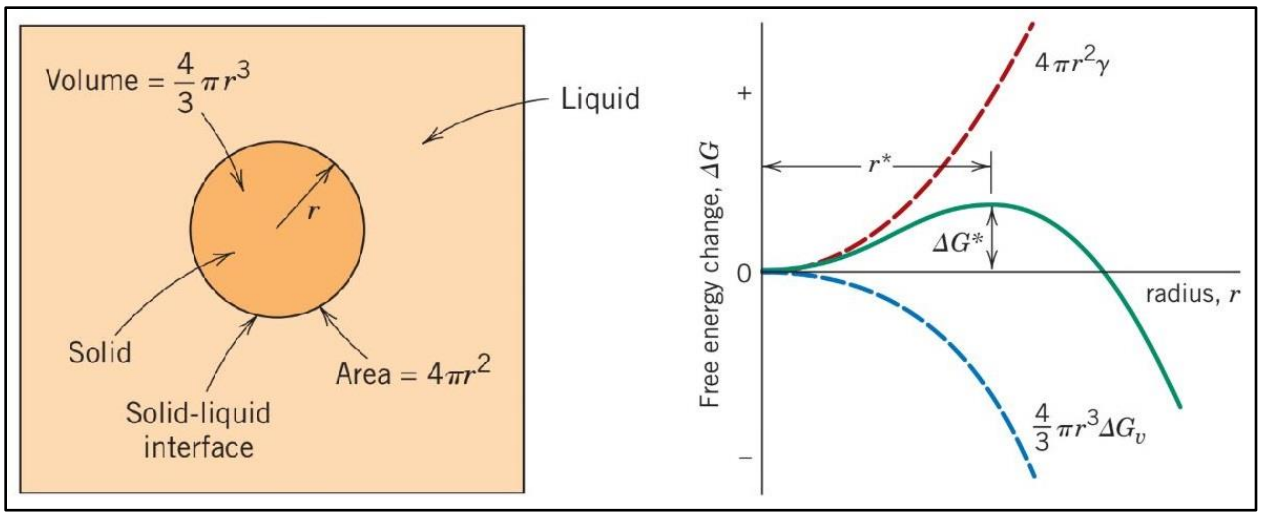

Figure 2.8: Homogeneous nucleation; (left) homogeneous sphere precipitate, (right) Gibbs free energy of homogeneous nucleation [69]

Equation 2.1 can be seen graphically in Figure 2.1(right); which shows that for nuclei to form and grow, a critical radius (r^*) must be formed so that additional growth (increased r) results in a reduction of free energy. The critical radius of nucleation can be found by solving for the point of zero slope taken from the derivative of Equation 2.1) (where $d\Delta G/dr = 0$). Therefore, the critical Gibbs free energy of nucleation (ΔG using r^*) can be represented by Equation 2.2 [69], [70] below.

$$\Delta G^* = \frac{16\pi\gamma^3}{3(\Delta G_v)^2} \qquad \textbf{2.2}$$

ΔG_v, the volume free energy change, is a function of temperature (T) and becomes increasingly negative after the temperature has fallen below the melting temperature (T_m). Therefore, as the magnitude of undercooling (T_m-T) increases, the minimum nuclei radius and the overall energy for nucleation decreases. Consequently, for complete homogenous nucleation the undercooling magnitude must reach tens to hundreds of degrees Celsius. In practice however, most material exhibits undercoolings of only a few degrees, which is attributed to heterogeneous nucleation [70].

2.4.1.2 HETEROGENEOUS NUCLEATION

Heterogeneous nucleation takes place when a solid develops from foreign particles or surfaces present in cooling liquid metal. These foreign particles can be impurities, oxides, mold walls, or other elements; all of which provide preferential sites for nucleation. The presence of foreign

particles heavily decreases the required surface free energy of nucleation, since forming atoms can bond onto existing surfaces rather than creating new ones. Figure 2.9(left) shows the surface interface between some forming nuclei solid and a heterogenous particle. The forming nuclei has three interfacial energies γ_{SI}, γ_{SL}, and γ_{IL}; which determine a resultant wetting angle, θ. As θ decreases, the effective radius of the forming solid increases, therefore decreasing the required Gibbs free energy for nucleation. If $\theta \approx 0$, then complete wetting occurs, which is the ideal case for heterogeneous nucleation [69], [70].

Figure 2.9(right) shows that heterogeneous nucleation requires much less energy to reach an equivalent effective critical radius when compared to homogeneous nucleation. For this reason, heterogenous nucleation has far lower magnitudes of undercooling than homogeneous nucleation [69].

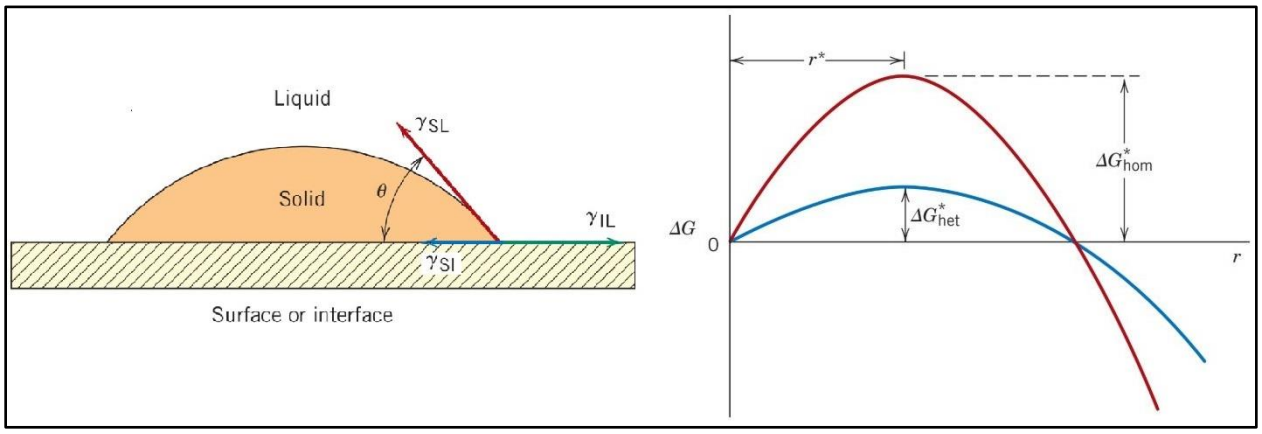

Figure 2.9: Heterogeneous nucleation; (left) nucleation surface interface, (right) Gibbs free energy of heterogeneous nucleation versus homogeneous nucleation [69]

Heterogeneous nucleation is the operating mechanism of chemical grain refinement, which works by physically introducing foreign particles into liquid metal as nucleation sites. However, material characteristics and the interaction of the matrix metal and inoculating particles play an important role in grain refinement effectiveness.

2.4.2 GRAIN REFINERS FOR ALUMINUM ALLOYS

Research has been done into understanding the fundamentals and design of grain refiners for aluminum alloys. The results suggest that the ideal inoculating particles should:

1. Have a similar crystal structure or good lattice matching to the primary alloy phase, allowing for better wetting and heterogeneous nucleation [9], [70].

2. Have a good stability in the melt (a higher melting temperature than the primary alloy) [9], [70]
3. Be effective in small amounts so as not to disrupt the overall composition [70]
4. Have no deleterious effects on material properties [70]
5. Initiate freezing at low undercoolings [9]
6. Have a larger particle size than the critical size, which is dependant on the melt undercooling [9]
7. Have a fast optimum contact time and a slow fade time [9]
8. Be resistant to nucleation interference from other alloy constituents, referred to as poisoning [9]
9. Have a large grow restricting factor (GRF) and promote constitutional undercooling [72]–[74]

A major challenge for chemical grain refinement, however, is the equal distribution of refining material throughout the liquid metal before or during casting. Due to density differences and wetting properties, the inoculant material often agglomerates together and typically sinks in the aluminum melt – this sedimentation can be rapid and is known as refiner fade [75]. To address this, refiner particles can be delivered as a part of an aluminum master alloy. A master alloy is a pre-alloyed material that allows for the measured addition of refining elements before or during casting. Master alloys are often 90-99wt% aluminum, with the remaining balance being inoculants. This design effectively reduces the density difference of the inoculants and helps initial dispersion and the reduction of refiner fade [8], [76].

For the grain refinement of hypoeutectic Al-Si-Cu alloys, two different master alloy groups are known to work most effectively: aluminum-titanium-boride and aluminum-titanium-carbide [6], [8], [9], [77].

2.4.3 ALUMINUM-TITANIUM-BORIDE GRAIN REFINERS

Al-Ti-B based grain refiners are currently the most common industrial additives used for Al-Si-Cu alloy grain refinement. Depending on the Ti:B ratio, Al-Ti-B master alloys will have three identifiable refining phases present in Al-Si-Cu alloys: aluminum boride (AlB_2), titanium boride (TiB_2) , and titanium aluminide ($TiAl_3$).

The AlB_2 phase is seen at low Ti concentrations or excess B addition, and is not able to effectively grain refine aluminum by heterogenous nucleation due possibly to poor lattice matching (where AlB_2 is a hexagonal C32 structure at a_{AlB2} = 0.301 nm , and α-Al is a standard FCC structure at a_{Al} = 0.405 nm) [6], [9], [78]–[80]. Rather, AlB_2 works by increasing growth restriction of the Al-Si system and early precipitation of α-Al. AlB_2 produces a refined eutectic

reaction of αAl-AlB_2 at a higher temperature than the liquidus temperature. This initiates early nucleation and subsequent grain refinement off of the α-Al phase in the new eutectic [76]. However, AlB_2 was seen to dissolve readily in aluminum and is therefore not an ideal refining phase due to rapid fading [75].

By increasing Ti concentration, to a ratio of 2.2 Ti/B or higher, the TiB_2 phase will precipitate. TiB_2 is an excellent nucleant due to its high chemically stability in aluminum and slow fading properties [75], [76], although the mechanisms of TiB_2 refinement are still under contention. TiB_2 is isomorphous to the AlB_2 crystal structure (hexagonal C32 with a_{TiB2} = 0.303 nm), but the presence of Ti seems to allow for some heterogenous nucleation [9], [78]–[80]. Comprehensive reviews of aluminum grain refinement by Kashyap and Chandrashekar [81], Quested [79], and Murty *et al.* [9] showed that TiB_2 particles are accepted to be responsible for the nucleation of α-Al at low levels of solute Ti (<0.15wt% Ti, known as hypo-peritectic). However, at higher levels of solute titanium (>0.15wt% Ti, known as hyper-peritectic) a $TiAl_3$ phase is produced along side TiB_2. The $TiAl_3$ phase shows much better lattice matching with α-Al (where $TiAl_3$ is a tetragonal $D0_{22}$ structure with a_{TiAl3} = 0.385 nm), but is a poor nucleant alone due to fast dissolution [9], [75]. Recent research by Fan *et al.* [82] and Wang *et al.* [83] has shown that TiB_2 nucleating potency was significantly improved by the coating of a dynamic $TiAl_3$ layer in concentrated Al-Ti solution [9]. The coating of stable TiB_2 by better interfacing $TiAl_3$ supports the many studies showing Al-Ti-B systems to be more effective grain refiners of Al-Si alloys then Al-Ti or Al-B systems alone [9].

For Al-Si-Cu alloys such as the B319 alloy, it has been shown that Al-Ti-B refiners are most effective when added in concentrations of at least 0.10wt% Ti overall, with approximately 10-20 ppm B [84]. Shabestari and Malekan [85] added 0.8-10wt% of Al-5Ti-1B refiner (0.04-0.5wt% Ti) to a commercial 319 alloy. The optimum level of refinement additions was found to be 3.4wt% Al-5Ti-1B (0.17wt% Ti), which caused a reduction of the grain size by ~88%. It was observed however, that grain refiner addition did not affect dendritic arm spacing (DAS) significantly, but rather created a more discontinuous dendritic network with modification of the interdendritic Al-Si eutectic. Ti addition was also seen to change the following solidification points: (i) increased liquidus temperature and lowered liquidus dT/dt peak, (ii) lowered total solidification time, (iii) decreased nucleation undercooling up to 0.17wt% Ti, (iv) decreased recalescence undercooling to zero at 0.17wt% Ti, (v) increased Al-Si eutectic temperatures, (vi) marginally lowered Al-Cu eutectic temperature. Therefore, the above listed points (i)-(vi) are thought to be markers for successful grain refinement with master alloy addition.

2.4.3.1 SYNTHESIS OF ALUMINUM-TITANIUM-BORIDE GRAIN REFINERS

Al-Ti-B refiners can be synthesized in a number of ways, including but not limited to: (i) reaction of fluoride salts with molten alumina, (ii) reaction of oxides with molten aluminum, (iii) thermal reduction and electrolysis, (iv) melting of elemental mixtures, and (v) mechanical alloying [9]. Among the aforementioned methods, a common low temperature (750-800°C compared to 1000°C or more) and low cost method is the reaction of molten aluminum with halide salts [9].

2.4.3.2 POISONING OF ALUMINUM-TITANIUM-BORIDE GRAIN REFINERS

For Al-Ti-B refinement of Al-Si alloys, there is an adverse phenomenon known as poisoning; which is a time dependant mechanism that decreases refiner effectiveness. It has been suggested by Sigworth and Guzowski [86] that for alloys containing more than 2wt% Si, a layer of titanium silicide ($TiSi_2$) would coat the surface of $TiAl_3$ particles and arrest α-Al nucleation. A study by Qiu *et al.* [87] and research by Quested *et al.* [88] confirmed that $TiAl_3$ is more susceptible to coating by $TiSi_2$ than TiB_2, and that this is likely the cause of high losses in grain refiner potency over time in the popular Al-5Ti-1B or Al-3Ti-1B master alloys.

Silicon poisoning is in part thought to be the reason that high B containing master alloys (Al-3Ti-3B for instance) are more effective refiners for Al-Si alloys [76], [89]. However Al-Si-Cu alloys are seen to benefit from higher Ti concentrations, which suggests that the presence of Cu may help to reduce silicide coating [30].

2.4.4 ALUMINUM-TITANIUM-CARBIDE GRAIN REFINERS

For certain applications, the Al-Ti-B master alloy and the presence of TiB_2 have been found to have undesirable side effects, such as the reduction of alloy formability [9]. Additionally, AlB_2 is highly soluble in aluminum and both TiB_2 and $TiAl_3$ can be poisoned by silicon [9], [86]. The carbide theory, first proposed by Cibula [90] in 1972, suggested that other carbides with hexagonal structures could act as effective nucleants for aluminum alloys. This theory sparked research into the use of Al-Ti-C master alloys for grain refinement of aluminum alloys.

In the Al-Ti-C grain refiner, two main phases are responsible for nucleation: $TiAl_3$, and titanium carbide (TiC). TiC possesses a cubic B1 crystal structure, shows good lattice matching with the α-Al phase (where a_{TiC}=0.4315-0.4330 nm), has high chemical stability in aluminum, and has been found to act effectively as an inoculant particle for α-Al dendrites [9], [78], [80], [91].

Al-Ti-C refiners have been shown to effectively reduce the grain size of both pure aluminum and the poisoning-prone Al-Si alloys [92]–[95]. A study by Kumar *et al.* [94] found that Al-Ti-C master

alloys were 10 times as effective on a equivalent weight basis compared to Al-B or Al-Ti-B master alloys. The addition of 0.1wt% Al-Ti-C in a Al-7Si-0.35Mg alloy was seen to give the same refining effect as 1.0wt% Al-B or Al-Ti-B. However, at higher addition levels the Al-Ti-C had drastically reduced efficiency due to suspected TiC agglomeration and Si poisoning.

Another study by Kumar *et al.* [95] compared the effectiveness of Al-Ti-C and Al-Ti-B refiners in an Al-7Si alloy. It was confirmed that Al-Ti-C refiners out perform Al-Ti-B refiners at low addition levels, but are more sensitive to Si poisoning and lose potency past additions of 1wt%. This study also investigated the individual refining responses of $TiAl_3$, TiC, and TiB_2 particles; finding that:

1. $TiAl_3$ particles show more fading compared to TiC
2. TiC and TiB_2 particles are more sensitive to Si poisoning than $TiAl_3$
3. TiB_2 refining potency increases with addition levels
4. $TiAl_3$ refining potency increases with addition levels
5. TiB_2 appears to settle faster than TiC

Recent work by Kumar [19] and Kumar and Bichler [77] tested the refining ability of TiC on the B319 alloy. TiC powder was added directly to the B319 alloy before casting, microscopy and mechanical testing was then performed on the as-cast samples. The optimal addition level was found to be 0.03wt% TiC, which yielded secondary dendritic arm spacing (SDAS) reduction of ~13%. The SDAS reduction was thought to be responsible for the experimental increase in mechanical properties (~36% increase in yield stress and 6% increase in Vickers microhardness).

2.4.4.1 SYNTHESIS OF ALUMINUM-TITANIUM-CARBIDE GRAIN REFINERS

Al-Ti-C refiners have been successfully produced by a variety of methods including: (i) blending of Al and TiC powders [77]; (ii) mixing of molten Al-C and Al-Ti master alloys [96]; or (iii) the high temperature reaction of molten Al, Ti bearing salts, and elemental carbon (such as graphite powder) [9]. The high temperature methods, however, have been found to lead to Al_4C_3 and Ti_3AlC_5 carbide phase formation at prolonged reaction times [97]. These phases are known to poison the master alloy and reduce refiner effectiveness by coating the TiC particles [9].

While carbon containing compounds, such as the TiC ceramic, are well studied additives for aluminum; the use of elemental carbon as a potential refiner or additive is not well researched.

2.4.5 CARBON INOCULATION

Elemental carbon has long been used as an additive and alloying constituent in metal, predominantly in the production of ferrous metals such as cast iron and steel [16]. Although much less common, elemental carbon has also been used as an additive for some non-ferrous metals, most notably as a refiner for Mg-Al alloys or as a general additive for Al alloys.

Qian and Cao [98] performed both an experimental study and comprehensive summary of current literature on the refinement of Mg-Al alloys with elemental carbon containing master alloys. It was found that graphite addition (in the form of fine particles at 0.6wt%C total) showed a grain size reduction of ~60%. The authors proposed that refinement was due to the in-situ reaction of Al-C and the subsequent development of Al_4C_3, or Al_2OC phases. These phases were seen to have good lattice matching parameters and good stability, therefore acting as effective α-Mg nucleants (where Mg is hexagonal with a_{Mg}= 0.3202 nm, Al_4C_3 is rhomboherdral but indexed in a hexagonal unit cell with a_{Al4C3}=0.3329 nm, and where Al_2OC is hexagonal with a_{Al2OC}=0.3170 nm) [98], [99]. It was also found that minimum Al contents of ~2wt% were required to provide effective refinement, strengthening a hypothesis that Al-C systems, such as Al_4C_3, were responsible for the noted refinement [98]. More recent studies by Bhingole and Chaudhari [11], Du *et al.* [100], and Prabhu T [10] confirmed the above findings, that fine elemental carbon powder (either graphite, activated charcoal, or nano carbon black) acts as an effective grain refiner for Mg-Al alloys. For all the supporting research, grain size reduction of at least 50% was seen after the addition of 0.2-1wt% C for Mg-(3,6,8,9)Al alloys. Huang *et al.* [101] proposed that a third phase, Al_2MgC_2, may be responsible for α-Mg refinement. Al_2MgC_2 showed a closely matched hexagonal crystal structure to Mg ($a_{Al2MgC2}$=3.379 nm) and was found in the middle of Mg grains suggesting that it was acting as a preferred nucleation site.

The use of elemental carbon for the refinement or strengthening of aluminum alloys is far less common than Mg-Al, but has gained some industrial and academic attention in recent years. Studies by Mansoor and Shahid [102] and Elshalakany *et al.* [103] have demonstrated that carbon addition, in its nano tube allotrope, can increase the mechanical properties of both pure aluminum and Al-Si alloys. Carbon nano tubes were added at ranges of 0-2.5wt%C by either master alloy Al-C pellets or by straight carbon powder addition. It was found that for both cases tensile strength was increased by a maximum of ~50%, with a smaller accompanying increase in ductility as well. Research by Rong *et al.* [104] however, found that an Al-Cu alloy saw no strength increase but a three fold improvement in ductility with the addition of standard carbon powder at 3wt% C. However, the effects of carbon addition to Al alloy on grain size has not

been well studied. Researchers such as Shon [105], Yang and Scott [106], and Sidhu *et al.* [107], have investigated the interface of Al-C systems (such as an Al-Si alloy reinforced with carbon fibre strands [106]) and saw in-situ development of Al_4C_3 at the Al-C interfaces. Since Al_4C_3 has a closely matched crystal structure to FCC aluminum and seems to readily form at Al-C interfaces, it may be possible that elemental carbon addition could act as an effective inoculant for Al alloys such as the B319 alloy.

While there is currently a relative lack of research into Al-C alloy systems, two recent US patents were filed which describe the use of carbon addition for Al-Si-C and Al-Si-Cu-C alloys similar to the B319 alloy:

Shugart *et al.* [108] received a patent for a aluminum carbon composition, created with the aluminum alloy 356 and 0.02wt% C in the form of activated carbon powder. The carbon powder was added to the molten 356 alloy at ~870°C and then charged with 315 amps. No aluminum carbides or any Al-C matrixes were observed in the final alloy, which allegedly showed grain refinement and improvements in ductility and fracture toughness.

Ijichi and Ohshima [109] received a patent for an Al-Si-Cu-C alloy synthesized by the addition of 0.04wt% C graphite powder to a 319 alloy at 800-1000°C. The inventors claimed that tensile strength increased by ~20% or more. However, boron was also added with the graphite as a "carburization promoter" and the refinement effects of boron may explain the increased mechanical properties, since there was no reported refinement mechanism credited specifically to the graphite addition.

2.4.5.1 CARBON BLACK

Carbon black is a form of amorphous elemental carbon made by the thermal decomposition or partial combustion of hydrocarbon materials [110], [111]. There are two primary production methods for carbon black, referred to as furnace black (most common) and thermal black.

The furnace black process produces carbon black by the pyrolysis of heavy oils, which are first vaporized to produce microscopic carbon particles. The thermal black process produces carbon black by the pyrolysis of natural gas, mainly containing methane.

Unrefined carbon black, often referred to as "soot" or black carbon, can be produced by the combustion of carbon containing fuels such as waste oil, rubber, wood, or plastics. Though, unrefined carbon black typically contains less than 60% elemental carbon with the balance being ash or metals [110].

Carbon black is used for a variety of applications, but is primarily added to rubber as a reinforcement filler, or to paints, plastics, and coatings as a pigment. Carbon black has an extremely high surface-area-to-volume ratio and exhibits a unique aggregate aciniform morphology (seen in Figure 2.10 below), with turbostratic layering of nanoparticles [110].

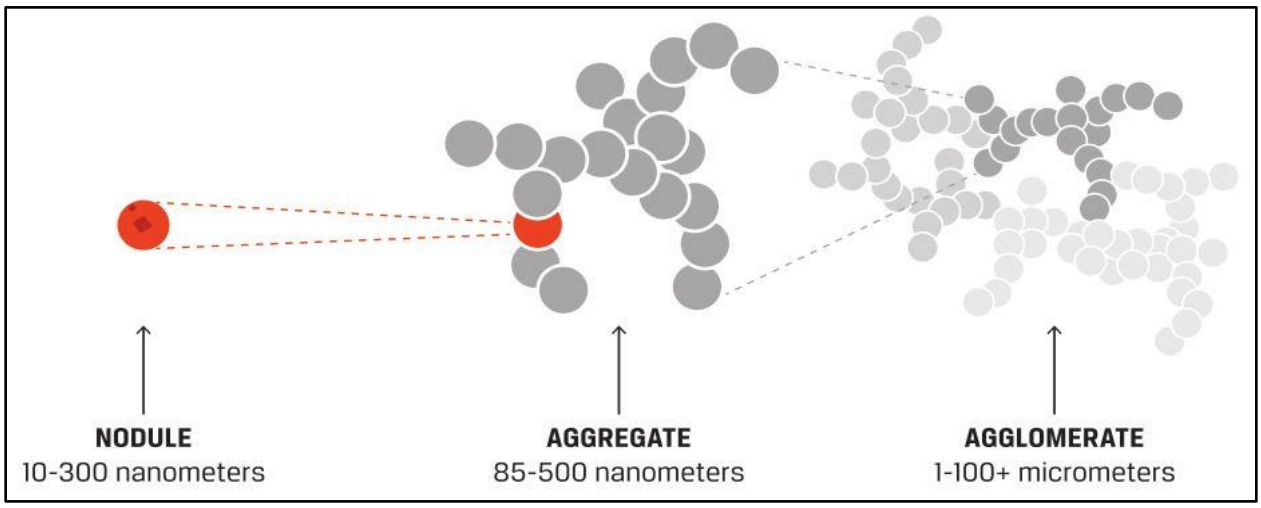

Figure 2.10: Carbon black structure development [110]

Due to its high surface-area-to-volume ratio carbon black could act as an effective inoculant or modifier in aluminum alloys. However, some challenges for inculcation are the of low solubility of carbon in aluminum, poor wetting, and extreme density differences between aluminum and carbon black [7], [111]. Sintering is a method that has been found to help homogenize "dissimilar" materials and previously seen to help disperse carbon allotropes in aluminum.

2.5 SPARK PLASMA SINTERING

Powder metallurgy (PM) is a manufacturing process where bulk materials are sintered together from powders [112]. Sintering typically involves the application of both pressure and heat. However, some sintering processes such as selective laser sintering use only heat. There are many types of sintering operations, two of the most popular techniques are conventional sintering (CS) and hot pressing (HP). In the CS process, powders are first pressed into pucks before being placed in an oven for heat application and sintering [113]. HP processing uses the concurrent application of heat and pressure in which a loaded die of powder is pressed while heat is applied via induction heaters [114]. Both techniques, however, have limitations related to high energy costs, long processing times, and uneven heating. Therefore, to address these limitations, more advanced methods of sintering were developed, such as spark plasma sintering (SPS).

Spark plasma sintering is a relatively novel form of pulsed electric current assisted sintering (PECAS). For this process, powders are loaded into a sintering die, which is placed into the SPS machine. The SPS machine simultaneously applies pressure to the die while on-off direct current (DC) is passed through the powder (for conductive powders). The current creates spark discharge and joule heat points between the individual particles, resulting in localized welding and effective densification [115]. Figure 2.11 and Figure 2.12 below show the SPS process and how joule heating joins conductive particles.

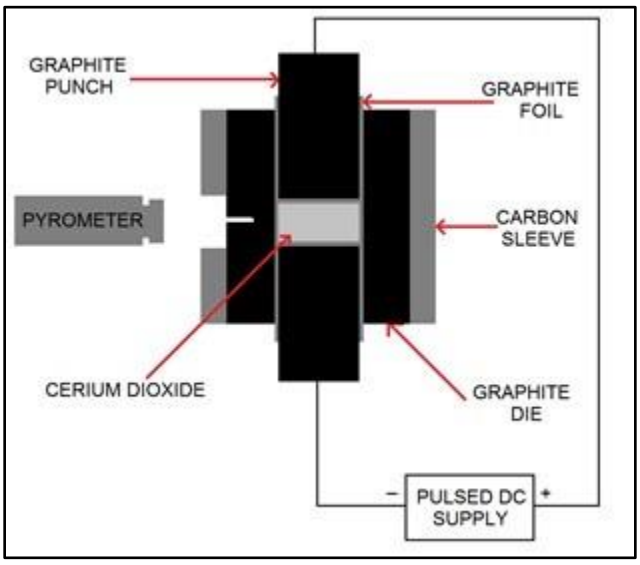

Figure 2.11: SPS process schematic [116]

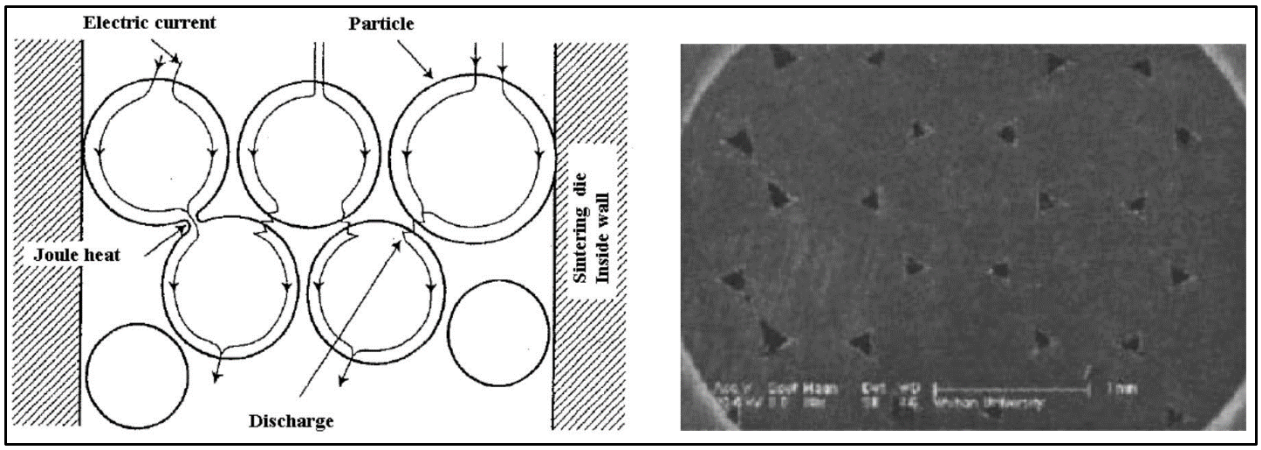

Figure 2.12: SPS current flow; (left) SPS current flow through powder particles [117]*, (right) localized welding of metal particles after SPS* [115]

The SPS process has been noted for its ability to homogeneously densify and join dissimilar particles, such as the sintering of ceramic-metal matrices or metal composites [116], [118]–[120]. Also, the SPS process can be performed in an inert gas atmosphere or under vacuum,

and creates internal joule heating/welding of particles at much lower temperatures than normally required for conventional sintering. Therefore, SPS has been found to effectively densify composite powders without the creation of typical oxides or secondary phases seen in melting or CS [112]–[115].

The advantages of the SPS process have made it feasible for the manufacturing of unique and highly controlled grain refiners. Research by Azad and Bichler [121] showed that the SPS process could be used to successfully manufacture Al-SiC master alloys, which could be used to more easily disperse micro SiC particles into a molten Mg alloy for grain refinement. Additionally, work by Davis *et al.* [122] successfully produced Al-Ti-B master alloys via SPS, which showed a complete homogeneous dispersion of refining particles in the aluminum carrier matrix. Scanning electron microscope (SEM) linescans of the synthesized master alloys showed interfacial diffusion between the matrix material and refining particles, signifying that the SPS process can provide “pre-wetting” of nucleant phases, which is beneficial for dispersion of the inoculant in a carrier metal after grain refiner addition. For the Al-C system specifically, a novel study conducted by Shon [105] showed that under the application of either positive or negative DC, aluminum to carbon wettability could be increased. Sessile drop tests were performed in which a molten drop of pure Al was put in contact with a graphite plate, and then a small electrode was used to run a current of between 0-15A through the Al and graphite. It was found that high currents of 10-15A significantly improved the wettability of Al on graphite, decreasing the contact angle by more than 40% and accelerated the growth of an Al_4C_3 layer at the Al-C interface. Shon then also performed the same experiments on less dense graphite plates (70% relative density compared to 100% relative density for the first tests) and found that wettability increased even further and the Al_4C_3 was found to triple in thickness, from ~30nm to ~90nm.

The above research suggests that the use of the SPS technique in the synthesis of an Al-C master alloy will likely function to increase Al-C wettability and help better disperse the carbon inoculants in the metal for grain refining.

CHAPTER 3: EXPERIMENTAL PROCEDURE

In this chapter, the details pertinent to all experimental procedures for the synthesis, processing, and evaluation of all materials investigated in this thesis are discussed.

3.1 CHAPTER OUTLINE

As outlined in Chapter 1, the objective of this thesis was to study the effect of carbon inoculants on the as-cast B319 alloy's structure and properties. To gain a comprehensive quantitative overview of the effect, the following sections outline the characterization performed after each experimental stage:

Section 3.2: Raw materials

Outlines the specifications of the materials used to prepare the master alloys and as-cast alloys.

Section 3.3: Master alloy synthesis

Details on the equipment and procedures used for master alloy production: precursor experiments, powder preparation, spark plasma sintering (SPS), and casting preparation.

Section 3.4: Casting experiments

Provides an overview of the alloy casting procedure and the equipment involved.

Section 3.5: Alloy analysis

Describes the procedures implemented for mechanical testing, microstructure and material characterization, and statistical analysis.

3.2 RAW MATERIALS

Commercially available samples of the B319 alloy were received from the Nemak Windsor Aluminum Plant. The material ingots were used for all casting experiments. The chemical composition of the recieved B319 alloy is outlined in Table 3.1.

Table 3.1: Chemical composition of the B319 alloy

Elements	Si	Cu	Zn	Fe	Mn	Ti	Ni	Cr	Mg	Other	Al
wt%	5.95	3.14	0.93	0.64	0.29	0.17	0.15	0.07	0.05	0.11	balance

The chemical analysis results obtained via SEM/energy-dispersive x-ray spectroscopy (EDXS) were in accordance with ASTM B179-17, Standard Specification for Aluminum Alloys [17].

The master alloys prepared to treat the B319 alloy were synthesized by the SPS machine at the University of British Columbia Okanagan campus (UBCO). Pure aluminum powder was used as a matrix, while two grades of carbon black powder were investigated as inoculants. The general specifications for each powder are listed in Table 3.2, while the chemical composition checked by EDXS are provided in Table 3.3 and Table 3.4.

Table 3.2: Master alloy raw powder specifications

Powder	Average Particle Size (μm)	Purity (%)	Source	Product No.	CAS No.	Lot No.	Surface Area (m^2/g)	Bulk Density (g/L)
Al	40.0	99.8	Alfa Aesar	00010	7429-90-5	W01B002	n/a	n/a
C_A	n/a	99.9+	Alfa Aesar	45527	1333-66-4	Q29C020	75	170-230
C_R	n/a	~81	Recycled Carbon Black	n/a	n/a	n/a	n/a	n/a

Table 3.3: Chemical composition of Al powder

Elements	O	Ag	Al
Wt.%	1.24	0.76	Balance

Table 3.4: Chemical composition of C_R carbon black powder

Elements	O	Zn	S	Si	C
Wt.%	10.00 – 10.5	2.5 - 4	1.5 - 2	0.5 - 1	Balance

3.3 MASTER ALLOY SYNTHESIS

Two sources of carbon were used for all casting experiments: (i) a high purity carbon black from a commercial supplier (Alpha Aesar), and (ii) a recycled carbon black from a pyrolysis process.

A total of four master alloys were prepared with these two carbon sources:

1) Alpha Aesar carbon black high concentration (AH) master alloy
2) Alpha Aesar carbon black low concentration (AL) master alloy
3) Recycled carbon black high concentration (RH) master alloy
4) Recycled carbon black low concentration (RL) master alloy

Before being tested in casting experiments, precursor experiments were performed to determine preparation parameters and compositional limits of the master alloys. Afterwards, master alloy powders were prepared and sintered following the procedures outlined.

3.3.1 PRECURSOR EXPERIMENTS

In the early stages of this research, preliminary experiments were performed to determine an optimal method to prepare Al-C powder blends. Also, the optimal level of master alloy addition to the B319 alloy was investigated.

PRELIMINARY TRIALS ON POWDER BLENDING

The powder blend preparation trials were conducted to address the challenge of mixing carbon black powder with the aluminum matrix powder. The objective of the trials was to achieve a homogeneous dispersion of carbon black in the aluminum matrix powder.

During this stage of research, a total of 11 blends were prepared. These blends were prepared subject to varying mixing method (ball mill or manual stir mixing), suspension fluid (water, alcohol, or dimethylformamide), and varying processing parameters. It was determined that manual stir mixing, with alcohol was the most effective method for carbon black dispersion (further discussed in Section 3.3.2 and Chapter 4).

PRELIMINARY TRIALS ON MASTER ALLOY COMPOSITION

The master alloy composition trials were performed to determine the maximum weight percentage of carbon that could be successfully sintered to form an as-sintered pellet with optimal integrity and homogeneity (i.e., to allow the pellet to be added into the liquid B319 alloy). Three carbon concentration levels initially studied were: 2wt%, 5wt% and 10wt% C.

The Al-2wt%C as-sintered pellet had the most favourable densification and homogeneity (further discussed in Chapter 4). Therefore, it was selected as the “high” concentration master alloy. An Al-1wt%C master alloy was then prepared and used in subsequent experiments to study the effect of the Carbon concentration on the B319 alloy (further discussed in Chapter 4). This master alloy was termed as the “low” concentration master alloy.

CAST ALLOY COMPOSITION TRIALS

Using the Al-2%C master alloy, three castings were prepared to determine the effect of the overall Carbon concentration on the B319 alloy’s microstructure. The following carbon concentrations were explored: 0.01wt% C, 0.03wt% C, and 0.10wt% C.

The castings were prepared with the thermal mold and as-cast grain size was evaluated. The 0.03%wt C addition level showed the highest degree of grain refinement and thus was used for subsequent tests with the B319 alloy. This selection was in agreement with literature [77][9].

3.3.2 POWDER PREPARATION

To prepare an Al-C master alloy for sintering, aluminum powder and carbon black powder were weighed out on a scale (Fisher Scientific, module No. ALF204, +/- 0.0005g). Table 3.5 shows the total composition of each master alloy when processed in a 60mm SPS die. The 60mm die was able to yield ~120g of the Al-C powder mixture.

Table 3.5: Master alloy composition

Master Alloy	Aluminum		Carbon Black			Total Weight (g)
	Weight (g)	Composition (wt.%)	Weight (g)	Composition (wt.%)	Carbon Black Source	
AH	117.6	98.0	2.4	2.0	C_A	120.0g
AL	118.8	99.0	1.2	1.0	C_A	120.0g
RH	117.6	98.0	2.4	2.0	C_R	120.0g
RL	118.8	99.0	1.2	1.0	C_R	120.0g

After weighing, the powders were added together into a beaker and mixed with denatured alcohol until reaching a flowable slurry. This slurry was continuously stirred manually with a glass stir stick on a hot plate (set at 80°C) until reaching a wet sand consistency with uniform colour and carbon dispersion. The mixture was then immediately removed from the hot plate and scooped into the prepared SPS die.

It was observed that if the Al-C mixture was too dry it would begin separating while loading the die. Consequently, the mixture was scooped into the die while still wet (wet sand consistency) to retain carbon dispersion before sintering.

3.3.3 SPARK PLASMA SINTERING

The following sections describe the sintering machine, procedure, and program used for all master alloys synthesized in this work.

3.3.3.1 SINTERING MACHINE

All sintering was done with a Thermal Technologies LLC 10-3 SPS machine. The 10-3 SPS machine consisted of the following:

1. **Process Control and Data Acquisition System:** The SPS hydraulic pressure, atmospheric chamber pressure, and sintering temperature were independently

controlled by an Eurotherm controller using loop control method. The sintering program was programmed via iTools software and was subsequently uploaded to the Eurotherm controller. A laptop connected to the SPS machine acted as a data acquisition (DAQ) system via a SpecView software.

2. **Power Supplies:** SPS power was delivered by ON-OFF pulsed DC from three 1000-amp power supplies.
3. **Hydraulic System:** The hydraulic system, containing a single overhead ram and hydraulic pump, served to apply pressure to the sample-die assembly during sintering.
4. **Vacuum System:** Before SPS processing, the sintering chamber of the SPS machine was evacuated of atmospheric air to prevent high temperature oxidation of the sample or graphite tooling. In the present research, the sintering chamber was evacuated and then backfilled with inert argon.

3.3.3.2 SINTERING PROCEDURE

The following steps were carried out for all sintering trials:

Step 1: Two layers of 0.005” thick grafoil were placed on the inner diameter of a graphite die (90mm OD, 60.6mm ID, 80mm H). The Grafoil was added to reduce friction in the die during the sintering process, and to prevent the sintered sample from adhering to the graphite die ID walls. Further, the Grafoil between the punches and the die ID ensured that there was a tight tolerance fit preventing material from squeezing out during sintering.

Step 2: A graphite punch (Ø60mm, 50mm H) was inserted into one end of the cylinder (this punch was only inserted the minimum distance required to remain secure). On top of this punch, a graphite disk (Ø60mm, 5mm H) was placed inside the die cavity, followed by a disc of Grafoil.

Step 3: The die was filled with the wet Al-CB mixture. The powder mixture was manually packed down until flat. A Grafoil disk was placed on top of the powder surface, followed by inserting the top punch.

Step 4: The closed die assembly was heated in an oven set at 150°C for three hours. Heating the die assembly helped to evaporate any remaining alcohol, which greatly reduced the time required to pull a vacuum in the sintering chamber.

Step 5: The die assembly was removed from the oven and placed in the SPS sintering chamber, ensuring that the SPS thermocouple was inserted into the bottom punch and a carbon insulating sleeve placed over the die before the rams were set.

Figure 3.1 illustrates the proper packing order of the assembly and renderings of the completed die in the sintering chamber.

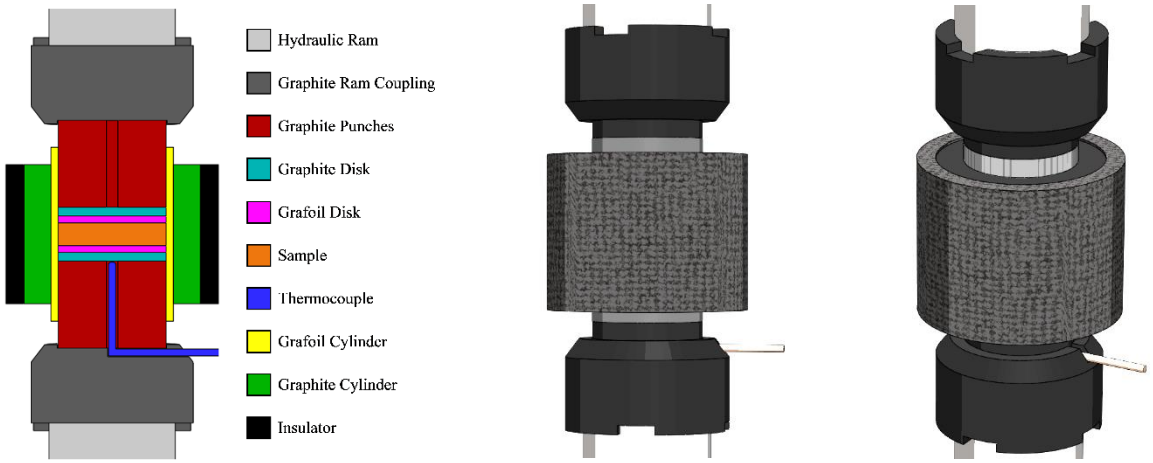

Figure 3.1: Loaded SPS die CAD model; (a) packing order for loaded SPS die, (b) front view rendering of loaded SPS die, (c) dimetric view rendering of loaded SPS die.

Each sintered master alloy sample was 60mm in diameter, approximately 17.5mm in height, and weighed 120g. A representative sample is shown in Figure 3.2.

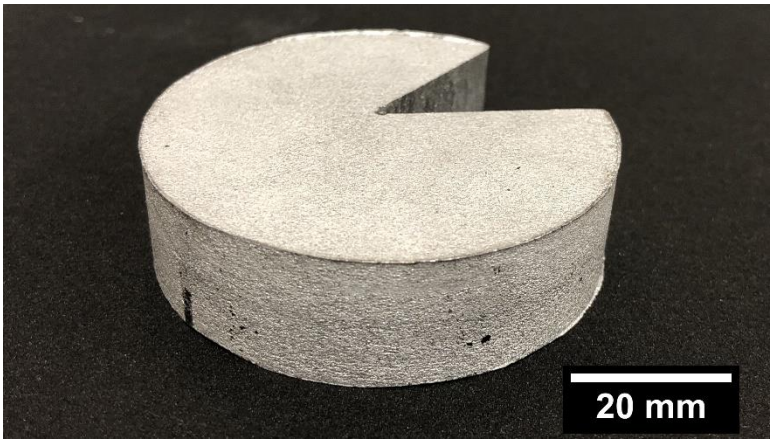

Figure 3.2: 60mm Al SPS sample

3.3.3.3 SPS SINTERING PROGRAM

Using iTools software and a laptop connected by ethernet to the SPS machine, a sintering program was created and automatically run for each sample.

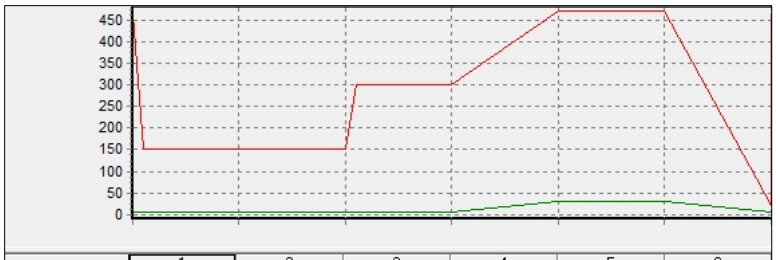

	1	2	3	4	5	6
Type	Profile (0)	Profile (0)	Profile (0)	Profile (0)	Profile (0)	Profile (0)
UsrTxt	Default Text	Default Text	Default Text	Default Text	Default Text	Default Text
PSP1Tp	Ramp (3)	Dwell (2)	Ramp (3)	Ramp (3)	Dwell (2)	Ramp (3)
PSP1Tg	150.00	150.00	300.00	470.00	470.00	20.00
PSP1Rt	100.00		100.00	50.00		100.00
PSP1Dw		10s			6m	
PSP1HT	Coarse Lo (4	Off (0)	Off (0)	Coarse Lo (4	Coarse Lo (4	Coarse Lo (4
PSP2Tp	Dwell (2)	Dwell (2)	Dwell (2)	Ramp (3)	Dwell (2)	Ramp (3)
PSP2Tg	5.00	5.00	5.00	30.00	30.00	5.00
PSP2Rt				10.00		10.00
PSP2Dw	0	0	0		6m	
PSP2HT	Off (0)	Off (0)	Off (0)	Off (0)	Off (0)	Off (0)
P_DOut	..	..	..	..	..	..

Figure 3.3: Screenshot of iTools software and the sintering program run for MA synthesis

Figure 3.3 above shows the iTools interface and the six-step sintering program used for all master alloy synthesis (temperature and pressure refer to the temperature and pressure occurring locally at the sample site, within the SPS die):

1. Ramp temperature from room temperature to 150°C at 100°C/min. Dwell pressure at 5 MPa.
2. Dwell temperature at 150°C for 10 seconds. Dwell pressure at 5 MPa.
3. Ramp temperature to 300°C at 100°C/min. Dwell pressure at 5 MPa.
4. Ramp temperature to 470°C at 50°C/min. Ramp pressure to 30 MPa at 10 MPa/min.
5. Dwell temperature at 470°C for 6 minutes. Dwell pressure at 30MPa for 6 minutes.
6. Cool to room temperature. Ramp pressure down to 5MPa at 10MPa/min. Program End.

This procedure was developed based on extensive trial-and-error experiments carried out by the author and a colleague (Mr. Justin Mok).

3.4 CASTING EXPERIMENTS

The following section outlines the casting experiments carried out in this research. The equipment, casting methods, test specifications and exact procedures for each of the three mold set-ups utilized (i.e., thermal mold, mechanical testing mold, and fluidity mold) are presented.

3.4.1 EQUIPMENT

All casting experiments were performed at the UBC-O metal casting laboratory. The equipment used for all casting trials consisted of:

1. **Melting furnace:** A cylindrical, top-loading, electric resistance furnace that was used to melt the alloys (Euclid R-85 furnace, Figure 3.4-Left).
2. **Preheat furnace:** A rectangular, front-loading, electric resistance furnace that was used for preheating master alloys and molds (Euclid CF 510 furnace, Figure 3.4-Centre).
3. **Casting stage:** A hydraulic scissor lift that was used as an adjustable pouring table (Figure 3.4-Right).

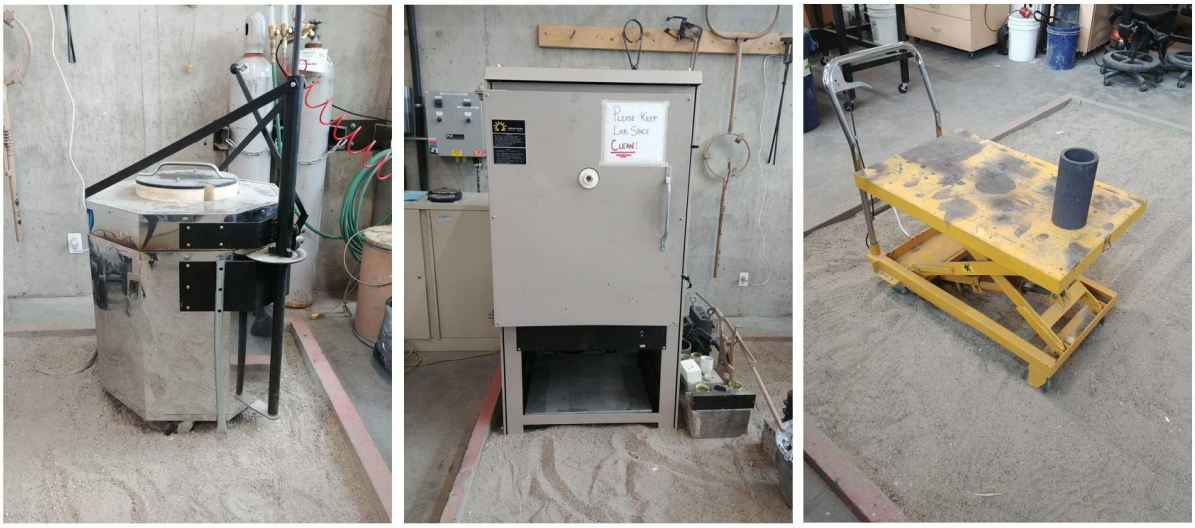

Figure 3.4: Casting equipment; (left) melting furnace, (centre) preheat furnace, (right) casting stage

4. **Shielding gas system:** The shielding gas system was used to create an inert gas atmosphere atop the crucible, thereby preventing oxidation of molten alloys while stirring and holding. The system contained a CO_2 tank, heated flow regulator, and a portable lance; delivering CO_2 at an output temperature of 65°C and flow rate of 7 LPM.

Figure 3.5: Shielding gas system

5. **Thermocouples:** OMEGA K-type thermocouple probes of various sizes were used for measuring mold, metal, and furnace temperatures.
    a. **Small:** Used for reading alloy solidification temperature in the thermal mold. A 304SS sheath probe, Ø0.02” x 24”; rated to 1250°C ± 0.4% (P/N: HKMTSS-020E-24).
    b. **Medium:** Used for reading thermal and fluidity mold temperatures. A 304SS sheath probe, Ø0.062” x 24”; rated to 1250°C ± 0.4% (P/N: KMQSS-062G-24).
    c. **Large:** Used for reading molten alloy temperature. An OMEGACLAD Ni-Cr sheath probe, Ø0.25” x 28”; rated to 1250°C ± 0.4% (P/N: TJ36-CAXL-14G-28).
6. **Heating tape system:** The heating tape was used for preheating the thermal mold. The tape was controlled with a closed loop thermostat with a medium thermocouple line, which operated ON-OFF DC heating. The heating tape was an OMEGA ultra-high temperature heating tape (P/N: STH051-080).

Figure 3.6: Heating tape system; (left) Omega heating tape wrapped around thermal graphite mold, (right) thermostat and heating tape power source

7. **Crucibles:** Two sizes of Silicon carbide crucibles were used for the melting, mixing, and casting of alloys:
    a. **Small:** A #3 Bilge Mars ISOMELT-I-M crucible, purchased from Smelko Foundry Products (Figure 3.7-Right).
    b. **Large:** A #60 Bilge Mars ISOMELT-I-M crucible, purchased from Smelko Foundry Products (Figure 3.7-Left).

Figure 3.7: Silicon carbide crucibles; (left) large crucible, (right) small crucible.

8. **Insulation:** Alumina-silica fibre batting was used for insulation of the thermal mold and fluidity mold. The batting was cut to shape from 2” thick Fibrefrax blanket, purchased from UNIFRAX.
9. **DAQ System:** The DAQ system was used for in-situ temperature data collection during alloy solidification in the thermal mold and fluidity mold. The system consisted of an OMEGA DAQ module (P/N: OMB-DAQ-56) connected by USB to a laptop. The laptop ran Personal DaqView software to configure and record data from the DAQ module in Microsoft Excel.
    a. **Thermal Mold:** One thermocouple was attached at a 5.0 Hz sampling frequency.
    b. **Fluidity Mold:** Five thermocouples were attached at a 1.553 Hz sampling frequency.
10. **Casting Molds:** Three types of casting molds were used for this research:
    a. **Thermal Mold:** Made from 2” medium extruded graphite rod, purchased from The Graphite Store (P/N: GR060-ROD-2OD) – See Section 3.4.3.
    b. **Mechanical Mold:** Made from 4” medium extruded graphite rod, purchased from The Graphite Store (P/N: GR060-ROD-4OD) – see Section 3.4.4.
    c. **Fluidity Mold:** Made from 1020 steel – see Section 3.4.5.

3.4.2 EXPERIMENTS PERFORMED

The casting experiments performed in this research were carried out using three mold configurations: the thermal mold, the mechanical mold, and the fluidity mold. Each of these molds was used to test several alloy compositions to study the effect of carbon inoculation on the as-cast B319 alloy. Table 3.6 summarizes the casting experiments performed for each mold type.

Table 3.6: Casting experiments performed, organized by mold category

	Casting Experiments		
	Thermal Mold	Mechanical Mold	Fluidity Mold
Alloy Compositions Tested	Virgin B319	Virgin B319	Virgin B319
	Pure Aluminum	AH	AH
	AH	AL	AL
	AL	RH	RH
	RH	RL	RL
	RL		
	B319CC		
	AHCC		
Total Castings performed	20	10	14

The alloy compositions that were investigates were as follows:

1. **Virgin B319 alloy:** Casting trials with this material were carried out to establish a benchmark for mechanical properties, microstructure and solidification behavior.
2. **Pure aluminum:** A SPS pellet of pure aluminum was cast as an additional control, often denoted as PAl.
3. **AH and RH:** A high concentration master alloy (2.0wt%) synthesized with either C_A (AH) or C_R (RH), were added to the B319 alloy.
4. **AL and RL:** A low concentration master alloy (1.0wt%) synthesized with either C_A (AL) or C_R (RL), were added to the B319 alloy.
5. **B319CC:** Select tests at a lower pouring temperature were carried out with the virgin B319 alloy. These castings were labeled as B319CC.
6. **AHCC:** AHCC stands for “AH cold casting”, in which a high concentration master alloy (2.0wt%) with Alpha Aesar’s carbon black was added to the B319 alloy and cast at the same lower pouring temperature as in the case of B319CC.

A casting was deemed unsuccessful if its pouring temperature or mold temperature varied by more than 10°C, or if an oxide was inadvertently trapped in the casting, thereby affecting its integrity. All unsuccessful castings were repeated.

3.4.3 THERMAL MOLD

Following the works of Kumar and Bichler [77], and research by Murty *et al* [9], a standardized graphite mold design was selected to study the effects of grain refinement on the B319 alloy's solidification and the resulting microstructure.

The graphite thermal mold was manufactured at the UBCO machine shop from 2" medium extruded graphite rod, with dimensions given in Figure 3.8.

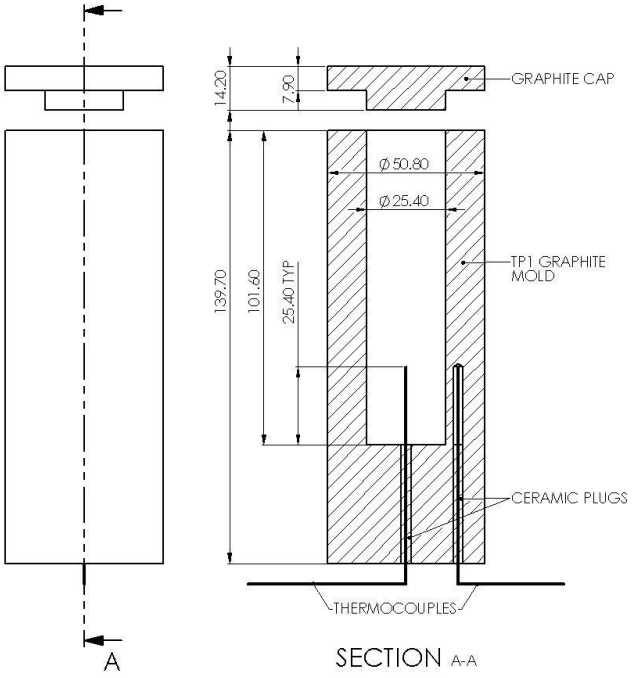

Figure 3.8: TP1 mold drawing (dimensions in mm)

To preform a Newtonian thermal analysis, the mold was fitted with two thermocouples. The first small thermocouple was inserted into the bottom hole. The second medium outer thermocouple was connected to the heating tape system controller, which was used to hold the mold at a specific preheat temperature. Each thermocouple was inserted into the graphite so that the point of measurement was taken 25.4mm from the base of the solidifying sample.

The following set-up and casting procedure was followed for all thermal mold experiments:

Set-up

1. The center and outer thermocouples were inserted into the graphite mold.
2. The graphite mold was wrapped with heating tape, covered with a layer of insulation blanket, placed on an insulating fire brick, and then pre-heated to 350°C, as seen in Figure 3.9 below.

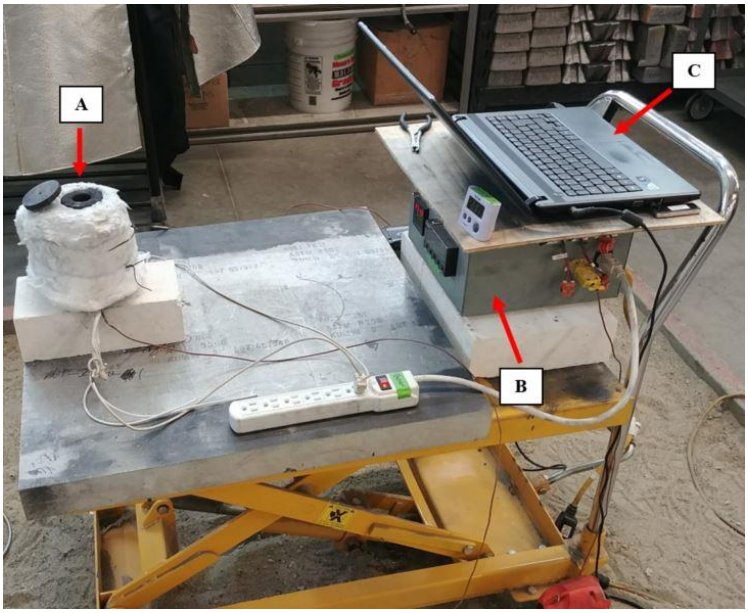

Figure 3.9: Thermal mold set-up; (a) mold, heating tape, and insulation assembly, (b) heating tape controller, (c) laptop and DAQ unit (DAQ unit not visible)

3. The melting furnace was set to 750°C and approximately 155g of the B319 alloy was cut from an ingot using a vertical band saw.
4. Using the above recorded mass of the B319 alloy, the required amount of master alloy to achieve 0.03wt% C was weighed out and wrapped in an sheet of aluminum foil. This foil package was placed into the mold furnace set at 350°C for preheating.
    a. For high concentration additions (AH and RH), Equation 3.1 below was used to determine the required weight of master alloy (W_H).
    b. For low concentration additions (AL and RL), Equation 3.2 below was used to determine the required weight of master alloy (W_L).

$$W_H = \left(\frac{3}{197}\right) W_{B319} \quad \textbf{3.1}$$

$$W_L = \left(\frac{3}{97}\right) W_{B319} \quad \textbf{3.2}$$

Where: W_{B319} = weight of the B319 alloy.

Casting Procedure

1. The sectioned B319 alloy was placed into a small crucible and loaded into the melting furnace. The furnace was heated until the molten alloy reached proper temperature, verified by a large thermocouple:
    a. 715°C for virgin B319 castings.
    b. 730°C for master alloy additions (PAl, AH, RH, AL, RL) castings.
    c. 700°C for B319CC castings.
    d. 710°C for AHCC castings.
2. Using a stainless steel perforated ladle, the melt was skimmed of slag.
3. Immediately after skimming, the melt was flooded with CO_2 from the shielding gas system to prevent oxidation of the freshly exposed molten surface. The aluminum foil package with carbon black was taken out of the mold furnace, added to the melt, and then stirred with a large thermocouple for ~80 seconds until all master alloy blocks were dissolved.
4. After mixing, the shielding gas was removed, and the molten alloy was held in the furnace for two minutes before reaching a temperature of:
    a. 715°C for PAl, AH, RH, AL, and RL castings.
    b. 685°C for AHCC castings.
5. The DAQ system was then started and the crucible was removed from the furnace and skimmed once more immediately before pouring at a temperature of:
    a. 710°C for virgin B319, PAl, AH, RH, AL, and RL castings
    b. 680°C for B319CC and AHCC castings.
6. Ten minutes after pouring, the DAQ system was stopped, the graphite mold was removed from the fibre batting, the thermocouples were cut, and the casting was left to cool in the graphite cylinder until it could be easily ejected.

3.4.4 MECHANICAL MOLD

To enable ASTM-compliant mechanical testing of the novel alloys, a custom graphite mold was designed and fabricated.

The graphite mechanical mold was manufactured at the UBCO machine shop from 4” medium extruded graphite rod and is shown in Figure 3.10.

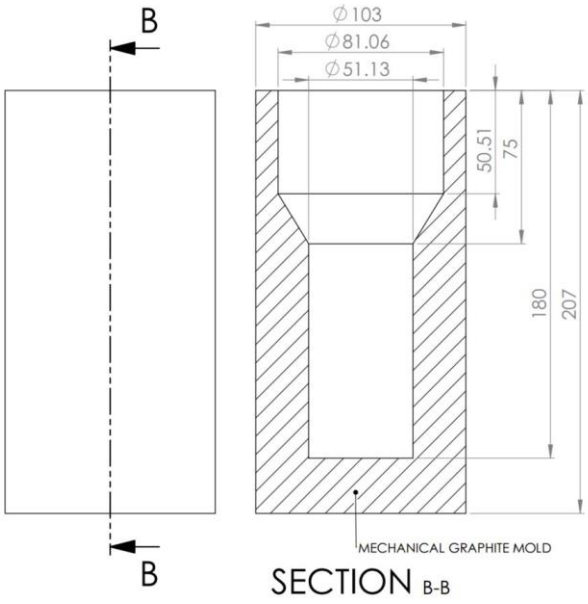

Figure 3.10: Mechanical mold drawing (dimensions in mm)

The graphite mechanical mold was sized in such a way that a minimum of two tensile samples and two Charpy samples could be extracted (explained further in Section 3.5.1.2).

The following set-up and casting procedure was followed for all experiments with the graphite mechanical mold:

Set-up

1. The graphite mechanical mold was loaded into a furnace and preheated to 350°C, while the melting furnace was preheated to 770°C.
2. Approximately 1300g of material was cut from the B319 alloy ingot using a vertical band saw.
3. The required amount of master alloy to achieve 0.03wt% C was weighed out and wrapped in an aluminum foil. This foil package was then placed into the mold furnace to preheat.
    a. For high concentration additions (AH and RH), Equation 3.1 was used to determine the required weight of master alloy.
    b. For low concentration additions (AL and RL), Equation 3.2 was used to determine the required weight of master alloy.

Casting Procedure

4. The sectioned B319 alloy was placed into a large crucible and loaded into the melting furnace.
5. The B319 alloy material was heated in a large crucible until the molten alloy reached a target temperature of:
    a. 715°C for virgin B319 castings.
    b. 760°C for master alloy addition castings.
6. Using a stainless steel perforated ladle, the melt was skimmed of slag.
7. The melt was then flooded with CO_2 from the shielding gas system to prevent oxidation of the molten surface. The master alloy in the aluminum foil was taken out of the furnace and stirred-in for ~130 seconds with a large thermocouple until dissolved. During mixing, the melt temperature dropped by ~20°C.
8. After mixing, the shielding gas was removed, and the molten alloy was held in the furnace for two minutes before reaching a temperature of 750°C. Then, the crucible was removed from the furnace and skimmed once more immediately before pouring at a temperature of 710°C.

3.4.5 FLUIDITY MOLD

The fluidity mold was custom designed and manufactured at UBCO based on research by Dahle *et al* [123], Di Sabatino *et al* [124], and Caliari *et al* [125]. This mold was used to test the effect of carbon black inoculation on the fluidity of the B319 alloy.

The fluidity mold, seen in Figure 3.11 and Figure 3.12, consisted of a lower spiral plate, upper head plate, and two-part removable down sprue. The spiral plate and head plate assembly (Figure 3.12-C) were machined on a 5-axis computer numerical control (CNC) milling machine from 0.5” thick 1020 steel plate. The spiral itself had a total length of 1020mm (measured from the centre-tip to the beginning of the flow path, denoted by the red dot in Figure 3.12-C) and a cross sectional area of 56mm^2. The head plate had four medium thermocouples welded into holes indexed every 102mm along the flow path (the four wires seen on top of the mold in Figure 3.12-A). These thermocouples were welded into the holes so that their tips were level with the head plate underside and could gather temperature of the solidifying alloy. The head plate also had pins located on two sides of the down sprue to ensure quick and precise alignment of the system before casting. The down sprue assembly (Figure 3.12-B) was machined manually by mill and lathe from 2” thick 1020 steel plate. The down sprue halves

were aligned with internal pins and then secured with a carriage clamp prior to casting (Figure 3.12-A).

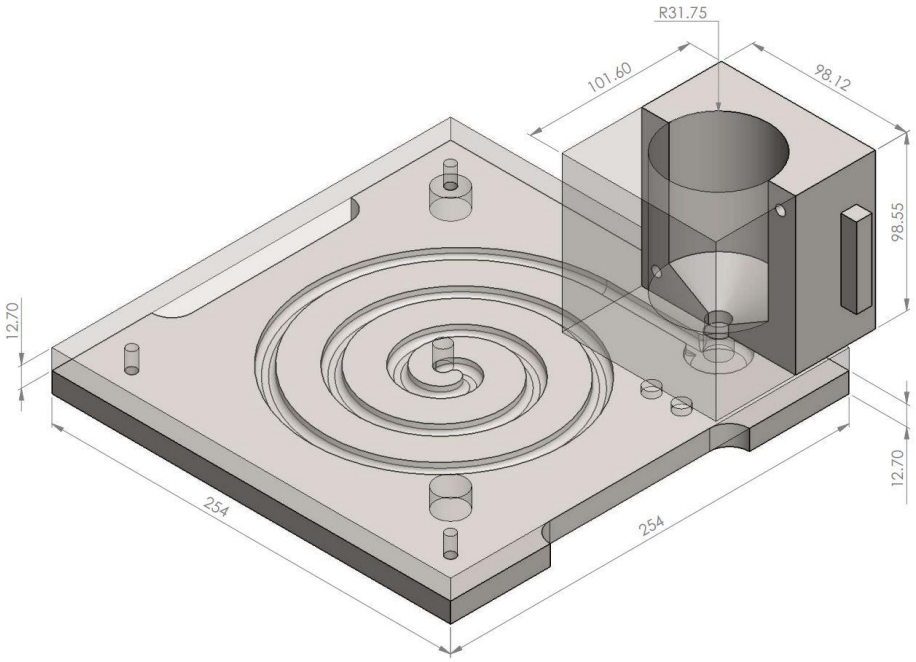

Figure 3.11: Fluidity mold CAD model (dimensions in mm)

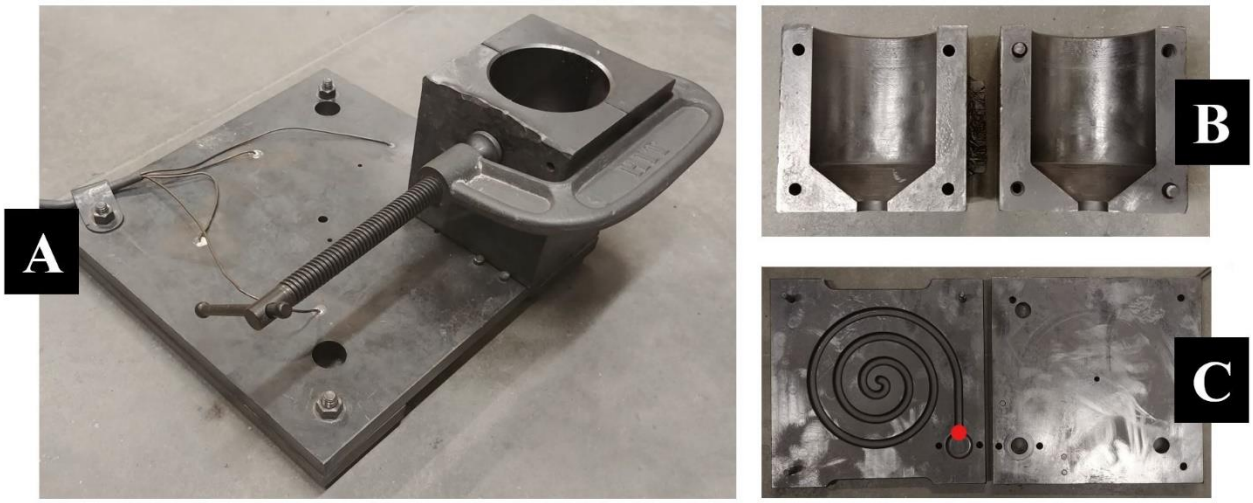

Figure 3.12: Fluidity mold; (a) assembly, (b) open down sprue, (c) open cope and drag

In addition to the mold assembly, a plug rod was also fabricated as seen in Figure 3.13 below. During casting, the plug was manually held in the down sprue (Figure 3.14) until the molten B319 alloy filled the entire downsprue. Thereafter, the plug was removed to enable liquid metal to enter the spiral mold cavity. The use of this plug helped remove experimental variation due to

manual pouring and variation in the flow rate. The plug rod was made from a 0.5” carriage bolt welded onto 0.5” round steel rebar bent at a 90° angle. The rod also had a medium thermocouple, which was using the melt temperature prior to forming the casting.

Figure 3.13: Fluidity mold plug rod

Figure 3.14: Fluidity mold plug rod placement

The following set-up and casting procedure was followed for all fluidity mold experiments:

Set-up

1. All interior surfaces of the fluidity mold were coated with graphite lubricant to aid in casting ejection (Jig-A-Loo extreme temperature graphite lubricant, P/N: 03815022).
2. The fluidity mold thermocouples and plug rod thermocouple were attached to the DAQ system. The mold assembly was then placed into the mold furnace at 315°C to preheat (long leads on the thermocouple wires were used so that the mold could remain attached to the DAQ system while preheating and casting).

3. The melting furnace was set to 780°C and the head of the plug rod was placed into the furnace for preheating.
4. Approximately 670g of the B319 alloy was cut from an ingot using a vertical band saw.
5. Using the above mass of the B319 alloy, the required amount of master alloy to achieve 0.03wt% C was weighed out and wrapped together with aluminum foil. This foil package was then placed into the mold furnace with the fluidity mold to preheat.
    a. For high concentration additions (AH and RH), Equation 3.1 was used to determine the required weight of master alloy.
    b. For low concentration additions (AL and RL), Equation 3.2 was used to determine the required weight of master alloy.

Casting Procedure

6. The sectioned B319 alloy was placed into a small crucible and loaded into the melting furnace.
7. The B319 alloy was heated until the metal reached a desired temperature, verified by a large thermocouple:
    a. 750°C for virgin B319 castings.
    b. 775°C for master alloy addition castings.
8. Using a stainless steel perforated ladle, the melt was skimmed of slag.
9. The melt was then flooded with CO_2 from the shielding gas system to prevent oxidation of the molten surface. The master alloy package was taken out of the mold furnace and added to the melt, stirring for ~75 seconds with a large thermocouple until all master alloy blocks were dissolved. The melt dropped ~30°C during the mixing phase.
10. After mixing, the shielding gas was removed, and the molten alloy was held in the furnace for approximately three minutes before reaching a temperature of 750°C.
11. The fluidity mold assembly was removed from the mold furnace and placed on the casting stage, sandwiched between two layers of insulation blanket (see Figure 3.15). The DAQ system was then started and the mold assembly was left on the casting stage for 90 seconds, cooling from 315°C to 310±5°C.

    For master alloy addition castings, the mold assembly was set out 90 seconds after the mixing phase so that the mold reached 310±5°C by the end of the three-minute holding phase.

Figure 3.15: Insulation of the fluidity mold

12. The plug rod was positioned in the down sprue (see Figure 3.14), while the melt was removed from the furnace, skimmed, and then immediately poured into the mold at ~740°C. The down sprue was filled in under two seconds and then the plug rod was lifted, allowing the molten alloy to flow into the mold.

3.5 MATERIAL CHARACTERIZATION

This section outlines the procedures and equipment used for the analysis and characterization of all raw, as-cast, and SPS alloys used in this research.

3.5.1 MECHANICAL TESTING

Three separate tests were conducted to evaluate the mechanical response of the as-cast materials: hardness test, tensile test, and Charpy V-notch impact tests. Each test was conducted at UBCO using the following procedures and equipment.

3.5.1.1 HARDNESS

Vickers microhardness tests were performed using the principles outlined in ASTM standard E384-11^{E1} [126], using a Wilson VH Tukon 3100 automatic hardness tester.

The hardness measurements were performed on the cast samples produced in the thermal mold after completing grain size measurement and general microscopy evaluation.

The hardness tester was set for a load of 0.2 kg (1.961N), a 15 second dwell time, and used a 4 x 4 measurement grid for each sample (3mm x 3mm). The corner of the matrix began at the centre of the casting as seen in Figure 3.16 below.

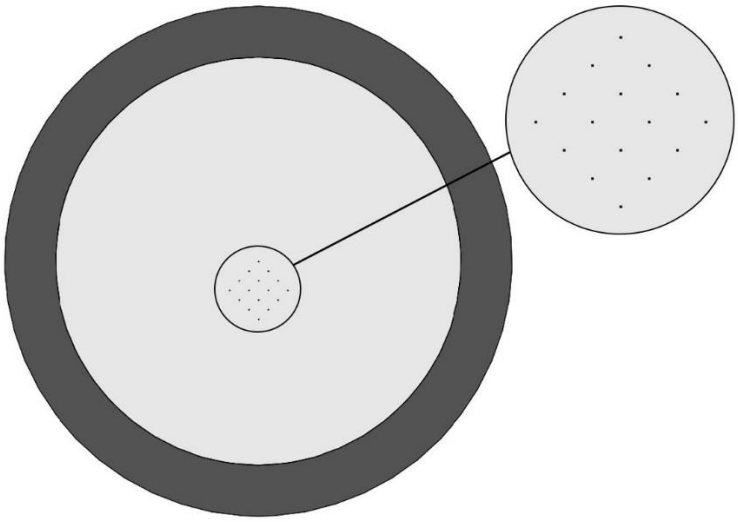

Figure 3.16: Vickers micro hardness test pattern on mounted thermal sample (3mm x 3mm)

After the indentations were completed, a microscope was used to measure and calculate the Vickers hardness value (HV) following Equation 3.3 [126] below:

$$HV = \frac{1.8544P}{d^2} \quad \textbf{3.3}$$

The hardness values were measured automatically using the Wilson VH software. All results were exported to Microsoft Excel for further analysis.

3.5.1.2 TENSILE

Tensile tests were performed using the principles outlined in ASTM standard B557M-15 [127], using an Instron 3385H tensile machine located at UBCO.

Pin-loaded tensile test specimens were fabricated using a lathe. The specimens were cut from the mechanical mold castings in such a way that a minimum of two Ø4 mm gauge samples were extracted. Figure 3.17 shows the specimen dimensions and Figure 3.18 shows how each sample was cut from the mechanical mold castings.

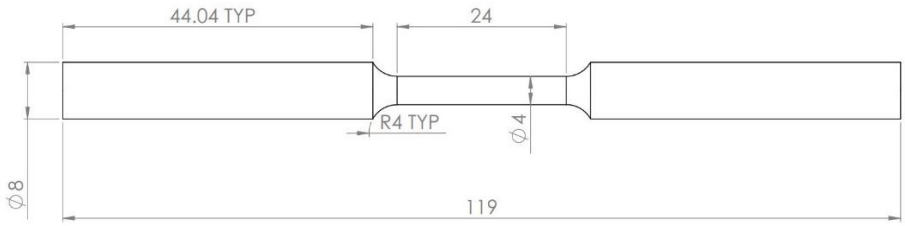

Figure 3.17: Tensile test specimen drawings (all units in mm)

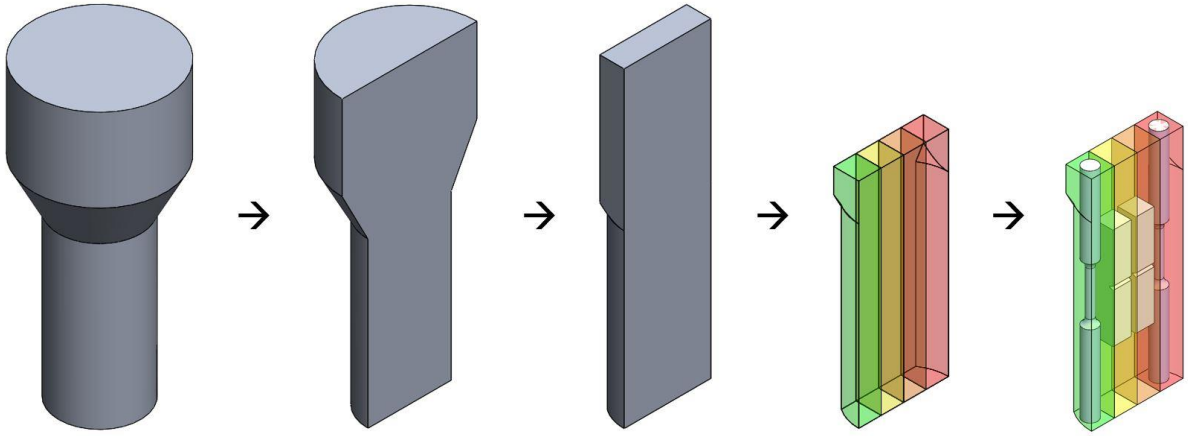

Figure 3.18: Tensile and Charpy specimen extraction from mechanical mold casting

Using PARTNER software on the Instron computer, a standard ASTM tensile test [127] was programmed. The sample was first loaded into the Instron's pneumatic jaws before applying a preload of 25N at 1mm/min. The program was then initiated and a constant strain rate of 0.2mm/min acted until specimen failure.

Two tensile tests were performed for every mechanical mold casting; therefore, a total of four tensile tests were performed for each experimental alloy. If visible inclusions or considerable porosity were seen on the fracture surface, a new tensile sample was fabricated, and a retest was carried out.

The stress and strain data collected by the PARTNER software during the test was exported to Microsoft Excel and the ultimate tensile strength (UTS, in MPa), elongation (%), reduction of area (%), and stress/strain curves were calculated.

3.5.1.3 CHARPY

Charpy tests were performed using the principles outlined in ASTM standard E23-16b [128], using a Tinius Olsen impact test pendulum (P/N: 224285).

Standard simple-beam V-notch Charpy test specimens were manufactured at the UBCO machine shop using a milling machine. These specimens were cut from the mechanical mold castings in such a way that a minimum of two standard ASTM samples could be retrieved. Figure 3.19 below shows the specimen dimensions.

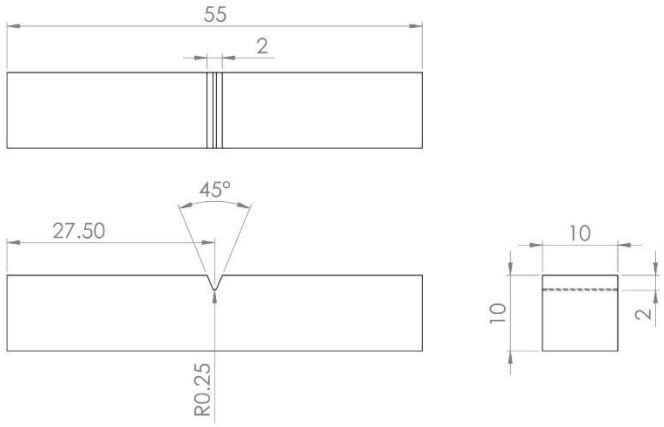

Figure 3.19: Charpy test specimen drawings (dimesnions in mm)

Each Charpy sample was loaded into the Tinius Olsen's sample stage. After a sample was securely positioned into the anvil, the pendulum was released, and the impact force was recorded in ft*lbs.

3.5.2 MICROSTRUCTURE ANALYSIS AND MATERIAL CHARACTERIZATION

Microstructure analysis was performed on all the master alloys and cast samples prepared in this work. The following sections outline the procedures and testing performed on the master alloys and cast samples.

3.5.2.1 SAMPLE PREPARATION

Mounting and polishing

For viewing with the optical microscope and SEM, samples were carefully extracted from SPS pellets and bulk castings using a fine-tooth band saw. Once sectioned, the samples were mounted in Multifast phenolic hot set resin (P/N: 40100028) using a Struers Cito-Press-1 and following the outlined manufacturers procedure.

The mounted samples were then polished to a mirror finish, following the schedule outlined in Table 3.7 below.

Table 3.7: Sample polishing schedule

Step	MetLab Polishing Consumables	Force (N)	~Time (sec)
1	P240	hand	45
2	P400	hand	45
3	P600	hand	45
4	P800	hand	45
5	9 µm diamond paste and suspension w/ designated pad	240	180
6	6 µm diamond paste and suspension w/ designated pad	210	180
7	1 µm diamond paste and suspension w/ designated pad	150	180
8	0.5 µm OP-S solution w/ designated pad	90	60

The sample were rinsed thoroughly with denatured alcohol between each step to prevent particle contamination in the polishing process.

Etching

Samples were etched to reveal the grain boundaries to enable grain size measurements. Etching was done at the UBCO chemistry lab using the reagent and particulars listed in Table 3.8 below.

Table 3.8: Sample etchant and etching time

Etchant	Chemical composition	Sample immersion time (sec)
Keller's Reagent	– 175mL distilled water – 5mL nitric acid (HNO_3) – 2mL hydrofluoric acid (HF) – 3mL hydrochloric acid (HCl)	20

A sample was fully submerged into Keller's reagent for 20 seconds. Immediately afterwards, the sample was submerged into two consecutive baths of distilled water to rinse off the acid etchant. The sample was then rinsed with denatured alcohol and put under a heated air dryer to remove any water marks before grain size measurement.

3.5.2.2 MASTER ALLOY ANALYSIS

The density and carbon distribution in the as-sintered master alloys was examined using Archimedes principle and by SEM-EDXS techniques.

The Archimedes test was performed on each master alloy after sintering to check if adequate sample densification was achieved. The Archimedes test procedure measures the specific gravity of a sample in water; therefore, since specific gravity is the ratio of a substance's density over the test liquid's density, and since the density of water is very close to 1.0 g/cm^3 (0.9982 g/cm^3 at 20°C), the specific gravity can be taken as an accurate measurement of the sample density.

The following procedure was followed for all Archimedes tests:

1. The mass of the master alloy was found (scale accuracy ±0.005 g).
2. Using an Archimedes test kit, the sample's mass in distilled water was measured (scale accuracy ±0.005 g).
3. The master alloy's specific gravity was calculated following Equation 3.4 below:

$$SG = \frac{W_{air}}{W_{air} - W_{water}} \quad \textbf{3.4}$$

Where: *SG* = specific gravity

W_{air} = sample mass in air

W_{water} = sample apparent immersed mass in distilled water.

3.5.2.3 NEWTONIAN THERMAL ANALYSIS

Using Microsoft Excel, Matlab, and Origin graphing software, data collected from the thermal mold castings was used to produce the solidification curve (T/t), the solidification rate curve (dT/dt), baseline rate curve (dT/dt BL), and the fraction of solid curve for each alloy.

The baseline rate curve equation was calculated using Matlab's logarithmic line-fitting add-in, and was used for an estimation of the theoretical cooling curve [129]. Points were chosen at the beginning of each alloy's dT/dt curve before solidification begins, above ~650°C, and after solidification ends, below ~520°C. The Matlab software would then plot a logarithmic equation with coefficients of 95% confidence bounds and a typical R-square value of 0.99.

The fraction of solid curve was produced by plotting the instantaneous fraction solid (f_s) over time (s) during the solidification of an alloy. The instantaneous fraction solid was found using Equation 3.5 [130], [131].

$$f_s = \frac{T_L - T + \frac{2}{\pi}(T_S - T_L)\{1 - cos\left[\frac{\pi(T - T_L)}{2(T_S - T_L)}\right]\}}{(T_L - T_S)[1 - \frac{2}{\pi}]} \quad \textbf{3.5}$$

Where: T_L = non-equilibrium liquidus temperature

T_S = non-equilibrium solidus temperature

T = instantaneous alloy temperature.

The above equation calculates the fraction solid percentage based on the alloy's assumed constant liquidus and solidus temperatures. Yet, for alloy systems with high cooling rates the concentration of solute at the solid-liquid interface changes throughout solidification, thus the liquidus and solidus temperatures are changing also. However, while acting on the assumption of constant liquidus and solidus temperatures, the validity of this equation has been empirically tested and shown excellent correlation [132]–[134].

Figure 3.20 shows an example of the thermal analysis graphs for the virgin B319 alloy. Important thermal points are identified by the numbered markers, and dashed lines show how these points correspond to the axes or other plots. Table 3.9 is also given and describes referenced solidification points in respects to Figure 3.20.

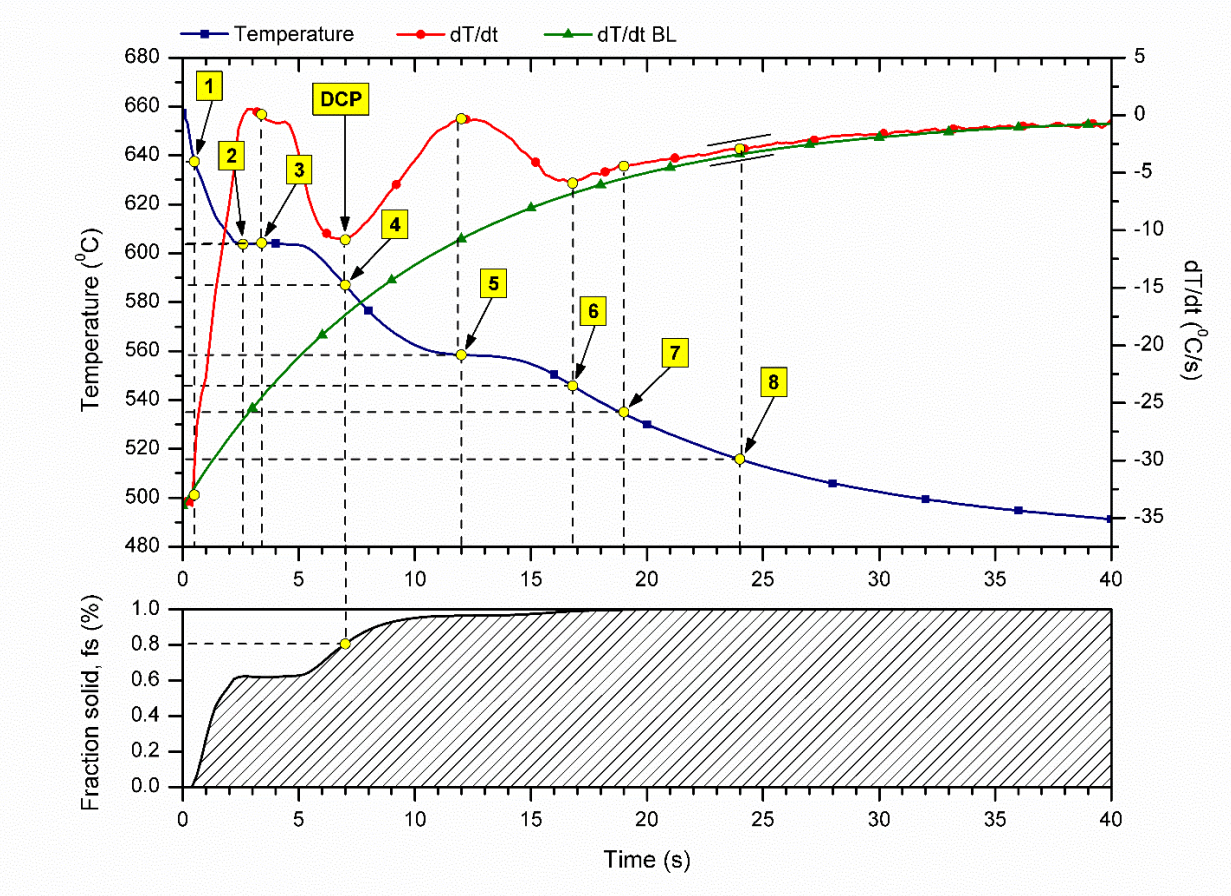

Figure 3.20: Illustration of solidification characteristics on the virgin B319 alloy's cooling curves. Denoted points are explained or related to solidification in Table 3.9 (DCP = dendritic coherency point)

Table 3.9: Solidification characteristics of the B319 alloy (in relation to Figure 3.20)

Thermal data	Description	Relation to Figure 3.20
$T_{N\ \alpha\text{-Al}}$	α-Al nucleation temperature, [°C]	pt. 1 (~ dT/dt leaves dT/dt BL)
$T_{G\ \alpha\text{-Al}}$	α-Al growth temperature, [°C]	pt. 3 (~ avg. peak of dT/dt)
T_{UC}	underccoling temperature, [°C]	pt. 3 – pt. 2
$t_{G\ \alpha\text{-Al}}$	α-Al growth period, [s]	pt. 4 – pt. 1
$T_{N\ Al\text{-}Si}$	Al-Si eutectic nucleation temperature, [°C]	pt. 4
$T_{G\ Al\text{-}Si}$	Al-Si eutectic growth temperature, [°C]	pt. 5 (~ avg. peak of dT/dt)
$t_{G\ Al\text{-}Si}$	Al-Si eutectic growth period, [s]	pt.6 – pt.4
$T_{N\ Al\text{-}Cu}$	Al-Cu intermetallic nucleation temperature, [°C]	pt. 6
$T_{G\ Al\text{-}Cu}$	Al-Cu intermetallic growth temperature, [°C]	pt. 7 (~ avg. peak of dT/dt)
FR	freezing range, [°C]	pt. 1 – pt. 8 (pt.8 ~ dT/dt and dT/dt BL parallel)
t_s	solidification time, [s]	pt. 8 – pt. 1
CR	cooling rate, [°C/s]	FR / t_s
T_{DCP}	temperature at the dendrite coherency point, [°C]	pt. 4 (~ dT/dt valley)
$fs_{,DCP}$	fraction of solid at the dendrite coherency point [%]	pt. 4 fs %

3.5.2.4 FLUIDITY ANALYSIS

To evaluate the effect of carbon black additions on the B319 alloy's fluidity, the flow length of the liquid metal along the spiral mold was measured. The castings were placed onto a polar graph paper and imaged with a DSLR camera (as seen in Figure 3.21) to measure the flow distance.

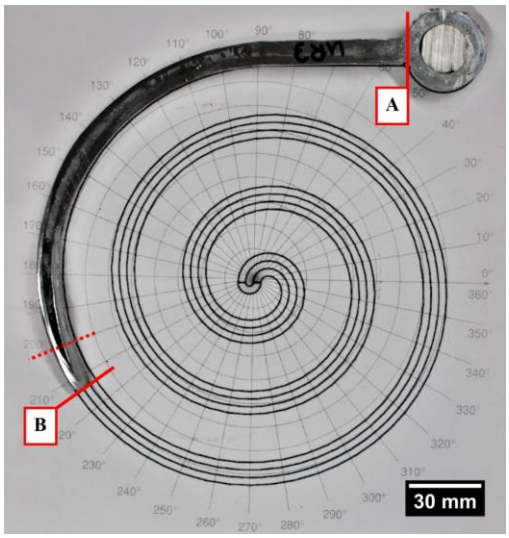

Figure 3.21: Fluidity analysis of the virgin B319 alloy; (a) start of measurement, (b) end of measurement

The image was then analyzed with ImageJ software and the specimen's length, measured from *A* to *B* in Figure 3.21, was calculated.

3.5.2.5 GRAIN SIZE EVALUATION

Grain size measurement was conducted on samples from the thermal mold castings. A 6.35mm disk was cut from thermal mold castings as shown in Figure 3.22.

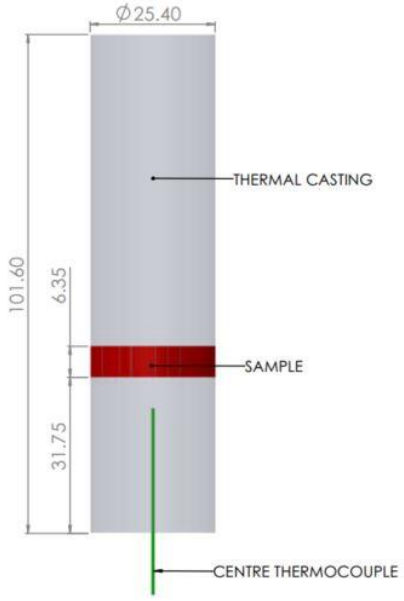

Figure 3.22: Grain size evaluation specimen extraction from thermal mold castings (all units in mm)

This disk was cut 31.75mm from the base of the sample to be close to the thermocouple, yet far enough away from the thermocouple that it would not provide a nucleation site and cause distortion of grain size measurements. The samples were then polished, mounted, and etched on the side closest to the thermocouple, following the procedure outlined in Section 3.5.2.1.

The grain structure of the samples was evaluated using ImageJ software and Abrams three-circle intercept procedure, measured according to the principles outlined in ASTM standard E112-13 [135].

Three circles, centered on the specimen, were drawn: Ø17.88mm, Ø12.82mm, and Ø7.76mm. Intercepts were then counted at any point where a circle crossed a grain boundary, as seen in Figure 3.23 below (intercepts are marked with cross hairs along the circles).

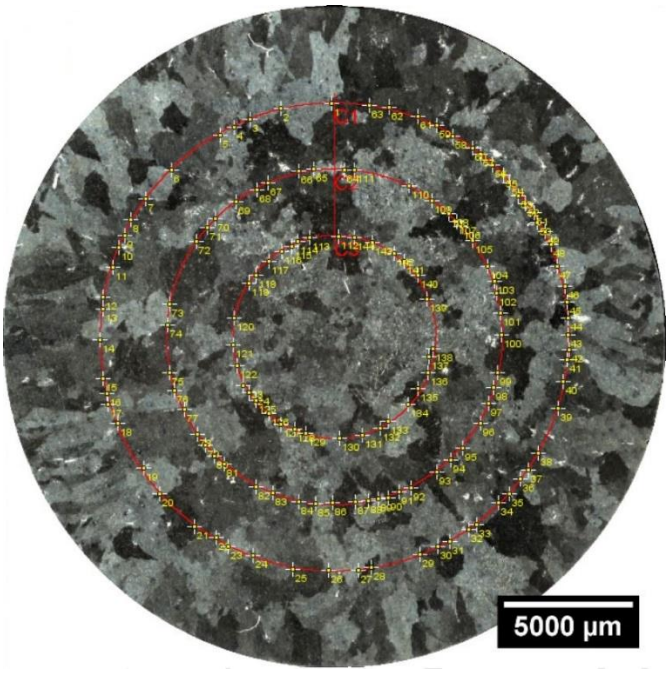

Figure 3.23: Abrams three-circle grain size measurement of the virgin B319 alloy

Average grain size was calculated using Equation 3.6 [135]:

$$GS = \frac{\pi(D_1 + D_2 + D_3)}{N_i} \quad \textbf{3.6}$$

Where: GS = average grain size

D_1 = diameter of circle 1

D_2 = diameter of circle 2

D_3 = diameter of circle 3

N_i = total intercepts

3.5.2.6 MICROSCOPY AND SCANNING ELECTRON MICROSCOPY

Optical microscopy was performed at UBCO using a Ziess AxioVert A1m microscope. The Ziess microscope was connected to a desktop computer with a Buehler Omnimet 9.5 image analysis software.

SEM and EDXS analysis was performed at the UBCO SEM lab using a Tescan Mira3 XMU field emission scanning electron microscope. Images were captured using Tescan software, while EDXS and elemental analysis was obtained using Oxford Aztec X-MAX EDXS software and an 80 mm^2 EDXS detector.

Before SEM and EDXS analysis, mounted and polished samples were sputter coated with 10 nm of platinum-palladium. To ensure the best image quality (reduced surface oxidation), the final sample polish was performed just prior to sputter coating and SEM analysis.

3.5.2.7 X-RAY DIFFRACTION

XRD analysis was performed on samples to complement the elemental EDXS analysis to identify the alloy phases. All XRD used in this work was conducted at the University of British Columbia Vancouver campus (UBCV) using a Bruker D8 Advance X-ray diffractometer. XRD characterization was performed from 0°-90°, using a step size of 0.03°, a step time of 145.6s, and with Cu-Kα radiation (40kV, 40mA).

CHAPTER 4: RESULTS AND DISCUSSION

This chapter provides the results obtained for casting experiments and alloy characterization of carbon inoculation trials on the B319 alloy.

4.1 PRECURSOR EXPERIMENTS

The precursor experiments of this thesis were performed to determine three primary objectives:

1. The most efficient method for homogenously mixing aluminum and carbon black powder before sintering (powder preparation).
2. The highest allowable weight percentage of carbon black in aluminum that would yield a stable and adequately dense solid after sintering (master alloy synthesis).
3. The most effective total weight percentage carbon black in a casting for grain refinement (cast alloy refinement).

4.1.1 POWDER PREPARATION TRIALS

Due to a large density difference and some static charging, carbon black powder was not easily mixed with aluminum powder. Carbon black powder has a range of bulk density of 0.17-0.23 g/cm^3, which is and order of magnitude lower then the density of pure aluminum powder (2.7 g/cm^3) [7]. To create a fully homogenous sintered alloy, spark plasma sintering requires that the loaded powder blend be completely homogenous. To achieve this, two blending procedures were tried:

1. Ball mill blending
2. Stir blending

Ball mill blending was first attempted due to the reported success of milled carbon nano-tubes (which have a similar size and powder likeness to amorphous carbon black) and aluminum powder in literature [120], [136], [137]. Using a planetary ball mill and a variety of milling parameters, suspension fluids, and packing ratios; it was found that high energy operations consistently produced some variety of Al-C oxide/hydroxide within the powder. XRD was performed and it was thought that Boehmite, or aluminum oxide hydroxide (AlO[OH]), was the milled by-product. Milling in an inert atmosphere (such as argon) was not attempted due to machinery constraints, which may have mitigated the production of oxides/hydroxides [120],

[136], [137]. Alternatively, powder produced by low energy milling operations was seen to readily separate back to into partitioned aluminum and carbon black powders once dried and physically agitated (this was seen even with the visible deformation of aluminum particles in the milling process).

Stir blending was then attempted as the least intensive method available. Aluminum and carbon black powders were added to a beaker and mixed by stir stick, either dry or with varying amounts of suspension fluid (water, alcohol, and dimethylformamide (DMF) [138]–[141]). It was found that a homogenous powder blend, and subsequent sintered solid, was best formed if the powder mixture was stirred as a slurry in alcohol. Once mixed and achieving a wet sand like consistency, the mixture was immediately loaded into the SPS die and dried in an oven before sintering (referred to Section 3.3.2 of the experimental procedure).

4.1.2 MASTER ALLOY SYNTHESIS TRIALS

To find the approximate highest allowable weight percentage of carbon black in aluminum for solid stability after sintering, three Al-C powder blends were tested:

1. 10wt% carbon black in aluminum
2. 5wt% carbon black in aluminum
3. 2wt% carbon black in aluminum

High purity carbon black, C_A, was used for each pellet trial. Figure 4.1 below shows each pellet after sintering (either full or sectioned).

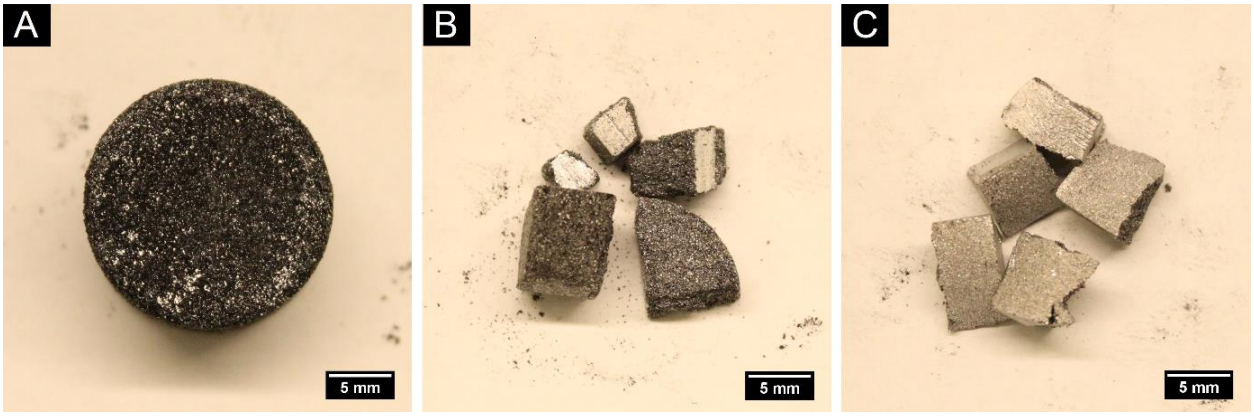

Figure 4.1: Master alloy synthesis trials; (a) 10wt% C pellet, (b) 5wt% C sectioned pellet, and (c) 2wt% C sectioned pellet

It was found that the 2wt% pellet was most solid and was then selected as the high concentration master alloy. The 10wt% and 5wt% pellets were seen to more readily break apart under pressure and have large carbon agglomerations easily visible to the naked eye.

4.1.3 CAST ALLOY REFINEMENT TRIALS

Research by Kumar and Bichler [77] found that the most effect total weight percentage of a carbon containing inoculant (TiC) for grain refinement of the B319 alloy was 0.03wt%. To test these findings with a pure carbon master alloy, three thermal mold castings were performed (see section 3.4.3 of the experimental procedure):

1. 0.10wt% total carbon added to the B319 alloy
2. 0.03wt% total carbon added to the B319 alloy
3. 0.01wt% total carbon added to the B319 alloy

Each of these casting used the AH master alloy, synthesised with 2wt% C_A.

After the preliminary castings, each sample was sectioned, etched, and imaged following Section 3.5.2 of the experimental procedure. 0.03wt% added C was seen to yield the smallest grain size and was selected as the total carbon content to be used for further grain refinement research and was in agreement with previous research [77].

Figure 4.2 below shows the average grain size for each composition.

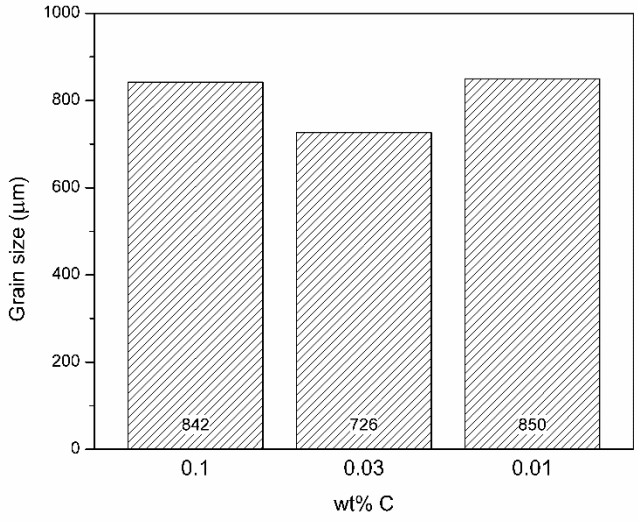

Figure 4.2: Cast alloy refinement trials. Average grain size of single casting samples with 0.10, 0.03, and 0.01 total wt% C

4.2 CHARACTERIZATION OF PRE-CAST MATERIALS

The following section characterizes the properties, microstructure, and chemical compositions of pre-cast materials; which include the raw powders and following master alloys synthesized from those powders.

4.2.1 RAW POWDERS

Pure aluminum and two grades of carbon black, high purity (C_A) and recycled (C_R), were used for the synthesis of master alloys. The three powders were characterized in terms of particle size, composition, and morphology.

4.2.1.1 PARTICLE SIZE

The average particle size for each powder can be seen in Table 4.1.

Table 4.1: Raw powder particle sizes

Powder	Average particle size
Aluminum, Al	50 µm
Carbon black A, C_A	183 nm
Carbon black R, C_R	307 nm

The larger and more dense aluminum powder was measured from SEM images using a particle analyzer through ImageJ software, whereas the carbon black powders were small enough to be suspended in a DMF solution and measured by laser diffraction. High purity C_A was found to have a finer average particle size compared to the recycled carbon black. Figure 4.3 shows an example of the laser diffraction results seen from a measured sample of 0.75vol% C_R in DMF. Two peaks can be seen corresponding to particle distributions around 9 nm (low intensity, ~12.9%) and 345 nm (high intensity, ~87.1%). The smaller peak likely represents individual nodules, or small clusters, while the larger peak represents aggregate agglomerates of carbon black [110]. Therefore, the recycled carbon black appears to agglomerate in larger stable clusters than the high purity carbon black and is considered coarser. Figure 4.4 shows the laser diffraction results for a sample of C_A for comparison, which shows a finer particle size.

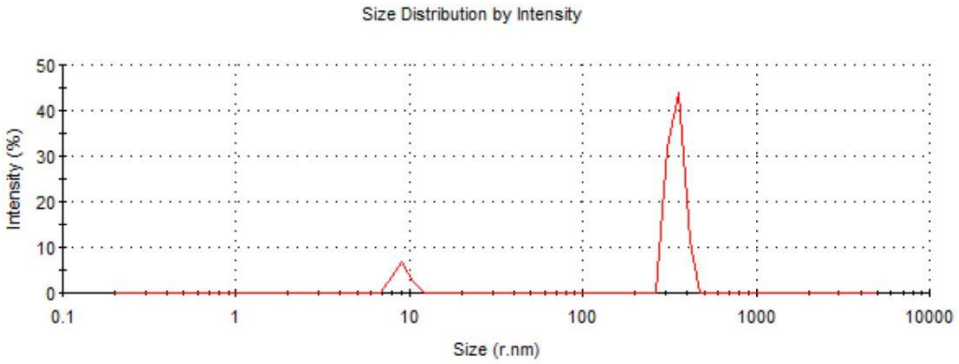

Figure 4.3: Laser diffraction results for C_R suspended in DMF solution (0.75vol%)

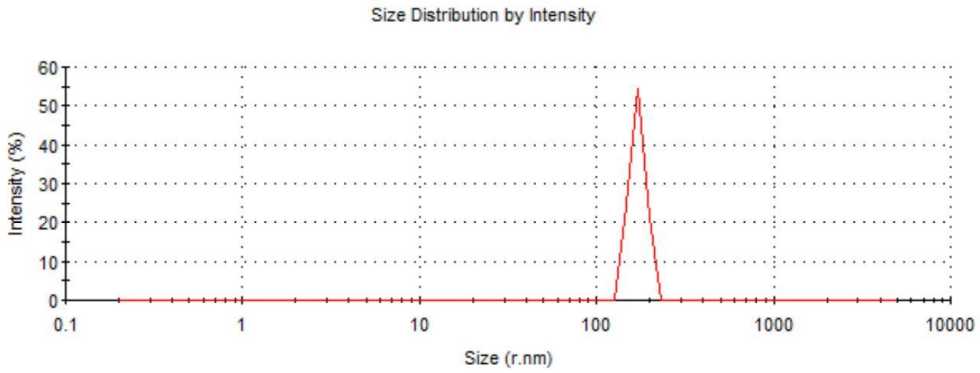

Figure 4.4: Laser diffraction results for C_A suspended in DMF solution (0.75vol%)

4.2.1.2 RAW POWDER X-RAY DIFFRACTION

Each powder was analyzed by XRD, the results of which can be seen in Figure 4.5 below.

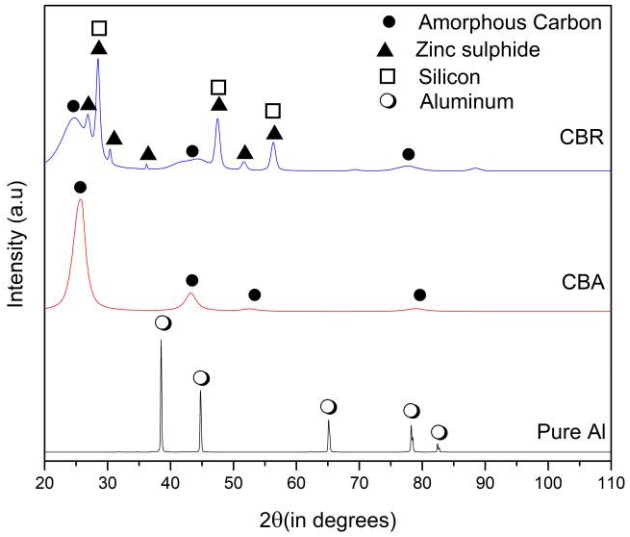

Figure 4.5: XRD spectra of raw powders; aluminum, high purity carbon black (C_A or CBA), and recycled carbon black (C_R or CBR)

Both the aluminum and C_A powder showed only peaks representative of their pure constituents, while C_R showed additional peaks for zinc sulphide and silicon contaminants. These contaminants are likely impurities resulting from the recycling process.

The diffractograms from the figure above show the C_R had more broad peaks compared to C_A. This would suggest that the recycled carbon black contained a greater amount of amorphous carbon structure compared to the high purity carbon, since broad peak distribution in the 2θ range is indicative of an amorphous material [142]. The C_A sample likely then contained a higher percentage of carbon crystallinity. However, it can still be seen that the peak distribution for C_A is broader than a full crystalline phase such as silicon; therefore C_A can still be considered as a largely amorphous material.

4.2.1.3 MICROSCOPY AND CHEMICAL ANALYSIS

Microscopy and chemical analysis was performed on the powders via SEM/EDXS. Figure 4.6 and Figure 4.7 show the morphology of the pure aluminum powder and the two carbon black powders, respectively.

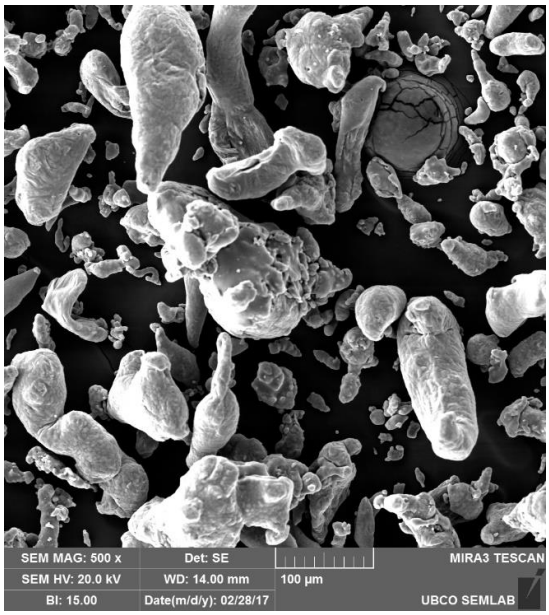

Figure 4.6: SEM image of aluminum powder used

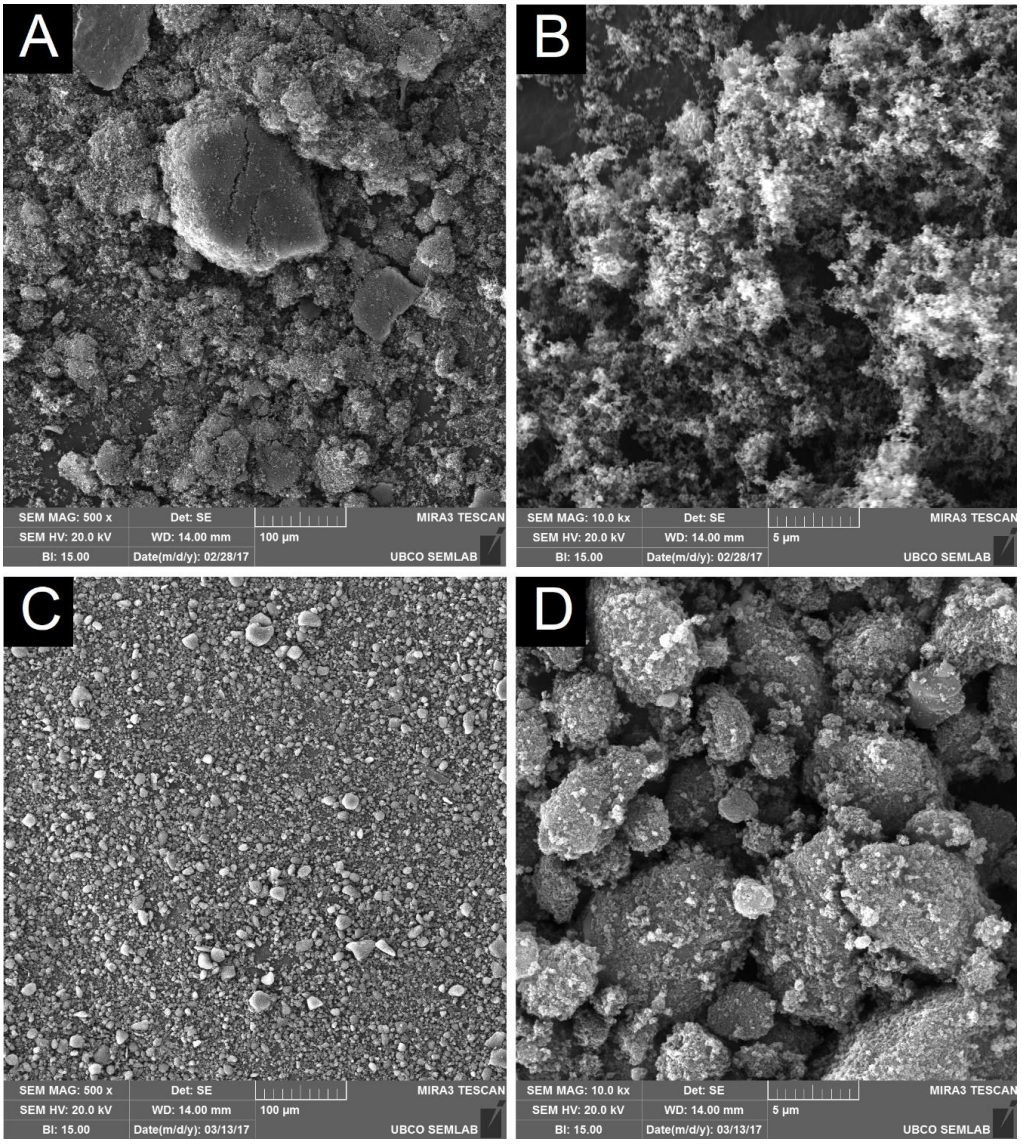

Figure 4.7: SEM micrographs of carbon black powders; (a) C_A at 500x, (b) C_A at 10kx, (c) C_R at 500x, and (d) C_R at 10kx

While it may appear at 500x magnification that C_A has a larger particle size than C_R, at 10kx magnification it becomes apparent that C_A has a much finer particle structure of agglomerated carbon particles, where as C_R still exhibits clumped carbon black aggregate at the same magnification.

EDXS analysis was performed on each of these powders to check chemical compositions. The results of the chemical analysis are tabulated below.

Table 4.2: Chemical composition of aluminum and carbon black raw powders

Elements (wt%)	Ag	Al	C	Ca	Fe	Mg	Na	S	Si	Zn
Aluminum	0.76	balance	-	-	-	-	-	-	-	-
High purity, C_A	-	-	100	-	-	-	-	-	-	-
Recycled, C_R	-	-	92.17	0.15	0.12	0.13	0.44	2.20	1.16	3.63

The results above have some limitations in regards to C detection, based on the difficulties associated with the measurement of light elements such as H, O, or C by SEM/EDXS [143], [144]. Therefore, EDXS results in relation to these light elements is semi-quantitative in nature, since accurate quantitive detection is not feasible via EDXS for this scenario.

The chemical analysis of the recycled carbon black verifies the XRD results, which showed zinc sulfide (ZnS) and silicon as impurities. Considering proper stoichiometric ratios, zinc was approximately twice the weight percentage of sulfur. However, the less prevalent impurities found by EDXS in the carbon powders (Ca, Fe, Mg, Na) did not show up in the XRD analysis. This is most likely due to the small percentages (<0.5wt%) contained in the sample, which probably were hidden in the diffractogram noise and thus below the XRD's detection limit for this setup [142].

4.2.2 MASTER ALLOYS

Following past research by Azad and Bichler [121], Davis *et al*. [145], and Davis *et al*. [122]; SPS manufactured grain refiners for this work were used to test the efficacy of carbon black inoculation in the B319 alloy. Both high concentration (2wt% C) and low concentration (1wt% C) master alloys were used to study the effect of varied concentrations. To study the effect of particle size and purity, two groups of master alloys were synthesized; one from fine high purity carbon black (C_A) and one from a coarser and less pure recycled carbon black (C_R). In total four master alloys were synthesized: AH (2wt% C_A), AL (1wt% C_A), RH (2wt% C_R), and RL (1wt% C_R).

The following sections characterize the sintered master alloys used in this thesis.

4.2.2.1 DENSIFICATION

To assess the success of sintering, densification analysis was performed on the post-sintered pellets as described in section 3.5.2.2. A summary of the density results is shown in Figure 4.8.

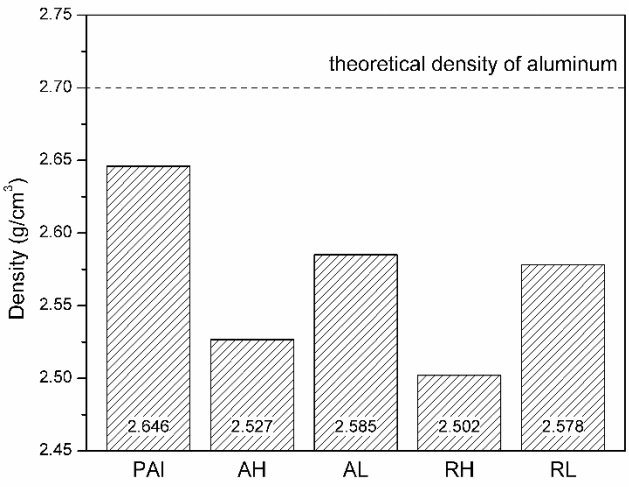

Figure 4.8: Densities of master alloys after SPS processing

Compared against a sintered sample of pure aluminum (PAl) the master alloys were found to be 4.7%, 5.8%, 2.4%, and 2.6% less dense for AH, RH, AL, and RL, respectively. It was anticipated that the low concentration master alloys would yield the highest degree of densification, due to less total carbon black. The above figure shows that in general, master alloys synthesized with C_A carbon achieved better densification. Presumably, the finer particle size of C_A allowed for better dispersion and coating of aluminum particles in the powder mixing, which was locked in during sintering. Figure 4.9 shows optical micrographs of each sintered sample and verifies that there was better qualitative carbon dispersion in low concentration pellets, and better relative densification in C_A pellets (AH and AL) versus the C_R pellets (RH and RL).

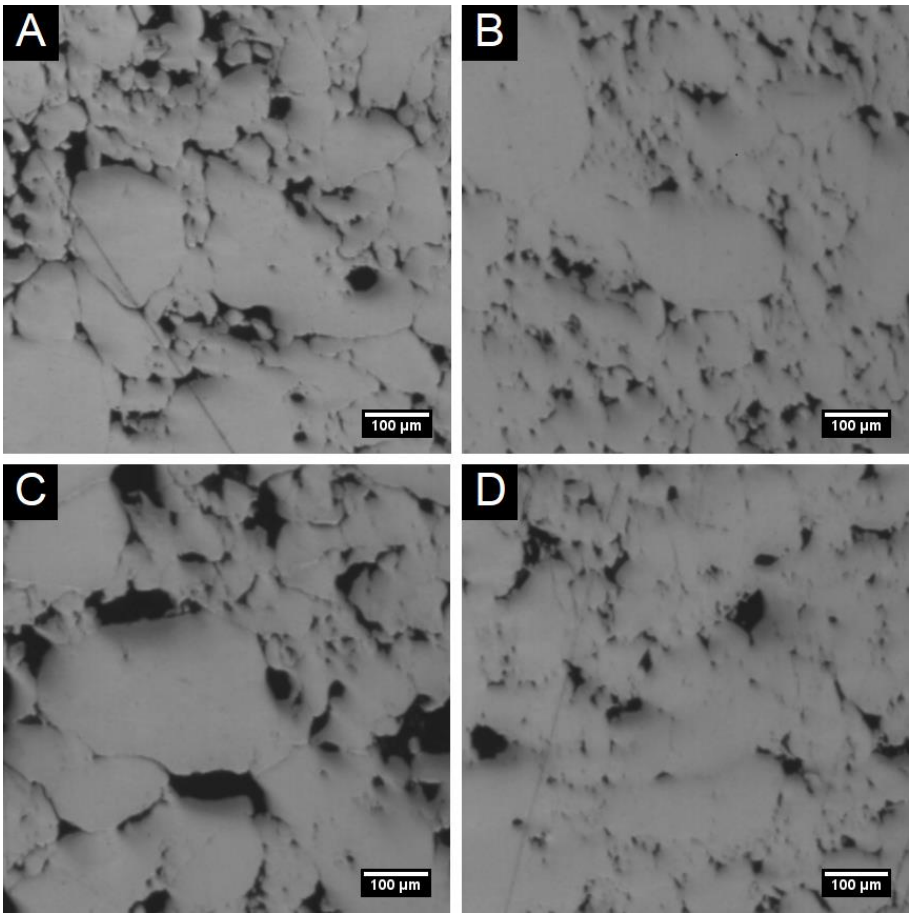

Figure 4.9: Optical micrographs of master alloys after SPS processing; (a) AH, (b) AL, (c) RH, and (d) RL

4.2.2.2 MASTER ALLOY X-RAY DIFFRACTION

X-ray diffraction was done on a portion of each master alloy after sintering, shown in Figure 4.10.

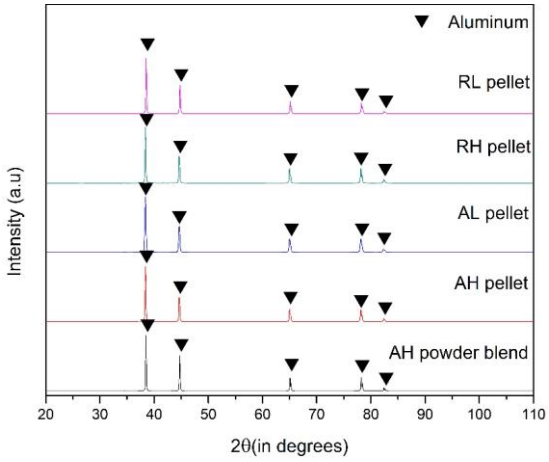

Figure 4.10: XRD spectra of master alloys

Comparing to Figure 4.5 (XRD of the raw carbon black powders), peaks at approximately 77.5°, 52.5°, 44°, or 26° would indicate carbon presence [146], [147]. While these carbon peaks were not immediately visible, at a much closer inspection a slight peak was found near 26° for the AH and RH master alloys (seen in figure below). However, no other carbon peaks were seen due to the low overall carbon presence, which can be hidden by XRD noise at low compositional percentages (<0.5wt%) for the XRD setup used.

A pre-sintered sample of the AH powder blend was also sent for XRD and showed no difference of result, indicating that the sintering process did not create any new phases discernable within the equipment's detection limits.

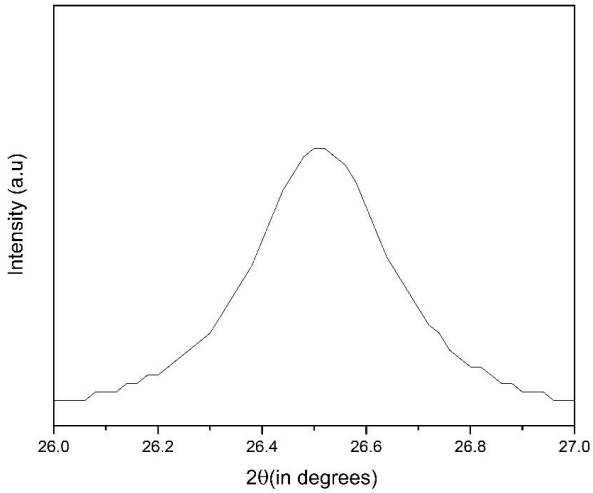

Figure 4.11: Partial XRD spectra of the RH master alloy; 26.0°-27.0°

4.2.2.3 MICROSCOPY AND CHEMICAL ANALYSIS

After sintering, SEM and EDXS analysis was performed on the master alloys to evaluate the post-sintered structure and constituents. Figure 4.12 shows a map scan of the KH master alloy, which closely resembled the carbon dispersion and structure of all other master alloys.

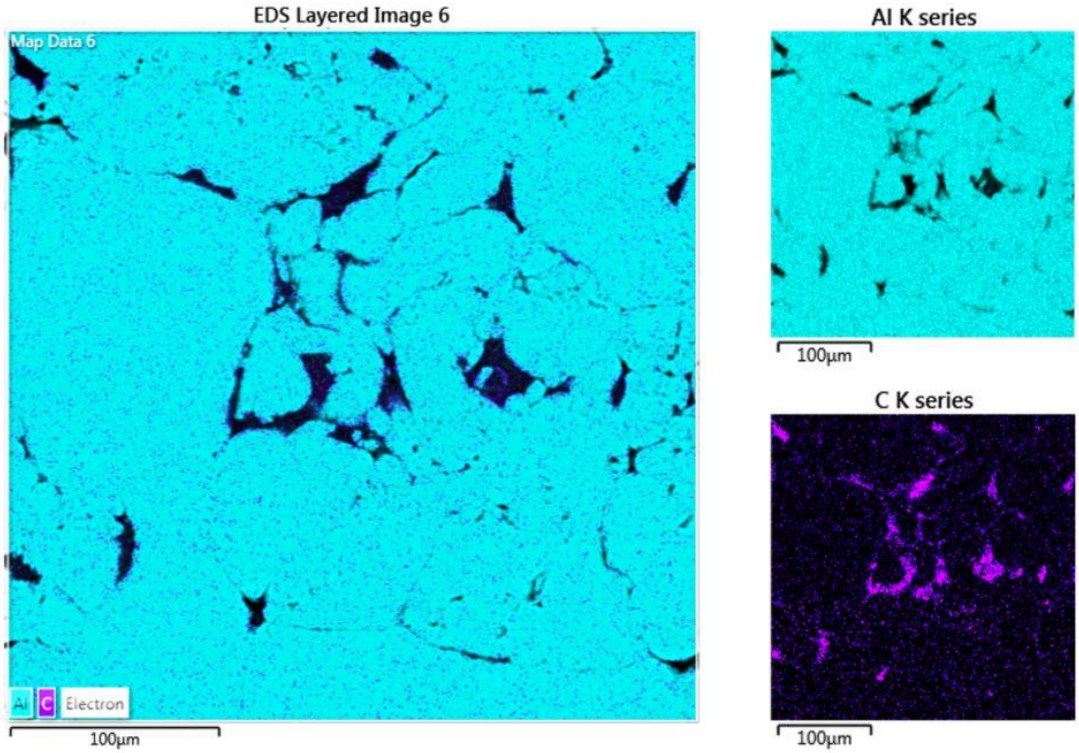

Figure 4.12: EDXS map scan of the KH master alloy

It can be seen from Figure 4.12 that the added carbon black was present and isolated to the grain boundaries of the sintered master alloy sample. This was seen uniformly over the cross section of the master alloy, verifying carbon presence and dispersion in the synthesized master alloys.

As discussed in Section 2.5, the SPS process is often favourable for the sintering of reactive or oxidizing materials, since it can be done in a tightly controlled atmosphere and at closely monitored temperature ranges. However, it is known that the joule heating principle for conductive powders (such as aluminum or carbon) can allow for localized grain boundary temperatures far exceeding that of the set sintering temperature [148]–[151]. Therefore, EDXS line scans were performed on each of the master alloys samples, investigating the grain boundary regions and Al-C interfaces for the potential formation of auxiliary phases during the SPS process. Figure 4.13 is a line scan from the AH master alloy, which shows a strong diffusion layer of carbon into the Al matrix. Areas of this diffusion layer could be seen as a visibly darker outline around the Al grains. The darker diffusion regions were measured up to 1 µm thick as seen in Figure 4.13, but most often was found to be a few hundred nano-metres thick.

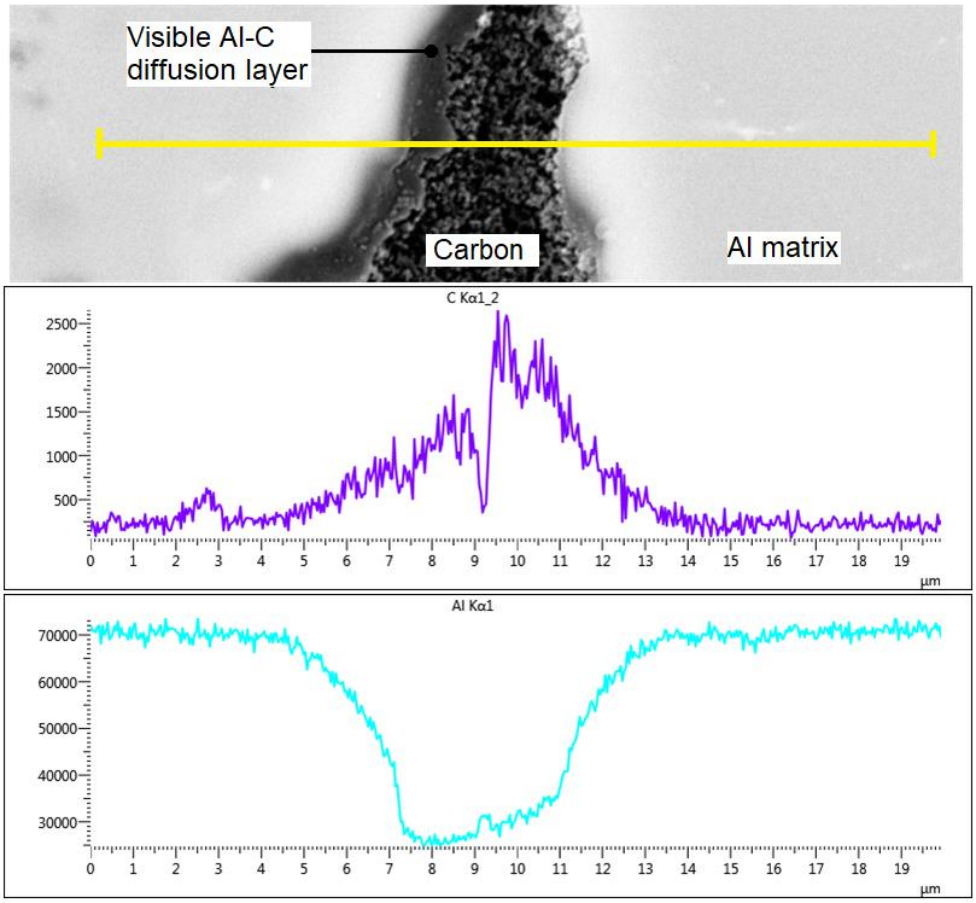

Figure 4.13: EDX line scan of the AH master alloy

Although undetectable by XRD and considering the limitations of measuring light elements with SEM/EDXS, it is suspected that these regions of carbon diffusion represent the formation of a thin layer of aluminum carbide (Al_4C_3) over the Al grains. This was found by Lalet *et al*. [152] who sintered aluminum and carbon fiber via SPS and discovered a similar layer at the Al-C interfaces. This thin formation of Al_4C_3 was also seen by Yang and Scott [106] when carbon fibre preforms were infiltrated with a molten Al-Si-Mg alloy and subsequently analyzed by EDXS. Yang and Scott however, found Al_4C_3 crystals of only ~20nm thick at the boundary; and used molten Al temperatures of over 700°C versus the relatively lower SPS temperatures of 470°C used in this research.

It was seen for all master alloy samples, that the Al-C diffusion layer was thicker and more evident at the narrower grain boundaries, near the sites of localized welding between Al particles. This would confirm research by Shon [105] who found that the applied current promoted Al_4C_3 formation at the Al-C interface. With the application of 10-15A across a drop molten Al on a graphite plate, the Al_4C_3 layer was noted to grow from ~30nm to ~90nm. Since

the SPS process can utilize as much as 3000A through a single sample, this high current may explain the relatively thick µm-scale layers of apparent Al_4C_3, principally at the narrower boundaries where higher currents would be found. Further research needs to be conducted on the topic of Al-C SPS to fully understand these mechanisms; particularly on the effects of sintering temperature, time, and current on the diffusion of carbon into aluminum.

4.3 CASTING RESULTS

To test the effect of carbon black inoculants on the B319 alloy, the SPS manufactured master alloys were added to a series of castings. Each of the four master alloy categories were tested against control castings of the virgin B319 alloy. Secondary control castings were then done with the addition of a pure aluminum 'pseudo' master alloy (PAl) to evaluate the possible effects of alloy dilution. The effect of casting temperature on carbon addition was also tested; however, this was performed for only the thermal mold and was done by casting just the AH refiner against the virgin B319 alloy at lower pouring temperatures ("cold casting"). The AH master alloy was chosen for cold casting tests because it initially showed the best grain refinement among the standard master alloy casting experiments (discussed in Section 4.3.2).

This section discusses the alloy characterization and casting results for the thermal mold and fluidity mold experiments.

4.3.1 THERMAL ANALYSIS

Following the process outlined in Section 3.4, castings were performed using the thermal mold and an in-situ thermocouple, which captured the solidification profile during each experiment.

4.3.1.1 VIRGIN B319 ALLOY THERMAL ANALYSIS

Figure 4.14 shows the captured cooling curve, first derivative cooling curve, first derivative baseline curve, and fraction solid curve for the virgin B319 alloy.

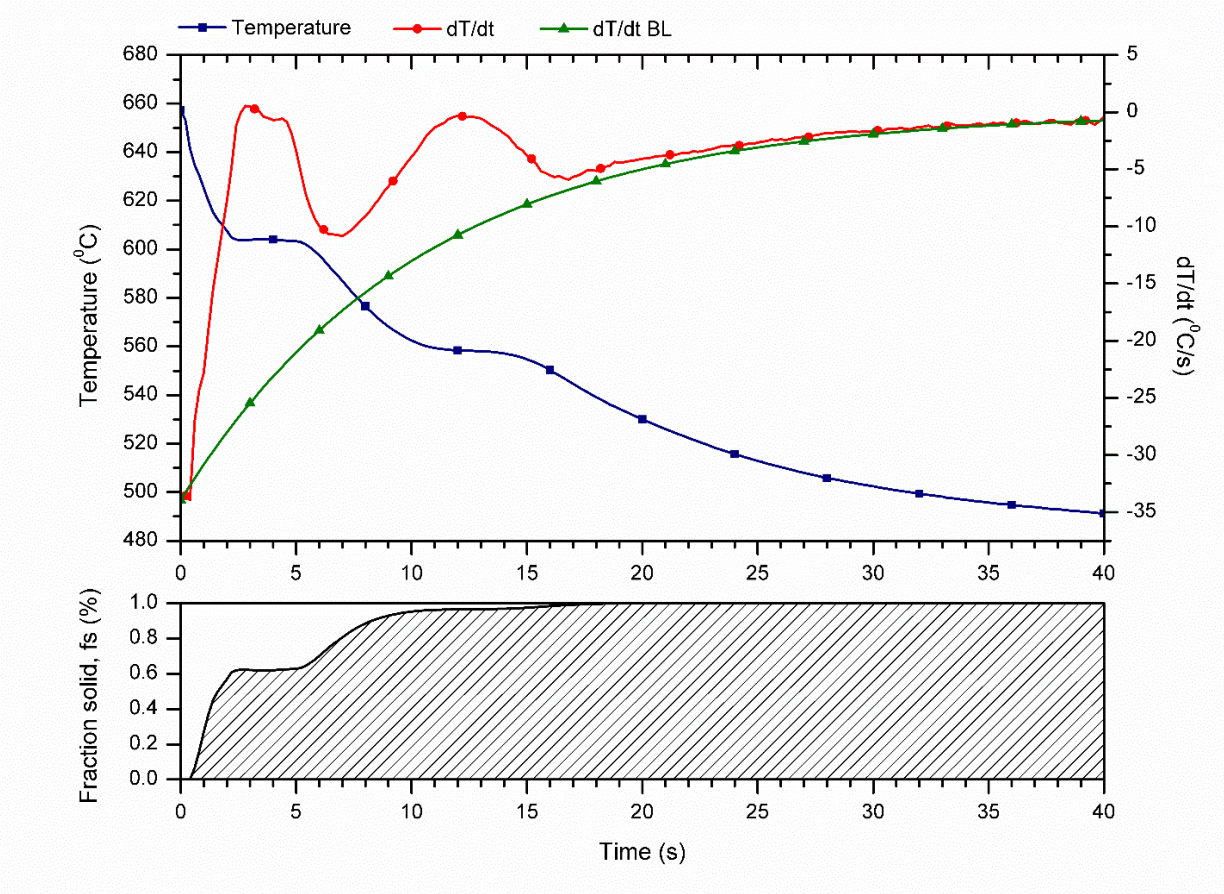

Figure 4.14: Cooling curves for the virgin B319 alloy

Table 4.3 below shows important thermal data recorded from solidification of the virgin B319 control castings (refer to Figure 3.20 on page 59 for an outline of the thermal data points).

Table 4.3: Thermal data for virgin B319 alloy

	Thermal data							
Alloy	$T_{N\ \alpha\text{-Al}}$ (°C)	$T_{G\ \alpha\text{-Al}}$ (°C)	$T_{N\ Al\text{-}Si}$ (°C)	$T_{G\ Al\text{-}Si}$ (°C)	$T_{N\ Al\text{-}Cu}$ (°C)	$T_{G\ Al\text{-}Cu}$ (°C)	T_{DCP} (°C)	$f_{s,\ DCP}$
B319	634	604	589	559	547	533	589	0.76

It can be seen in Figure 4.14, that solidification began with the nucleation of α-Al dendrites at 634°C – found at the point where the first derivative cooling curve (dT/dt) crosses above the baseline cooling curve (dT/dt BL), marking initial recalescence and a sharp cooling rate decrease. The melt then reached the stable growth temperature of the α-Al phase at 604°C, where the majority of dendrite grow proceeded and where mass latent heat release kept the

cooling rate near zero. It should be noted that a small peak on the dT/dt curve can be seen at approximately 4.5 seconds, which literature would suggest marks the precipitation of pre-eutectic iron intermetallics ($L \rightarrow Al + \alpha\text{-}Al_{15}(Fe,Mn)_3Si_2 + \beta\text{-}Al_5FeSi$) [52], [55]. Once the α-Al dendritic network was fully formed, dendrites began to impinge upon each other. This signifies the dendrite coherency point (DCP) at a temperature of 589°C and a fraction solid of approximately 76%. At this same temperature, the Al-Si eutectic reaction began, marked again by recalescence and a cooling rate decrease. The eutectic solidification stabilized at a growth temperature of 559°C. Soon after the eutectic reaction finished, the final Al-Cu phase development was marked once more by recalescence and a slight cooling rate decrease at 547°C. Al-Cu growth stabilized at around 533°C, after which the cooling rate gradually returned to the baseline curve, signalling the end of solidification. Each of the above growth phases were found to correlate well with solidification data from other 319 aluminum alloys (see Section 2.2.2.9) [48], [52], [55]–[61].

4.3.1.2 MASTER ALLOY THERMAL ANALYSIS

To accurately assess the effect of carbon inoculation, the cooling curves from the master alloy experiments were compared to the virgin B319 control curve at the α-Al and Al-Si solidification regions, which are most sensitive to grain refinement or modification and most identifiable graphically (distinguished as the first two defined peaks on the dT/dt line from Figure 4.14) [54], [76], [85].

Figure 4.15 and Figure 4.16 compare thermal plots of the master alloys to the control at the α-Al solidification region.

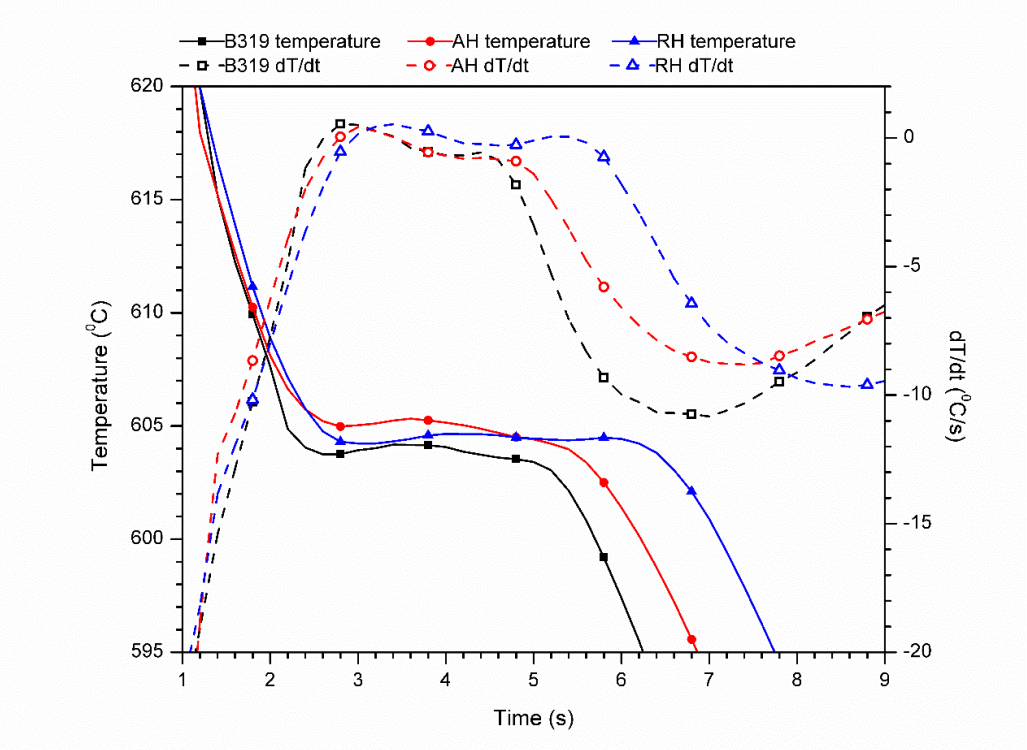

Figure 4.15: Cooling curves of the high concentration master alloys (AH & RH) vs. virgin B319 for the α-Al region

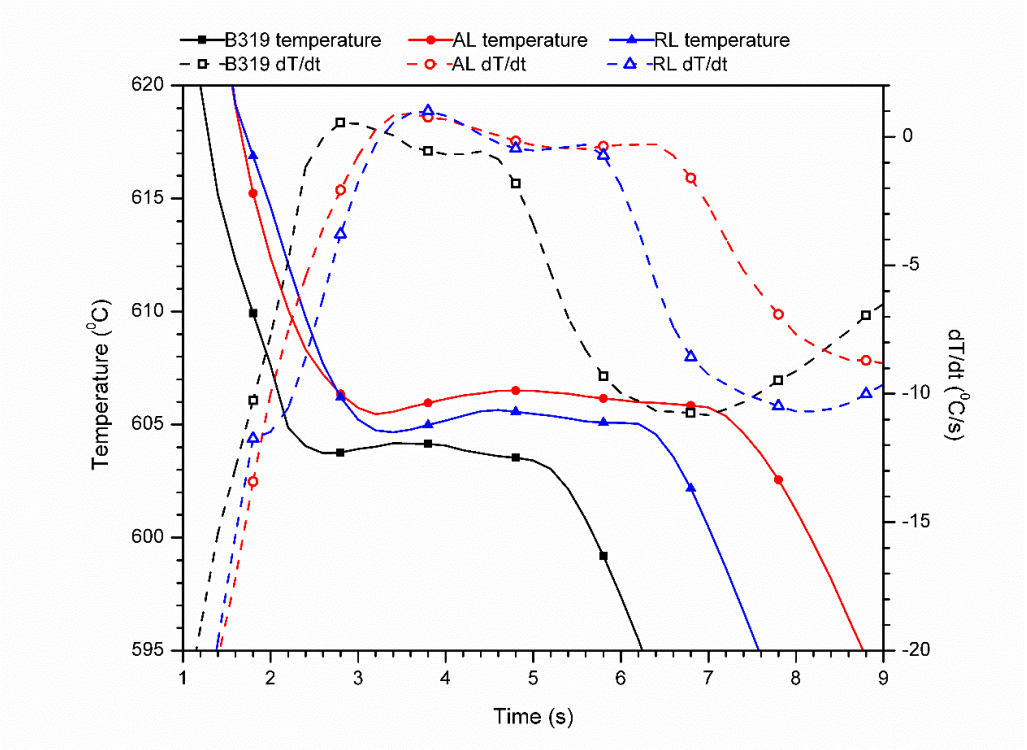

Figure 4.16: Cooling curves of the low concentration master alloys (AL & RL) vs. virgin B319 for the α-Al region

Figure 4.15 and Figure 4.16 both show that master alloy addition had little effect on the α-Al region of the cooling curve (T-t) and second derivative curve (dT/dt), compared to the virgin B319 alloy. This area of an aluminum cooling curve has proven to be important in predicting grain refinement or modification. In particular a (i) reduction of undercooling, (ii) increase of α-Al nucleation and growth temperature, or (iii) shrinking of dT/dt peak would suggest successful grain refinement [9], [76], [85]. The above figures show that master alloy addition seemed to have increased the α-Al growth temperature and growth time, which may indicate active added nucleation sites from the added carbon solute. However, both the undercooling and dT/dt peaks remained largely unchanged after master alloy addition and do not exemplify refinement. This suggests that overall the Al-C master alloy additions may not be altering the solidification process in any significant manner.

The aforementioned change in undercooling, or a general increase in the T-t line's slope over the plateau section, is possibly the most common indicator of grain refinement currently understood in literature [9]. Since inoculation acts on the principles of heterogenous nucleation, hypothetical maximum particle inoculation would be achieved at perfect heterogenous nucleation (when all solidification begins efficiently from foreign preferential nucleation sites). During perfect heterogenous nucleation, undercooling approaches zero. Therefore, all other parameters remaining equal, lower degrees of undercooling represent successful particle inoculation [9], [69]. When comparing undercooling at the α-Al regions (the difference between maximum and minimum temperatures in the plateau or growth region, found roughly between 3-7s for each figure), neither the high or low concentration master alloys had any significant effects within the accurate detection limit of the thermocouple (±0.4%, or approximately ±2.3°C for the 500-650°C range). The only notable effect of master alloy addition seems to be the lengthening of the α-Al growth period, which was the case for all experiments and was not seen for the PAl casting – signifying a possible response specific to carbon addition and not alloy dilution by pure aluminum. A lengthening of the α-Al growth period shows that there may be a larger release of latent heat, which may also mean that additional nucleation sites were activated [19], [153]. However, this effect may also represent the presence of minor dendritic growth restriction caused by the small amount of added carbon solute. This α-Al period lengthening seemed to translate down to the Al-Si growth period.

Figure 4.17 and Figure 4.18 compare thermal plots of the master alloys to the control at the Al-Si eutectic solidification region.

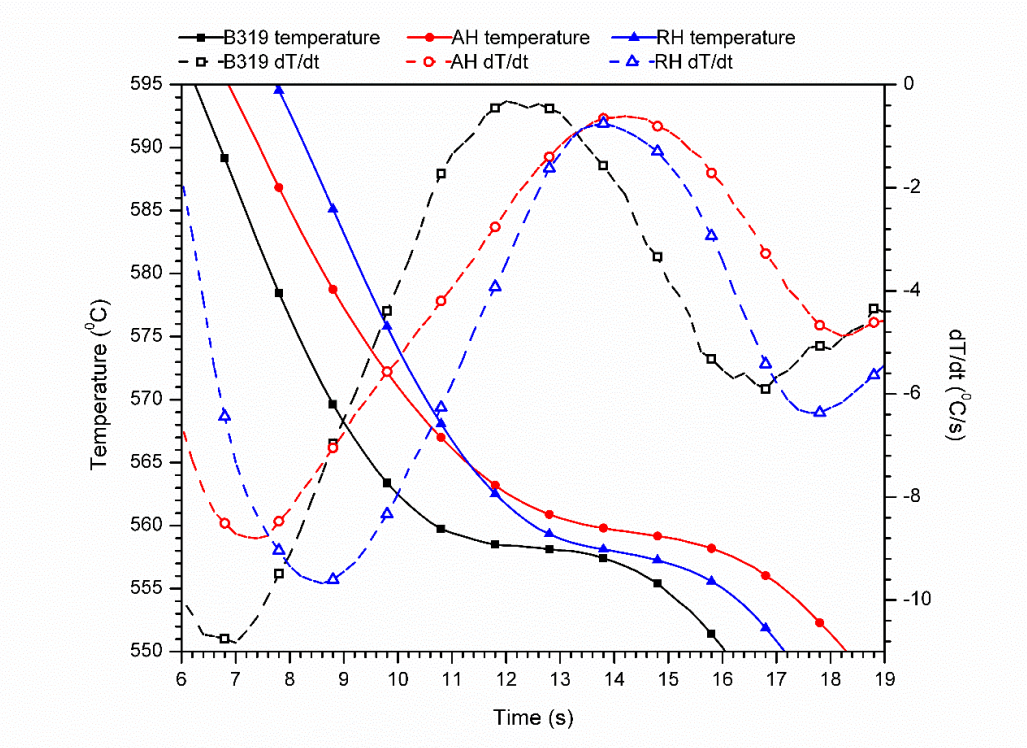

Figure 4.17: Cooling curves of the high concentration master alloys (AH & RH) vs. virgin B319 for the Al-Si region

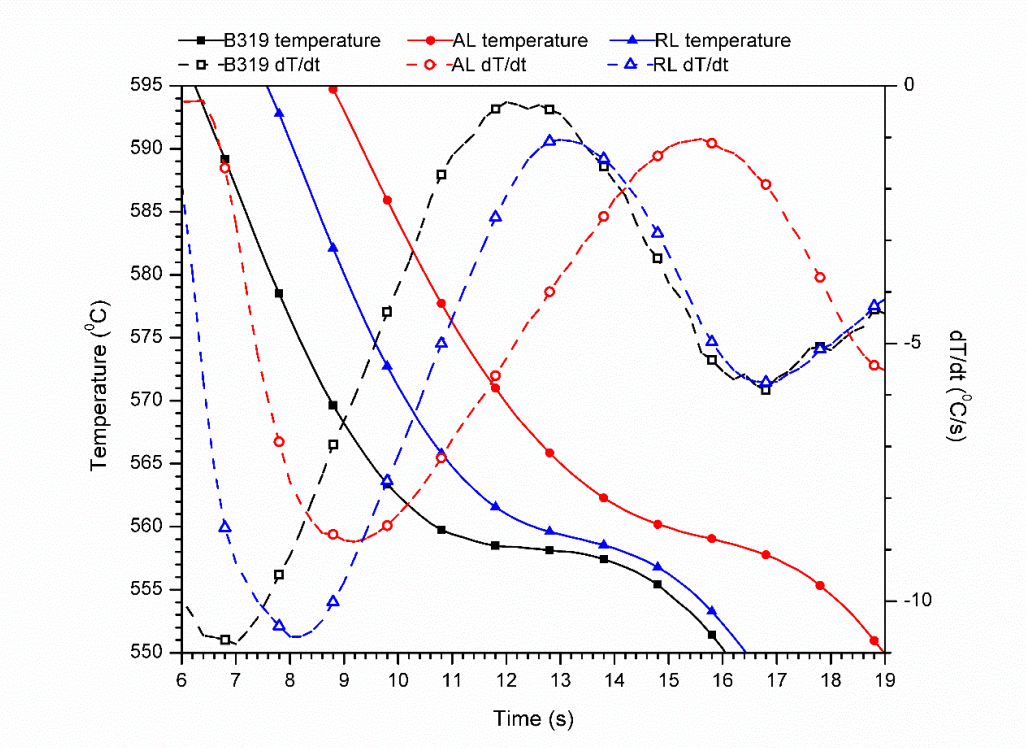

Figure 4.18: Cooling curves of the low concentration master alloys (AL & RL) vs. virgin B319 for the Al-Si region

Like the cooling curves seen at the α-Al region, the master alloy cooling curves near perfectly track the virgin B319 alloy curve over the Al-Si eutectic reaction region. The most prominent difference in the graphs was the right-hand curve shift seen for the master alloy castings, which is a consequence of the lengthened α-Al growth phase described above. Otherwise, visual analysis of Figure 4.17 and Figure 4.18 would suggested that Al-C master alloy addition did not modify the Al-Si eutectic reaction within detectable limits.

Table 4.4 shows the resultant thermal data points of interest for all casting groups. Each row and column lists the graphically determined thermal data as well as the deviation from the respective virgin B319 alloy data. If data points were seen to deviate significantly from the control (outside of the uncertainty range listed at the foot of the table), then the cell was coloured green for an increase or red for a decrease. Both high and low concertation master alloys produced a consistent increase in the $t_{G\,\alpha\text{-}Al}$ (α-Al growth time), which then also lead to minor increases in the overall *ts* (solidification time) and therefore lowered the alloy *CR* (cooling rate), however not significantly outside of the assumed uncertainty ranges. It is interesting to note that the cold casting experiments (B319CC and AHCC) displayed thermal curves very similar to those of the standard casting experiments, despite having an average pouring temperature of ~30°C under the standard castings (average pouring temperature of 676°C vs 706°C). Therefore, it can be assumed that the pouring temperature differential of ~30°C was not great enough to significantly alter the cooling rate or solidification time within the detection limits of these experiments. This was contrary to what was originally expect since a significantly lower pouring temperature, given the relatively small mass and wall thickness of the thermal mold, was assumed to produce a lower overall system equilibrium temperature. A lower equilibrium temperature was hypothesized to result in markedly higher cooling rates, as seen by Vandersluis [57].

Table 4.4: Thermal data for all casting categories

Alloy	Thermal data													
	$T_{N\ \alpha\text{-}Al}$ (°C)	$T_{G\ \alpha\text{-}Al}$ (°C)	T_{UC} (°C)	$t_{G\ \alpha\text{-}Al}$ (s)	$T_{N\ Al\text{-}Si}$ (°C)	$T_{G\ Al\text{-}Si}$ (°C)	$t_{G\ Al\text{-}Si}$ (s)	$T_{N\ Al\text{-}Cu}$ (°C)	$T_{G\ Al\text{-}Cu}$ (°C)	FR (°C)	t_s (s)	CR (°C/s)	T_{DCP} (°C)	$fs_{,DCP}$
B319	634	604	0.8	3.2	589	559	3.3	547	533	113	24.2	-4.7	589	0.76
PAl	631	608	0.5	3.1	589	560	3.1	548	527	111	20.15	-5.5	589	0.74
	-3	4	-0.3	-0.1	-	-	-0.2	1	-6	-2	-4.0	-0.8	-	-0.02
AL	643	606	0.7	3.7	589	559	3.5	548	530	126	25.75	-5.0	589	0.79
	9	3	-0.1	0.5	-	-	0.2	1	-3	14	1.6	-0.3	-	0.03
AH	634	606	0.4	3.9	594	560	3.8	549	533	114	28.35	-4.0	594	0.70
	-	2	-0.4	0.7	5	1	0.5	2	1	1	4.2	0.7	5	-0.06
RL	634	605	0.7	3.7	587	559	3.2	547	529	119	26.65	-4.5	587	0.76
	-	1	-0.1	0.5	-2	0	-0.1	0	-4	6	2.5	0.3	-2	-
RH	635	605	0.7	3.8	588	559	3.4	548	529	121	26.3	-4.6	588	0.75
	1	-	-	0.6	-1	0	0.1	1	-4	9	2.2	0.1	-1	-0.01
B319CC	633	607	0.0	3.7	587	558	3.2	547	531	118	26.75	-4.4	587	0.75
AHCC	633	607	0.0	4.0	588	559	4.0	548	526	116	28	-4.2	588	0.75
	-	-	-	0.3	1	1	0.8	1	-6	-2	1.3	0.2	1	-

For each thermal data point, the top figure represents the value while the bottom figure represents the deviation from the virgin B319 control castings. The table cells are colored if a value's deviation shows significances beyond experimental measurement uncertainty/tolerance:

T = ± 5°C , ΔT = ± 10°C, t = ± 0.4s, Δt = ± 0.8s, ΔT/Δt = ± 0.6°C/s

Figure 4.19 graphs the fraction sold versus temperature for master alloy additions compared to virgin B319 alloy castings. The fraction solid curves also show little effects of master alloy addition and each follow a similar slope, which should have steepened after inoculation or refinement according to experiments performed by Malekan and Shabestari [153]. The RL cast sample was an outlier and seen to have been translated to the right, however, as investigated in Section 4.3.2, this did not yield any appreciable change in the casting microscopy.

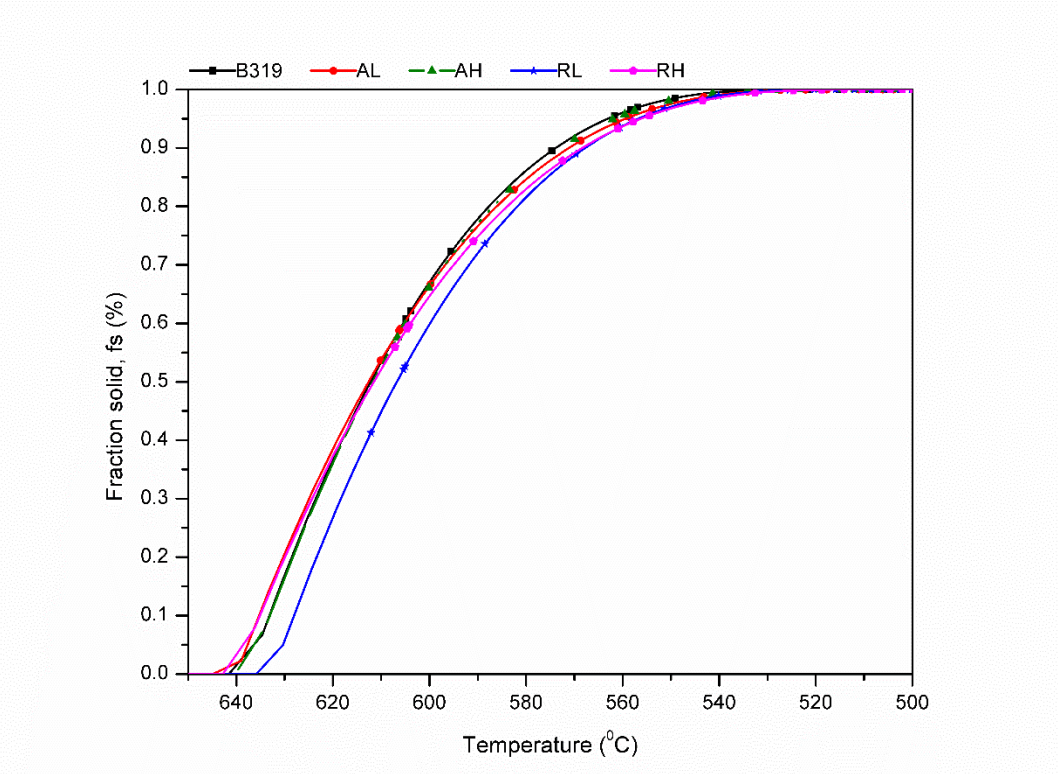

Figure 4.19: Fraction solid vs. temperature for thermal casting experiments

In the evaluation of the above thermal analysis data, it seems that the synthesized master alloys, at a hypothetical overall weight percentage of 0.03% carbon, did not have a significant effect on the thermal cooling curves of the B319 alloy that would indicate grain refinement or phase modification. Concentration of the master alloys, and alloy dilution, did not make a difference in the obtained thermal plots.

4.3.2 GRAIN SIZE EVALUATION

After casting in the thermal mold, samples for grain size evaluation were prepared and analyzed following the processes outlined in Sections 3.5.2.1 and 3.5.2.5. Figure 4.20 below shows a grain evaluation image of the virgin B319 alloy casting after etching.

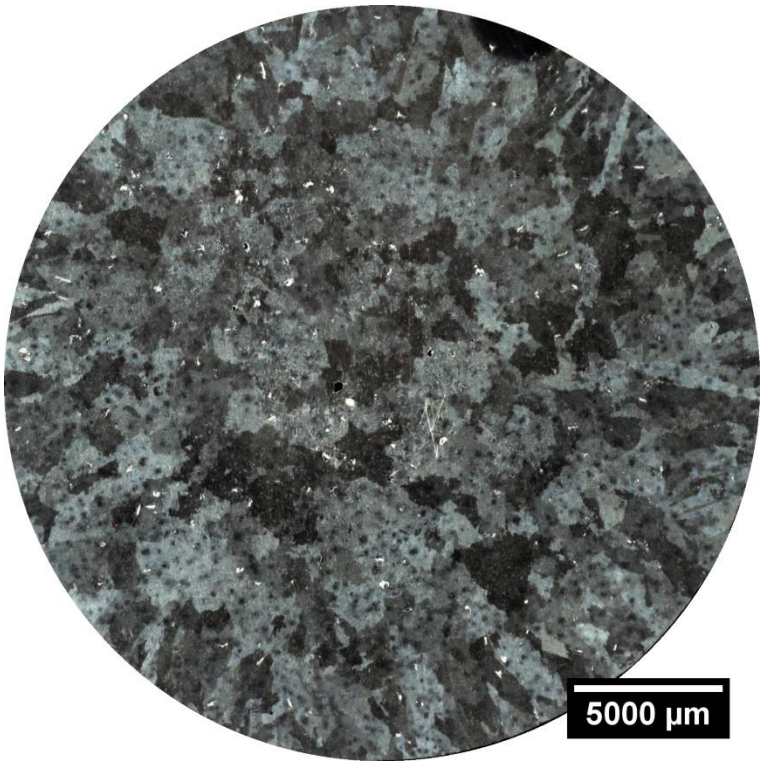

Figure 4.20: Grain structure of the virgin B319 alloy

The virgin B319 alloy had a generally equiaxed grain structure, with small regions of fine columnar grains at the sample edges. These columnar grains initially form from preferential nucleation at the mold walls, and then proceed to grow parallel to the heat flux gradient (the heat flux gradient flows radially from the centre outward, or from the hottest region to the coolest region). It was seen that columnar grain growth was arrested before 5000 µm from the mold wall, and an equiaxed structure took over, which is caused by dendritic growth restriction due to the high presences of solute in B319 and has been observed in other experiments reported in the literature that use permanent mold aluminum alloy castings [70]. The virgin B319 alloy castings were found to have an average grain size of 915 µm.

Figure 4.21 shows the results from all sample grain measurements.

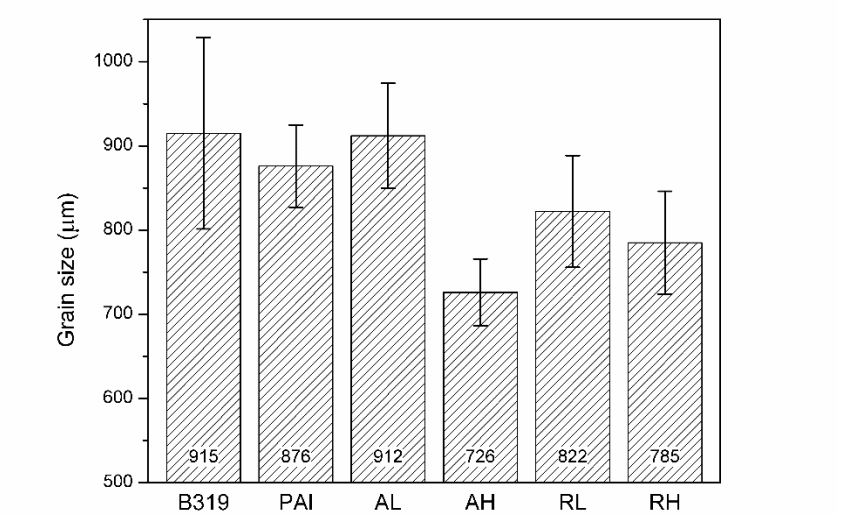

Figure 4.21: Grain size measurements (error bars represent standard deviation)

Comparing each casting to the virgin B319 alloy, the following grain size changes were seen: (i) PAl saw a 4.3% grain size reduction, (ii) AL saw a 0.4% grain size reduction, (iii) AH saw a 20.7% grain size reduction, (iv) RL saw a 10.2% grain size reduction, and (v) RH saw a 14.3% grain size reduction.

Referring to the thermal analysis results of Table 4.4, the high concentration samples AH and RH showed the largest increases in α-Al growth time and showed the largest decreases in grain size. These results suggest that some limited grain refinement may have been caused by the less dispersed carbon black particles, acting more effectively to create local solute growth restriction of the α-Al dendrites or functioning better as larger nucleant particles when agglomerated [9]. However, since 0.03wt% C was added for all four master alloys it would have been expected that the AL and RL casting would have shown some refinement as well. Accounting for the 4.3% grain size reduction observed by the PAl control casting, no significant results were seen for AL and RL. In fact, when compared against the PAl casting, AH and RH showed only ~17% and ~10% grain size refinement, respectively. Literature on current industrial aluminum alloy refiners (such as Al-TiC and Al-Ti-B) report ~60-80% grain size reduction after master alloy addition [85], [89], [94], [154]. Figure 4.22 displays images of each sample for grain structure comparison. AH shows a degree is visually apparent grain refinement, particularly a more fully equiaxed grain structure at the sample extremities.

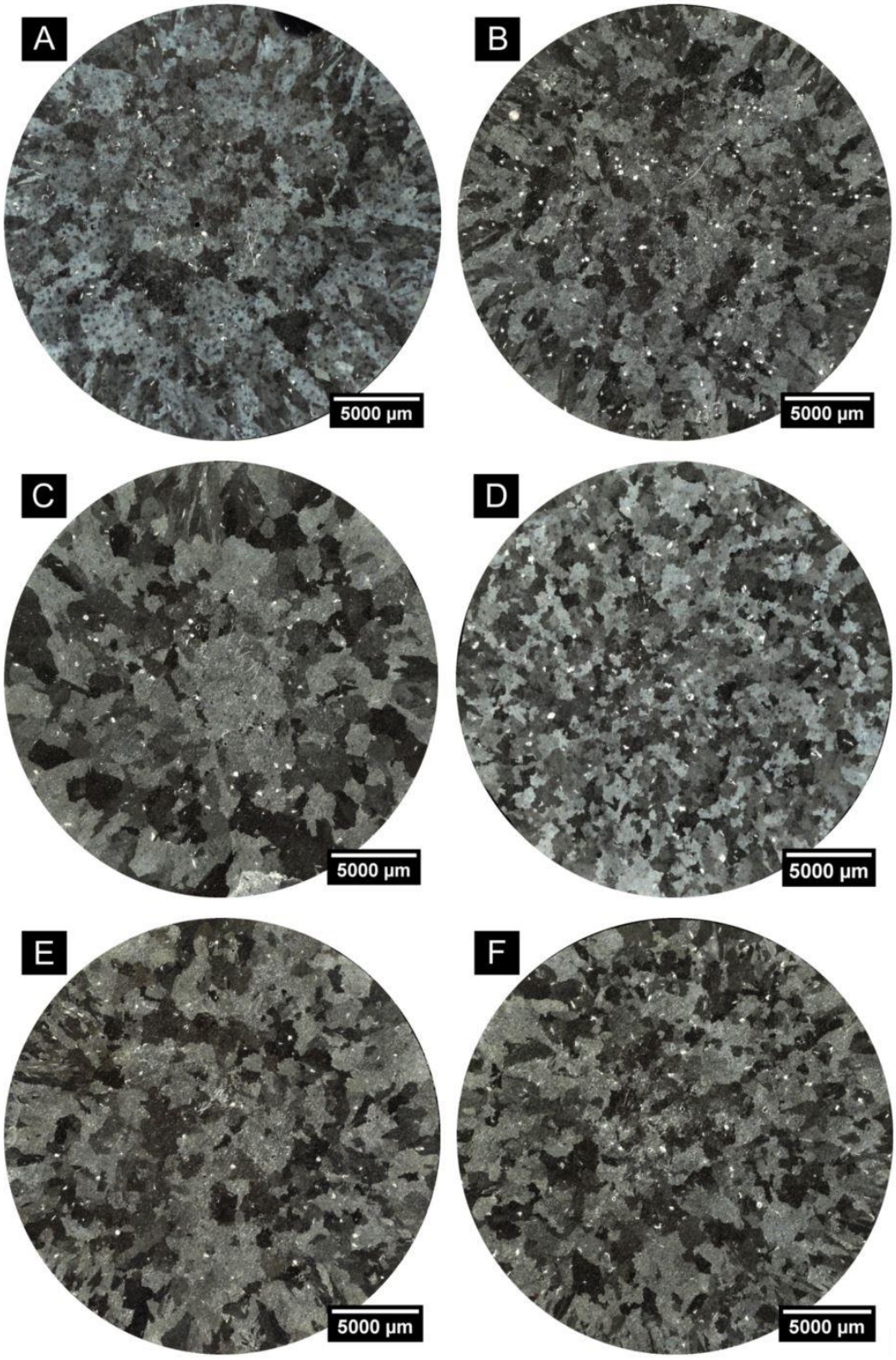

Figure 4.22: Grain structure images of cast samples; (a) virgin B319, (b) PAI, (c) AL, (d) AH, (e) RL, and (f) RH

To test the refinement effects of AH at lower pouring temperatures, cold castings of the virgin B319 alloy (B319CC) and of AH (AHCC) were compared to the standard castings, as seen in Figure 4.23 and Figure 4.24 below.

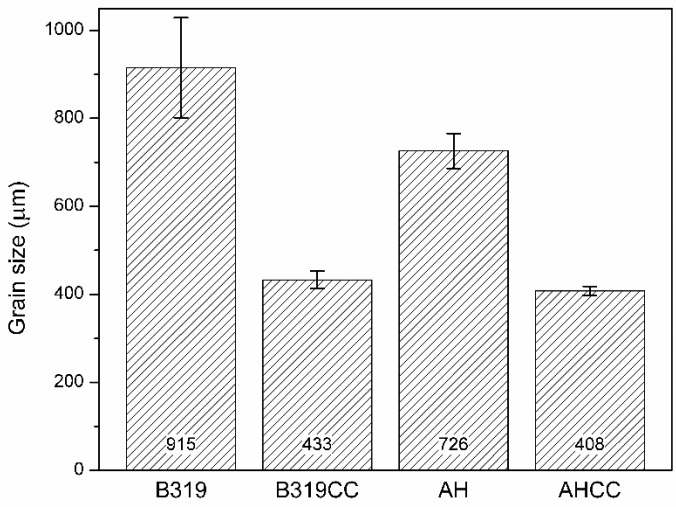

Figure 4.23: Grain size measurements of cold casted samples (error bars represent standard deviation)

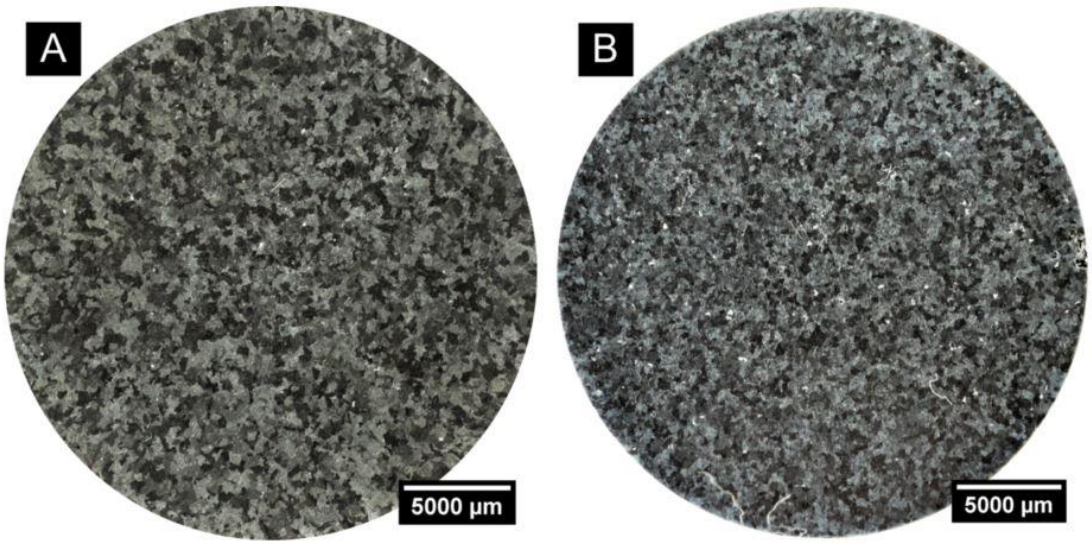

Figure 4.24: Grain structure images of cold casting; (a) virgin B319CC,(b) AHCC

Although showing some limited grain refinement at higher pouring temperatures (~710°C), the AH master alloy had very little effect on the grain structure at lower pouring temperatures compared to the virgin B319 alloy (~680°C).

The grain size results for all casting categories was tested for correlation against casting parameters (pouring temperature, super heat temperatures, etc.) and thermal data (Table 4.4) using an adjusted least squares linear regression. The highest R^2_{adj} values corresponded to the casting pouring temperatures ($R^2_{adj,\ pour\ T}$ = 0.794) and the undercooling temperatures ($R^2_{adj,\ Tuc}$ = 0.677). All other casting parameters and thermal data showed R^2 correlation of less then 0.50, including the R^2 of α-Al growth time against grain size ($R^2_{adj,\ t_{G,\alpha\text{-}Al}}$ = 0.085). Therefore, since the T_{UC} values are not considered significant regarding the thermal couple measurement limits, carbon black particles at 0.03wt% did not appear to have a significant grain refining potency in the B319 alloy.

4.3.3 X-RAY DIFFRACTION

XRD analysis was performed on the cast thermal samples and the results can be seen in Figure 4.1 below.

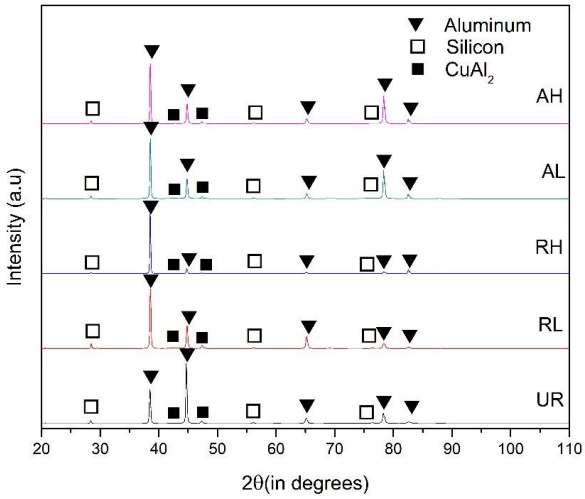

Figure 4.25: XRD spectra of thermal castings

Each sample showed peaks corresponding to the three primary phases in the B319 alloy: α-Al, Al-Si eutectic, and Al-Cu intermetallics ($CuAl_2$) [6]. The other known phases, including Fe, Mn, Mg, Ni, Zn, and Ti, were below the XRD detection limit and not visible in the data. The master alloy C additive was also below the detection limit and is not seen in any master alloy casting.

4.3.4 MICROSCOPY AND CHEMICAL ANALYSIS

SEM micrographs found the virgin B319 alloy to have a primary aluminum matrix, with eutectic and intermetallic phases forming between the aluminum dendrite arms. Three principal phases were identifiable by EDX analysis: (i) elemental Si eutectic, (ii) Al-Cu intermetallics, and (iii) Al-

Fe intermetallics. These phases and their morphologies are shown in Figure 4.26 and their compositions are listed in Table 4.5.

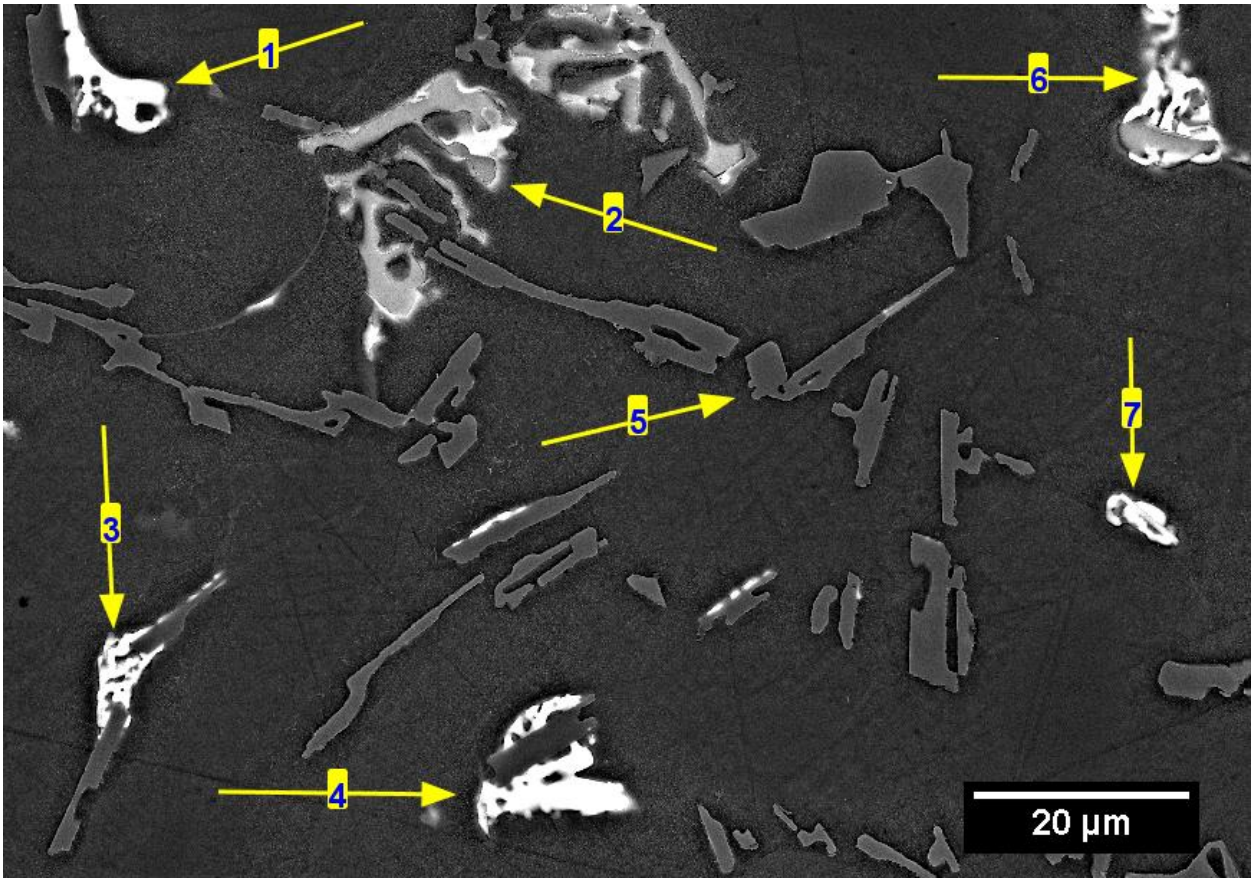

Figure 4.26: SEM micrograph of the virgin B319 alloy (BSE); (1,3,4,6,7) Al-Cu, (2) Al-Fei, (5) Si

Table 4.5: EDX point spectrum composition for the virgin B319 alloy (Figure 4.26)

Point	1	2	3	4	5	6	7	-
Phase(s)	Al-Cu	Al-Fe	Al-Cu	Al-Cu	Si	Al-Cu	Al-Cu	α-Al
Morphology	blocky	script	lamellar	blocky	acicular	lamellar	blocky	dendritic
Composition (wt%)								
Mg	0.05	0.03	0.10	0.08	0.05	0.10	0.08	0.08
Al	54.48	61.79	57.74	54.82	30.38	55.05	55.08	95.56
Si	0.86	7.83	1.20	0.74	68.38	0.75	5.35	0.85
Ti	0.01	0.05	0.03	0	0.01	0.05	0	0.36
Cr	0	1.37	0.03	0	0.03	0	0.02	0.06
Mn	0.04	5.84	0.05	0.02	0	0.05	0.10	0.11
Fe	0.25	15.35	0.12	0.08	0	0.35	1.74	0.04
Ni	2.13	1.00	3.12	1.31	0	3.81	10.90	0.06
Cu	41.73	6.24	37.15	42.41	0.86	39.51	26.15	1.77
Zn	0.46	0.52	0.46	0.56	0.30	0.35	0.57	1.12

Points 1, 3, 4, 6, and 7 show the $CuAl_2$ intermetallics present in the B319 alloy, which are identified by a high concentration of copper (between 25-50wt%) [6], [25], [32]. Relatively high nickel concentrations (up to 10.9 wt%) were also found at the $CuAl_2$ sites, which is also reported in the literature and signifies the presences of Al_3Ni or Al_3CuNi along side the Al-Cu phases [6]. In general, the Al-Cu-Ni phases form adjacent to the Si particles or other intermetallic phases since the Al-Cu precipitation is one of the last solidification reactions and takes place at the dendrite boundaries, around the already solid Al-Fe intermetallics and Al-Si eutectic.

Point 2 shows a script formation of the α-$Al_{15}(Fe,Mn)_3Si_2$, denoted by high relative concentrations of iron and manganese (up to 18wt% Fe and 9wt% Mn) [36], [41], [42]. It can also be seen that point 2 contains some copper and nickel and shows the presence of a denser Al-Cu-Ni intermetallic forming around the edges. This would supported the claim by Li *et* al.[32] that the Al-Fe intermetallics may act as nucleants for precipitation of the Al-Cu intermetallics. Adjusting for the included presence of copper and nickel at the edges, point 2 showed approximately 67wt% Al, 9wt% Si, and 24wt% of [Cr,Mn,Fe]; which near perfectly fits stoichiometric ratio for α-$Al_{15}(Fe,Mn)_3Si_2$ (64wt% Al, 9wt% Si, and 27wt% [Cr,Mn,Fe]). The β-Fe phase suggested in literature was not found in the samples, as was also seen in the research of Kumar [19].

Point 5 shows the formation of acicular silicon, and has a composition of high Al and high Si, which represent nearly pure silicon particles formed amongst aluminum in the Al-Si eutectic reaction [7], [20], [25].

The alloying elements magnesium, titanium, and zinc were not seen to form any visually obvious phases in the cast samples. Magnesium had a total reported weight percentage of 0.05% in the pre-cast B319 billet and was likely finely distributed in the microstructure around silicon as Mg_2Si, around Al-Cu as $Al_5Cu_2Mg_8Si_6$, around Al-Fe as π-$Al_8FeMg_3Si_6$, and in the α-Al matrix as $Al_2Mg_3Zn_3$ [7], [30], [36], [41], [44], [46], [47]. Compositional results show that magnesium was preferentially found either around the Al-Cu phases or within the α-Al matrix. Titanium was present in the α-Al matrix (up to 0.5wt% Ti), and likely takes the form of the nucleant $TiAl_3$ [8]. Zinc was also present in the α-Al matrix (up to 1.36wt% Zn), in the form of either $Al_2Mg_3Zn_3$ or $MgZn_2$ [7].

Figure 1.26 shows an EDX map scan of a separate zone on the virgin B319 alloy, clearly showing the principal phases.

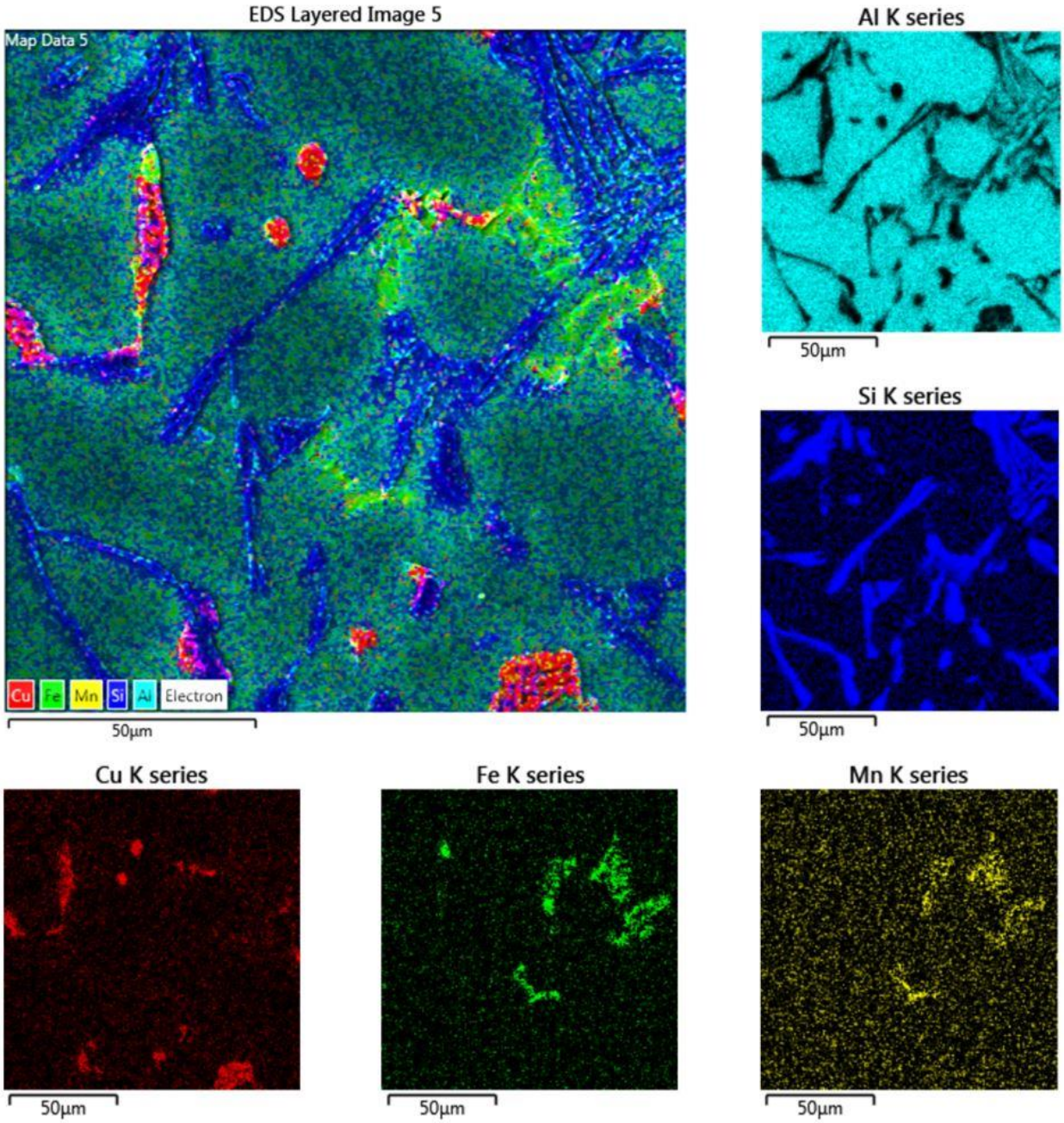

Figure 4.27: EDX map scan of the virgin B319 alloy

The addition of an Al-C master alloy (both low and high concentration) was not seen to make any significant changes to the microstructure of the castings. Neither the added pure aluminum (~3wt% Al for PAl, AL and RL; and ~1.5wt% Al for AH and RH) or the added carbon particles (0.03wt% C) showed any identifiable morphological modifications to the principal phases presented above. Figure 4.28 shows the virgin B319 alloy casting versus an AH master alloy casting for reference.

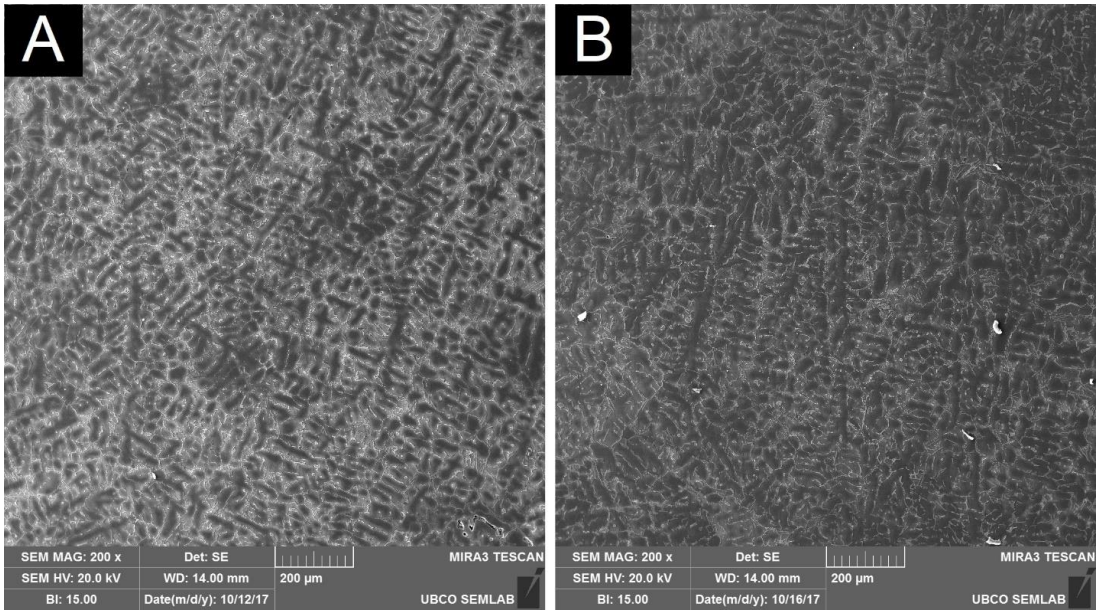

Figure 4.28: SEM micrographs of thermal castings; (a) virgin B319,(b) AH

It was hypothesized that master alloy addition would have little effect on the virgin B319 alloy's microstructure, as there were no substantial recorded alterations to either the grain size or thermal cooling curves. Since carbon is not reliably detected by EDXS, especially at small concentrations, it was not feasible to use EDXS analysis to find carbon presence in the cast samples. The carbon inoculants could only have been found visually through SEM analysis, which was unsuccessful. Either the particles were dispersed and too small to be visible/noticed, or agglomeration and floatation isolated the particles to specific regions outside of the sectioned microscopy plane or out of the cast sample all together.

4.3.5 FLUIDITY CASTINGS

The fluidity castings were performed to evaluate the effects of the Al-C master alloy on the fluidity of the molten B319 alloy. Figure 4.29 shows a virgin B319 alloy fluidity casting, prepared and measured following the procedure outlined in Section 3.5.2.4.

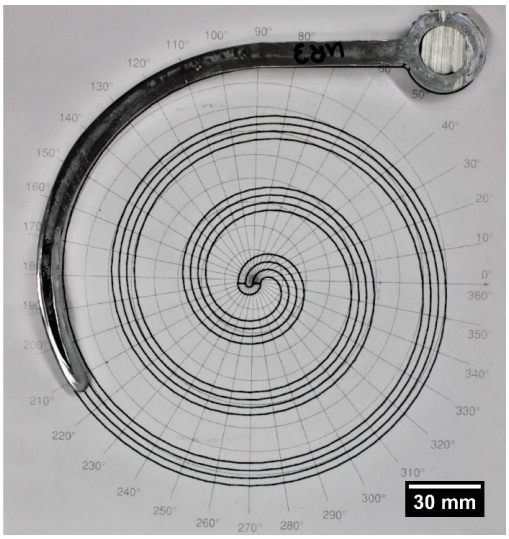

Figure 4.29: Fluidity casting of the virgin B319 alloy

Figure 4.30 shows the results obtained after all casting samples were measured.

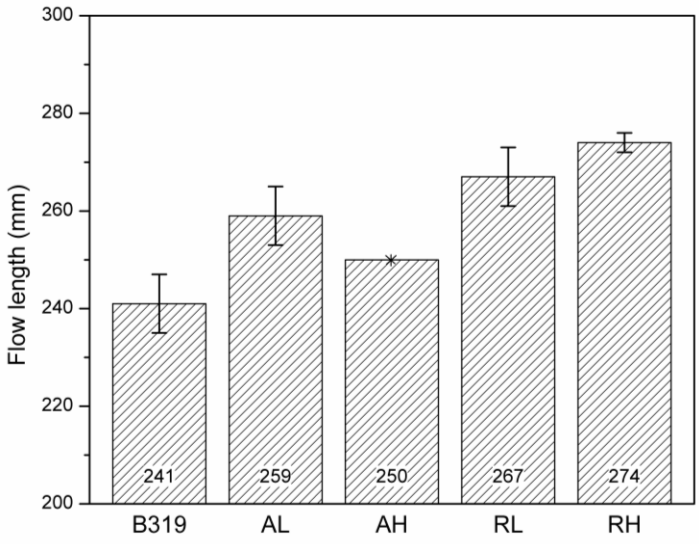

Figure 4.30: Fluidity mold flow lengths (error bars represent standard deviation)

The master alloys additives, particularly RL and RH, seemed to show an average positive effect on the molten fluidity of the B319 alloy. Travel lengths down the spiral were increased between

4-14% with the addition of the Al-C master alloy, with no distinct difference seen between master alloy concentration levels. Molten alloy fluidity is a multifaceted technological property, and can be influenced by a number of factors including: (i) composition, (ii) oxide/slag inclusion, and (iii) temperature parameters such as mold temperature and pouring temperature [124]. The experimental procedure, outlined in Section 3.4.5, was set-up to control for items (ii) and (iii). Therefore, it is most likely that the observed fluidity changes were primarily influenced by compositional changes to the cast alloy. However, the exact compositional mechanisms related to fluidity variations among cast aluminum alloys is largely debated. According to a study of fluidity in Al-Si alloys, Loper [155] stated that decreasing the concentration of alloying elements such as Cu, Fe, Mg, or Mn has been shown to increase fluidity. Consequently, one mechanism for this work's observed fluidity increase could have been the alloy dilution associated with the added pure aluminum via the master alloy. This supports early work by Mollard *et al.* [156], who found the fluidity of pure aluminum to decrease with rising impurity elements. Yet, it was also found that for the compositional range of the B319 alloy, decreases in none-Si alloying elements lead only to minimal changes in fluidity, often within the limits of standard error [157], [158]. If solute dilution was the sole driving factor, it would have been expected that low concentration master alloys would yield better fluidity results since they provided high levels of dilution – this was not seen, as RH provided the highest fluidity increase and smallest standard deviation in results. Additionally, a decrease in solute concentration of Si (alloys of < 15wt% Si) showed lower levels of fluidity [159]. Grain refinement and modification has also been recorded to alter alloy fluidity [124], but since no apparent grain refinement and modification was seen for the Al-C master alloys in earlier sections, this was not investigated any further.

Further investigation is warranted into the mechanisms of fluidity change in the B319 alloy, which is an in depth and complex topic not within the scope of this research.

4.4 MECHANICAL PROPERTIES

To further study the effects of carbon black inoculation in the B319 alloy, casting samples were tested for hardness and machined into tensile and Charpy specimens. The following sections discuss the results from the mechanical properties testing.

4.4.1 TENSILE TESTING

The results from the tensile tests are shown in Figure 4.31. The virgin B319 alloy was found to have the highest tensile strength and the highest modulus of elasticity when compared to any of

the master alloy casting categories. Therefore, the addition of a carbon containing master alloy seems to have produced a negative effect on the B319 alloy's strength and ductility.

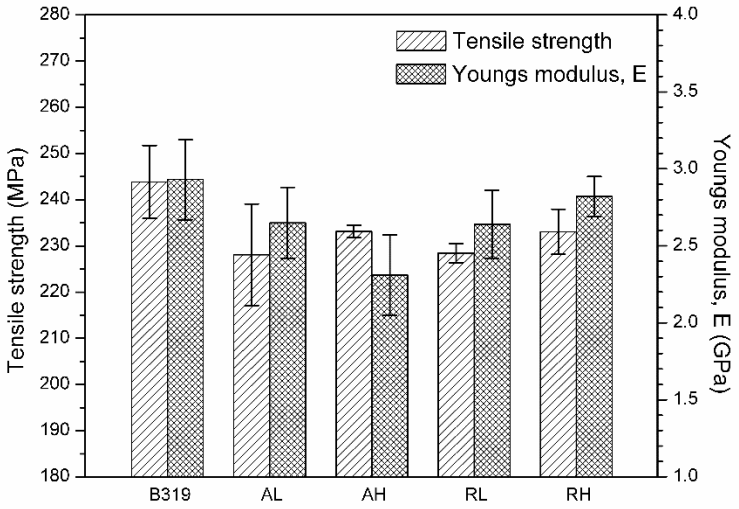

Figure 4.31: Tensile strength and Youngs modulus of cast mechanical samples (error bars represent standard deviation)

Figure 4.31 also shows that there was a correlation between sample tensile strength and sample modulus of elasticity. This can be explained by the brittle fracture mode of the samples, which did not exhibit a differentiable elastic/plastic region – seen in Figure 4.32. Figure 4.33 shows an image of a virgin B319 alloy tensile sample, which displays a brittle fracture with no cup-cone morphology that is associated with ductile materials [160]. This confirms previous research by Kumar [19], showing the B319 alloy to be a relatively brittle alloy in the as-cast state. In industry, heat treatments are often used to increase alloy ductility and overall toughness [6], [7], [33]

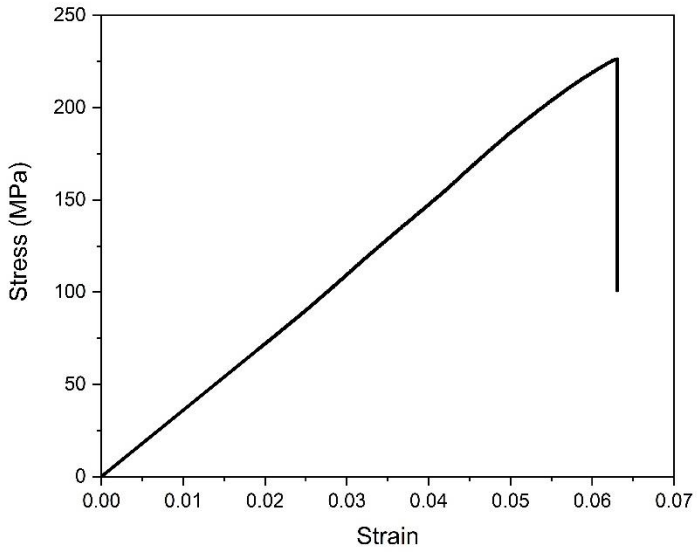

Figure 4.32: Stress-strain tensile curve for cast RL tensile sample

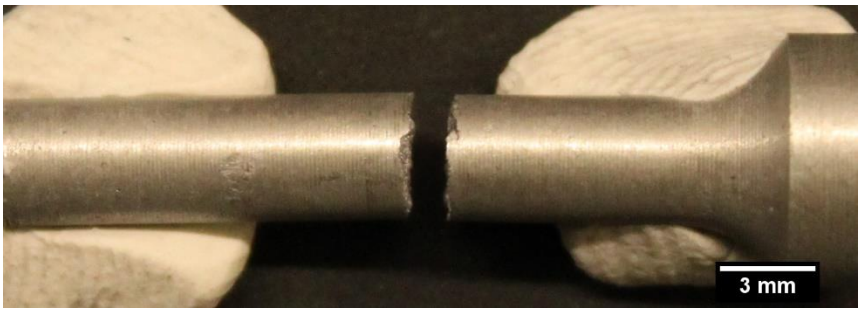

Figure 4.33: Fractured tensile sample of the virgin B319 alloy

Since master alloy addition seemed to have caused a decrease in tensile strength and ductility, sample tensile strength was compared against casting density and grain size to check for correlations. The results are shown in Figure 4.34 and Figure 4.35 below.

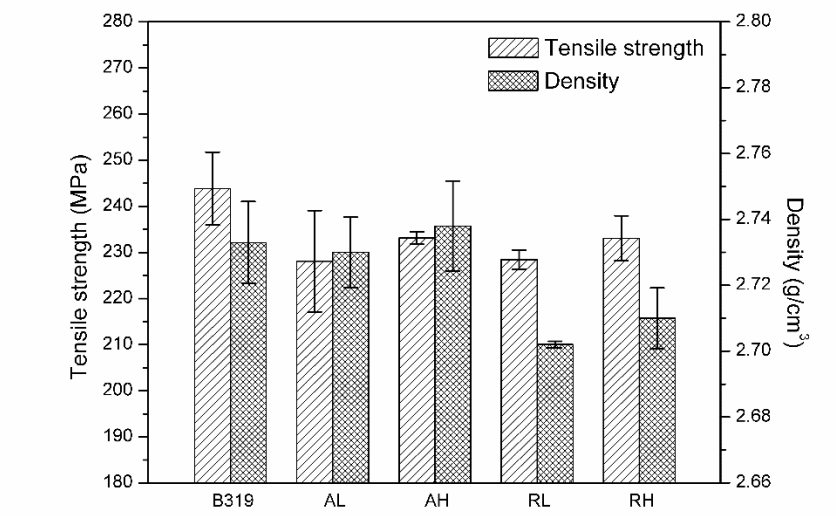

Figure 4.34: Tensile strength and density of cast mechanical samples

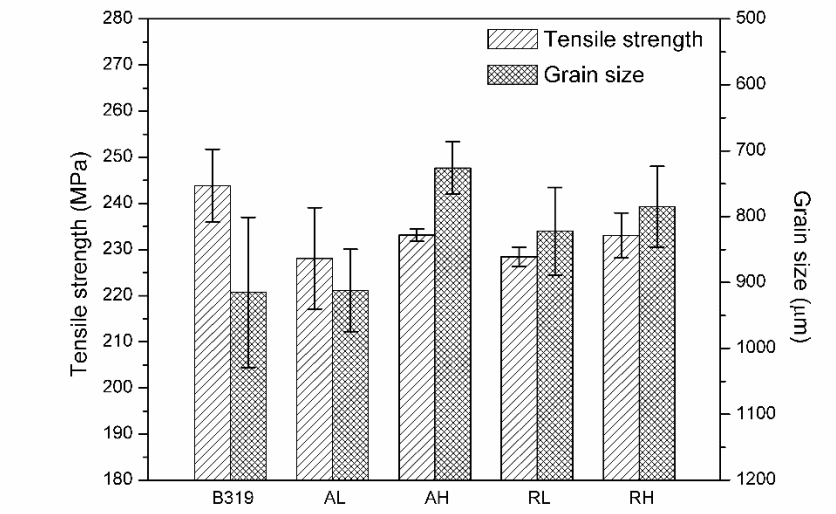

Figure 4.35: Tensile strength and grain size of cast mechanical samples

No bulk correlation was seen in Figure 4.34 to suggest that casting density or macro porosity was exclusively responsible for the loss of strength. Additionally, if grain size played any significant role in tensile property variation, Figure 4.35 should have shown an inverse correlation between strength and grain size as dictated by the Hall-Petch equation [160], which was not seen.

It is thought that the loss of strength and ductility seen after master alloy addition is due to either oxide/impurity inclusion or micro porosity (often caused by hydrogen entrapment) [6]. Since the master alloy addition castings were mixed and the unaltered castings were not, there is a much great chance for inclusion or hydrogen entrapment. Verification of this would require further

advanced material characterization and supplementary experimental controls, which are outside the scope of this thesis.

4.4.2 HARDNESS TESTING

Vickers microhardness testing was done on the cast samples to verify that there were no microstructural differences in terms of phase fractions (α-Al, Al-Cu, Si, Al-Fe, etc.). Unlike macrohardness, microhardness tests are unaffected by the Hall-Petch relation due to absence of the grain boundary effect since the impact point is small enough to take hardness measurements inside of grains and phases rather than across multiple grains/boundaries [161]. For example, in Figure 4.36 cold casted samples (B319CC and AHCC) produced a nearly 50% decrease in grain size but no significant change in microhardness.

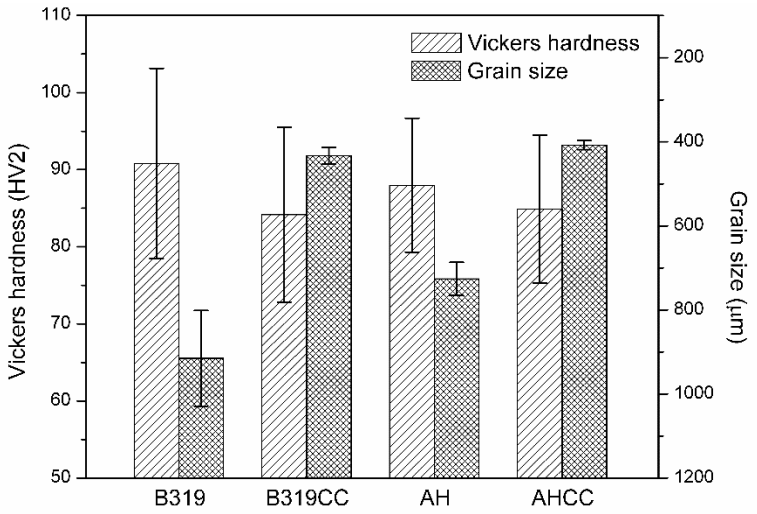

Figure 4.36: Vickers hardness and grain size of the virgin B319 and AH castings compared against their respective cold casting

Since B319 is a precipitation/age hardening material, the alloy would likely show a significant increase in hardness with a change in phase fractions (Al-Cu phase agglomeration for instance) [162]. Figure 4.37 shows that there was no significant change in the average microhardness of each casting category, which confirms that master alloy addition had no apparent effect on microstructure and phase fractions.

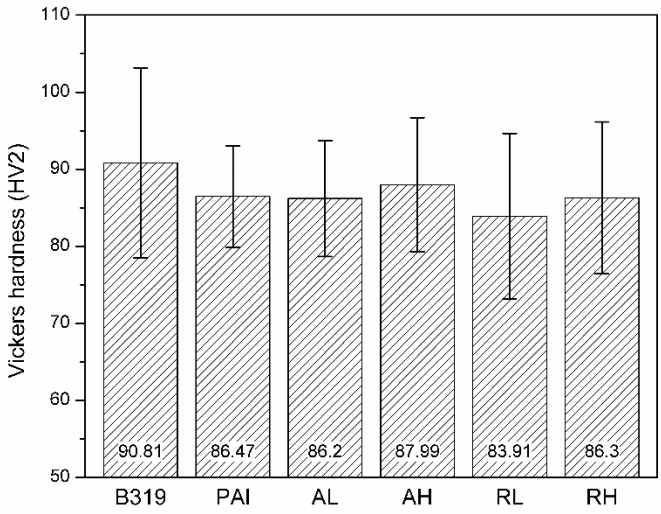

Figure 4.37: Vickers hardness of cast samples

4.4.3 CHARPY TESTING

The Charpy impact test results can be seen in Figure 4.38 below.

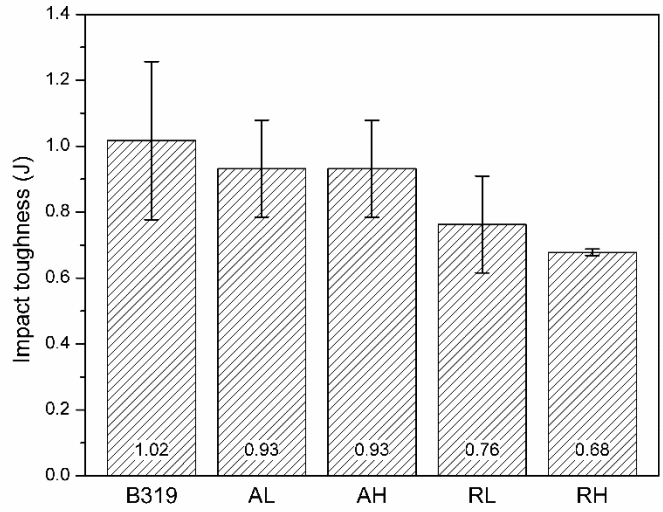

Figure 4.38: Charpy impact test results for cast samples

Apart from the RH sample outliers, master alloy addition showed little change on the impact toughness of the B319 alloy. Like the results obtained in tensile testing, the Al-C master alloy produced either no effect or a slight negative effect compared to the virgin B319 alloy. The lowered results obtained by the RH cast samples could likely be attributed to porosity or fracture surface defects.

In general, all casting exhibited a brittle fracture mode. Figure 4.39 shows a representative sample of the virgin B319 alloy, which displays a clean brittle fracture surface with no obvious plastic deformation. Figure 4.40 however, shows an example of a more ductile material after Charpy testing, in which clear plastic deformation can be seen for reference.

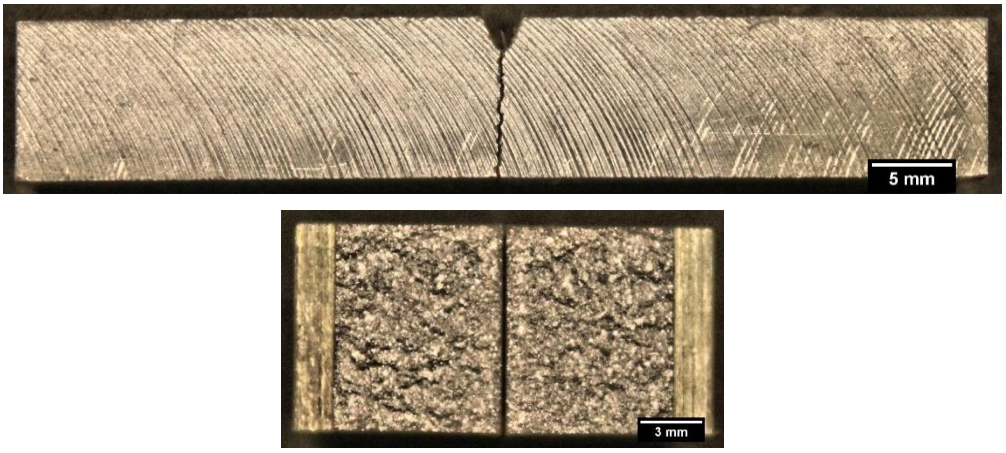

Figure 4.39: Fractured Charpy sample of the virgin B319 alloy

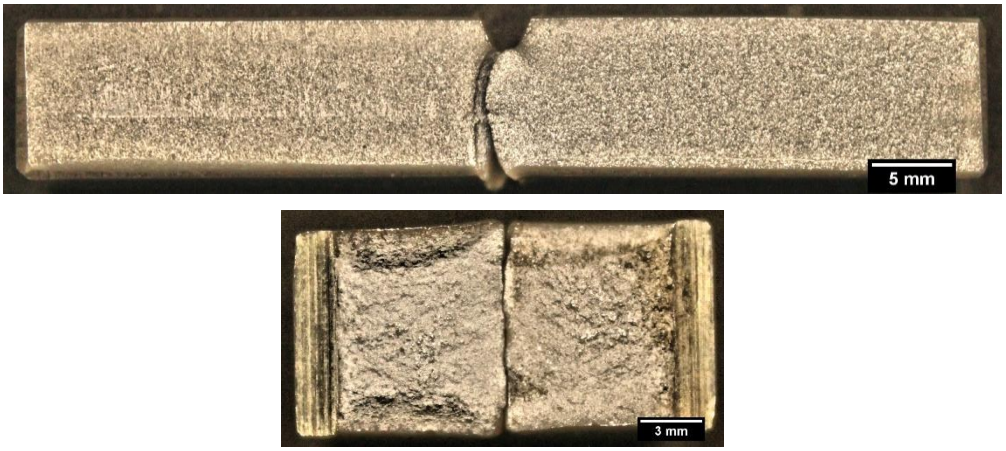

Figure 4.40: Fractured Charpy sample of 6061 aluminum

CHAPTER 5: CONCLUSIONS

This chapter reviews key findings from the results of this thesis and suggests future research related to the topics investigated in this work.

5.1 CONCLUSIONS

This study investigated both the SPS of a homogenous Al-C master alloy and the addition of this master alloy to the B319 alloy during casting. Listed below are the main conclusions drawn from this work:

PRECURSOR EXPERIMENTS

1. For the SPS synthesis of an Al-C master alloy, a composition of 2wt% carbon black was found to be the maximum limit for a homogenous and dense pellet. 10wt% and 5wt% carbon black were both seen to exhibit high degrees of agglomeration and low densification.

CHARACTERIZATION OF PRE-CAST MATERIALS

1. The carbon black powders exhibited nano-scale morphology, with average aggregate agglomerates of 183 nm and 307 nm for C_A and C_R respectively.
2. EDX and XRD results showed the presence of zinc sulphide and silicon in the recycled carbon black powder.
3. The SPS master alloys showed a decrease in densification of 4.7%, 5.8%, 2.4%, and 2.6% for AH, RH, AL, and RL, respectively when compared against the pure aluminum baseline pellet (ρ_{Al} = 2.646 g/cm^3). High concentration master alloys (2wt% C), exhibited the lowest densities due to the increased carbon black content.
4. SEM EDX analysis of the master alloys after sintering confirmed the presence of carbon black powder at the aluminum particle boundaries as well as a thin diffusion layer between Al and C, thought to be the Al_4C_3 formation previously seen in literature.

CASTING RESULTS

THERMAL ANALYSIS

1. Thermal analysis of the B319 alloy showed phase evolutions of the α-Al dendritic network, the Al-Si eutectic, and the Al-Cu intermetallics; these temperatures agreed closely with the ranges reported in literature.

2. Neither the high or low concentration master alloys had any significant effects on the degree of α-Al undercooling, indicating little grain refinement response from Al-C addition.
3. The solidification cooling curve of the B319 alloy was generally unchanged after master alloy addition.
4. Master alloy addition had very little effect on the fraction solid curve of the B319 alloy.

GRAIN SIZE EVALUATION

1. The virgin B319 alloy samples showed a mostly equiaxed grain structure with some columnar structure around the casting edge and an average grain size of 915 µm.
2. The addition of the Al-C master alloys showed no significant grain size reduction, the best result was seen by the AH master alloy and decreased grain size by ~17% compared against the PAl control.
3. The cold casting experiments showed no difference in grain size between the virign B319CC alloy and AHCC addition.
4. Grain size was compared against the thermal data and found to most closely correlate with the pouring temperature, with an adjusted $R^2 = 0.794$. There were no other correlations above an adjusted R^2 of 0.70.

MICROSCOPY AND CHEMICAL ANALYSIS

1. Four dominant phases were found in the B319 alloy microstructure and matched the expected morphologies described in previous literature: an α-Al dendritic network, with acicular elemental silicon, script α-$Al_{15}(Fe,Mn)_3Si_2$, and both blocky and lamellar $CuAl_2$.
2. The addition of the Al-C master alloys had no noticeable effect on the microstructure or morphology of the B319 alloy's phases.
3. No carbon black particles were found or detectable in the master alloy casted samples.

FLUIDITY CASTING

1. Master alloy addition showed a small increase in fluidity of between 4-14%, with the highest increase associated to the RH cast samples. This result was linear or correlation to master alloy concentration.

MECHANICAL PROPERTIES

TENSILE TESTING

1. The virgin B319 alloy exhibited both the highest tensile strength and highest modulus of elasticity.

2. All cast samples experienced brittle fracture and showed no plastic region on the stress strain curves.
3. No correlation was found between sample tensile strength and casting density (porosity).

HARDNESS TESTING

1. Microhardness testing verified that Al-C master alloy addition did not change the phase fractions of the B319 alloy.

CHARPY TESTING

1. There was no clear change to the B319 alloy's fracture toughness with master alloy addition.
2. All samples showed a brittle fracture mode

5.2 FUTURE WORK

The following sections could be modified or expanded upon in the future to further study the area of this research:

FLUIDITY CASTING

1. The mechanisms of fluidity change for the B319 alloy require a more in-depth study, while there is also a general gap in current research on the full understanding of fluidity changes among cast aluminum alloys.
2. The custom designed mold used for this research could be improved and adapted to test various casting and compositional parameters of alloy fluidity.

BIBLIOGRAPHY

[1] United States Enviromental Protection Agency, “Reducing Greenhouse Gas Emissions,” 2017. [Online]. Available: https://archive.epa.gov/epa/climatechange/reducing-greenhouse-gas-emissions.html. [Accessed: 25-Aug-2018].

[2] Enviroment and Climate Change Canada, “Greenhouse gas sources and sinks in Canada,” 2018.

[3] R. D. Gray, *Alloys and Automobiles: The life of Elwood Haynes*. Guild Press Emmis Publishing, 1979.

[4] The Aluminum Association, “Unprecedented Growth Expected for Automotive Aluminum as Multi-Material Vehicles Ascend, New Survey of Automakers Says,” 2017. [Online]. Available: http://www.aluminum.org/news/unprecedented-growth-expected-automotive-aluminum-multi-material-vehicles-ascend-new-survey. [Accessed: 25-Aug-2018].

[5] Ducker Worldwide, “Ducker Worldwide study: aluminum content in cars (public summary),” 2016. [Online]. Available: https://www.ducker.com/news-insights/ducker-worldwide-study-aluminum-content-cars-public-summary. [Accessed: 25-Aug-2018].

[6] F. C. Robles-hernandez, J. M. Herrera Ramírez, and R. Mackay, *Al-Si Alloys: Automotive, Aeronautial, and Aerospace Applications*. Springer International Publishing, 2017.

[7] J. R. Davis, “Aluminum and Aluminum Alloys,” in *Alloying: Understanding the Basics*, 2001, pp. 351–416.

[8] J. G. Kaufman and E. L. Rooy, *Aluminum Alloy Castings: Properties, Processes, and Applications*. Materials Park, OH, 2004.

[9] B. S. Murty, S. A. Kori, and M. Chakraborty, “Grain refinement of aluminium and its alloys by heterogeneous nucleation and alloying,” *Int. Mater. Rev.*, vol. 47, no. 1, pp. 3–29, 2002.

[10] R. Prabhu T, “Effect of synthetic graphite and activated charcoal addition on the mechanical , microstructure and wear properties of AZ 81 Mg alloys,” *J. Mater. Res. Technol.*, vol. 5, no. 3, pp. 259–267, 2016.

[11] P. P. Bhingole and G. P. Chaudhari, “Synergy of nano carbon black inoculation and high

intensity ultrasonic processing in cast magnesium alloys," *Mater. Sci. Eng. A*, vol. 556, pp. 954–961, 2012.

[12] R. Lazarova, N. Bojanova, R. Dimitrova, I. Panov, and V. Manolov, "Influence of Nanoparticles Introducing in the Melt of Aluminum Alloys on Castings Microstructure and Properties," *Int. J. Met.*, vol. 10, no. 4, pp. 466–476, 2016.

[13] "Aluminum Alloys 101," *The Aluminum Association*, 2018. [Online]. Available: http://www.aluminum.org/resources/industry-standards/aluminum-alloys-101. [Accessed: 27-Apr-2018].

[14] "History of Aluminum," *The Aluminum Association*, 2018. [Online]. Available: http://www.aluminum.org/aluminum-advantage/history-aluminum. [Accessed: 27-Apr-2018].

[15] J. G. Kaufman, "Introduction to Aluminum Alloys and Tempers," in *Introduction to Aluminum Alloys and Tempers*, ASM International, 2000, pp. 23–37.

[16] F. Cardarelli, *Materials Handbook*, 2nd ed. Springer-Verlag, 2008.

[17] ASTM Int., "ASTM B179-17: Standard Specification for Aluminum Alloys in Ingot and Molten Forms for Castings from All Casting Processes," *ASTM B. Stand.*, 2017.

[18] A. Lombardi, "A Study of Cylinder Bore Distortion in V6 Aluminum Alloy Engine Blocks," Ryerson University, 2009.

[19] V. Kumar, "Effect of chill condition and grain refinement on the microstructure and mechanical properties of B319 aluminum alloy," The University of British Columbia, 2015.

[20] M. Warmuzek, "Introduction to Aluminum-Silicon Casting Alloys," in *Aluminum-Silicon Casting Alloys: Atlas of Microfractographs*, ASM International, 2004, pp. 1–10.

[21] J. M. Boileau, "The Effect of Solidifcation Time on the Mechanical Properties of a Cast 319 Aluminum Alloy," Wayne State University, 2000.

[22] P. Marchwica, J. H. Sokolowski, and W. T. Kierkus, "Fraction solid evolution characteristics of AlSiCu alloys - dynamic baseline approach," *J. Achiev. Mater. Manuf. Eng.*, vol. 47, no. 2, pp. 115–136, 2011.

[23] M. G. Kalhapure and P. M. Dighe, "Impact of Silicon Content on Mechanical Properties of Aluminum Alloys," *Int. J. Sci. Res.*, vol. 4, no. 6, pp. 38–40, 2015.

[24] The University of Cambridge, “Phase Diagrams,” 2018. [Online]. Available: https://www.doitpoms.ac.uk/miclib/phase_diagrams.php. [Accessed: 22-May-2018].

[25] D. S. MacKenzie and G. E. Totten, *Analytical Characterization of Aluminum, Steel and Superalloys*. CRC Press (Taylor & Francis Group), 2006.

[26] M. M. Haque, “Effects of strontium on the structure and properties of aluminium-silicon alloys,” *J. Mater. Process. Technol.*, vol. 55, pp. 193–198, 1995.

[27] S. Hegde and K. N. Prabhu, “Modification of eutectic silicon in Al – Si alloys,” *J. Mater. Sci.*, vol. 43, pp. 3009–3027, 2008.

[28] E. Ogris, A. Wahlen, H. Lüchinger, and P. J. Uggowitzer, “On the silicon spheroidization in Al-Si alloys,” *J. Light Met.*, vol. 2, no. 4, pp. 263–269, 2002.

[29] S. G. Shabestari and H. Moemeni, “Effect of copper and solidification conditions on the microstructure and mechanical properties of Al-Si-Mg alloys.pdf,” *J. Mater. Process. Technol.*, vol. 153–154, pp. 193–198, 2004.

[30] C.-T. Wu, S.-L. Lee, M.-H. Hsieh, and J.-C. Lin, “Effects of Cu content on microstructure and mechanical properties of Al-14.5Si-0.5Mg alloy,” *Mater. Charact.*, vol. 61, pp. 1074–1079, 2010.

[31] C. Cloutier, J. Jones, and J. Allison, “The Effect of Copper Level and Solidification Rate on the Aging Behavior of a 319-Type Cast Aluminum Alloy,” *SAE Tech. Pap. Ser.*, no. 2000-01–0759, 2000.

[32] Z. Li, A. M. Samuel, F. H. Samuel, C. Ravindran, and S. Valtierra, “Effect of alloying elements on the segregation and dissolution of CuAl2 phase in Al-Si-Cu 319 alloys,” *J. Mater. Sci.*, vol. 38, no. 6, pp. 1203–1218, 2003.

[33] L. F. Mondolfo, *Aluminum Alloys: Structure and Properties*, 1st ed. Butterworth-Heinemann, 1976.

[34] L. A. Narayanan, F. H. Samuel, and J. E. Gruzleski, “Crystallization behavior of iron-containing intermetallic compounds in 319 aluminium alloy,” *Met. Mat. Trans. A*, vol. 25, pp. 1761–1773, 1994.

[35] A. Hetke, “Aluminum Casting Quality in Alloy 356 Engine Components,” *Trans. Am. Foundrymen’s Soc.*, no. 102, p. 367, 1995.

[36] J. A. Taylor, “Iron-containing intermetallic phases in Al-Si based casting alloys,” *Procedia Mater. Sci.*, vol. 1, pp. 19–33, 2012.

[37] J. A. Taylor, “The Effect of Iron in Al-Si Casting Alloys,” in *35th Australian Foundry Institute National Conference*, 2004, pp. 148–157.

[38] J. Asensio-Lozano and G. Vander Voort, “The Al-Si Phase Diagram,” *Microsc. Microanal.*, vol. 5, no. 1, 2009.

[39] M. W. Meredith, J. Worth, and R. Hamerton, “Intermetallic Phase Selection during Solidification of Al-Fe-Si(-Mg) Alloys,” *Mater. Sci. Forum*, vol. 396–402, pp. 107–112, 2002.

[40] J. Y. Hwang, H. W. Doty, and M. J. Kaufman, “Crystallographic studies on the iron-containing intermetallic phases in the 319-type aluminium casting alloys,” *Philos. Mag.*, vol. 88, no. 4, pp. 607–619, 2008.

[41] M. Tash, F. H. Samuel, F. Mucciardi, and H. W. Doty, “Effect of metallurgical parameters on the hardness and microstructural characterization of as-cast and heat-treated 356 and 319 aluminum alloys,” *Mater. Sci. Eng. A*, vol. 443, no. 1–2, pp. 185–201, 2007.

[42] J. Y. Hwang, H. W. Doty, and M. J. Kaufman, “The effects of Mn additions on the microstructure and mechanical properties of Al-Si-Cu casting alloys,” *Mater. Sci. Eng. A*, vol. 488, no. 1–2, pp. 496–504, 2008.

[43] A. Thirugnanam, K. Sukumaran, U. T. S. Pillai, K. Raghukandan, and B. C. Pai, “Effect of Mg on the fracture characteristics of cast Al-7Si-Mg alloys,” *Mater. Sci. Eng. A*, vol. 445–446, pp. 405–414, 2007.

[44] A. Mandal, N. Chippa, K. Jayasankar, and P. S. Mukherjee, “Effect of high magnesium content on microstructure of Al – 7Si alloy,” *Mater. Lett.*, vol. 117, pp. 168–170, 2014.

[45] P. Ouellet and F. H. Samuel, “Effect of Mg on the ageing behaviour of Al-Si-Cu 319 type aluminium casting alloys,” *J. Mater. Sci.*, vol. 34, no. 19, pp. 4671–4697, 1999.

[46] A. M. Samuel and F. H. Samuel, “Modification of iron intermetallics by magnesium and strontium in Al-Si alloys,” *Int. J. Cast Met. Res.*, vol. 10, no. 3, pp. 147–157, 1997.

[47] J. Y. Hwang, R. Banerjee, H. W. Doty, and M. J. Kaufman, “The effect of Mg on the structure and properties of Type 319 aluminum casting alloys,” *Acta Mater.*, vol. 57, no. 4,

pp. 1308–1317, 2009.

[48] A. M. Samuel, H. W. Doty, S. Valtierra, and F. H. Samuel, “Effect of Mg addition of microstructure of 319 type alloys,” *Int. J. Cast Met. Res.*, vol. 26, no. 6, pp. 354–363, 2013.

[49] A. Abedi, M. Shahmiri, B. Amir Esgandari, and B. Nami, “Microstructural Evolution during Partial Remelting of Al-Si Alloys Containing Different Amounts of Magnesium,” *J. Mater. Sci. Technol.*, vol. 29, no. 10, pp. 971–978, 2013.

[50] Q. Li, B. Li, J. Li, T. Xia, Y. Lan, and T. Guo, “Effects of the addition of Mg on the microstructure and mechanical properties of hypoeutectic Al-7%Si alloy,” *Int. J. Met.*, vol. 11, no. 4, pp. 823–830, 2017.

[51] S. X. Ji, D. Watson, Y. Wang, M. White, and Z. Y. Fan, “Effect of Ti Addition on Mechanical Properties of High Pressure Die Cast Al-Mg-Si Alloys,” *Mater. Sci. Forum*, vol. 765, pp. 23–27, 2013.

[52] L. Bäckerud, G. Chai, and J. Tamminen, *Solidification Characteristics of Aluminum Alloys, Volume 2: Foundry Alloys*. American Foundrymen’s Society, Inc., 1990.

[53] T. Morinaga, T. Takahashi, and T. Saga, “Effects of zinc on the properties of Al-Si-Cu die-casting alloys,” *Light Met.*, vol. 17, no. 5, pp. 291–297, 1967.

[54] L. Arnberg and L. Bäckerud, *Solidification Charcteristics of Aluminum Alloys, Volume 3: Dendrite Coherency*. Des Plaines, Illinois: American Foundrymen’s Society, Inc., 1996.

[55] F. H. Samuel, A. M. Samuel, P. Ouellet, and H. W. Doty, “Effect of Mg and Sr additions on the formation of intermetallics in Al-6 wt pct Si-3.5 wt pct Cu-(0.45) to (0.8) wt pct Fe 319-type alloys,” *Metall. Mater. Trans. A*, vol. 29, no. December, pp. 2871–2884, 1998.

[56] A. M. Samuel, J. Gauthier, and F. H. Samuel, “Microstructural aspects of the dissolution and melting of Al2Cu phase in Al-Si alloys during solution heat treatment,” *Metall. Mater. Trans. A*, vol. 27, pp. 1785–1798, 1996.

[57] E. Vandersluis, “Influence of Soldification Parameters on the Thermal Conductivity of Cast A319 Aluminum Alloy,” Ryerson University, 2016.

[58] S. G. Shabestari and S. Ghodrat, “Assessment of modification and formation of intermetallic compounds in aluminum alloy using thermal analysis,” *Mater. Sci. Eng. A*,

vol. 467, pp. 150–158, 2007.

[59] M. E. Farina, P. Bell, C. R. F. Ferreira, and B. A. Dedavid, “Effects of Solidification Rate in the Microstructure of Al-Si5Cu3 Aluminum Cast Alloy,” *Mater. Res.*, vol. 20, pp. 273–278, 2017.

[60] E. J. Martinez D., M. A. Cisneros G., S. Valtierra, and J. Lacaze, “Effects of strontium and cooling rate upon eutectic temperatures of A319 aluminum alloy,” *Scr. Mater.*, vol. 52, pp. 439–443, 2005.

[61] A. Lombardi, C. Ravindran, and R. Mackay, “Application of the Billet Casting Method to Determine the Onset of Incipient Melting of 319 Al Alloy Engine Blocks,” *J. Mater. Eng. Perform.*, vol. 24, no. June, pp. 2179–2184, 2015.

[62] T. V. R. Rao, *Metal Casting: Principles and Practice*. New Delhi: New Age International, 2003.

[63] J. Campbell, *Castings*, 2nd ed. Oxford, Uk: Butterworth-Heinemann, 2003.

[64] F. Farhang Mehr, C. Reilly, S. Cockcroft, D. Maijer, and R. MacKay, “Effect of chill cooling conditions on cooling rate, microstructure and casting/chill interfacial heat transfer coefficient for sand cast A319 alloy,” *Int. J. Cast Met. Res.*, vol. 27, no. 5, pp. 288–300, 2014.

[65] G. E. Byczynski, W. T. Kierkus, D. O. Northwood, D. Penrod, and J. Sokolowski, “The Effect of Quench Rate on Mechanical Properties of 319 Aluminum Alloy Castings,” *Mater. Sci. Forum*, vol. 217–222, pp. 783–788, 1996.

[66] X. Hu, F. Ai, and H. Yan, “Influences of pouring temperature and cooling rate on microstructure and mechanical properties of casting Al-Si-Cu aluminum alloy,” *Acta Metall. Sin. Lett.*, vol. 25, no. 4, pp. 272–278, 2012.

[67] J. Pavlovic-Krstic, R. Bähr, G. Krstic, and S. Putic, “The effect of mould temperature and cooling conditions on the size of secondary dendrite arm spacing in Al-7Si-3Cu alloy,” *Metal. - J. Metall.*, vol. 15, no. 2, pp. 105–113, 2009.

[68] J. M. Boileau and J. E. Allison, “The effect of solidification time and heat treatment on the fatigue properties of a cast 319 aluminum alloy,” *Metall. Mater. Trans. A*, vol. 34, no. 9, pp. 1807–1820, 2003.

[69] W. D. J. Callister and D. G. Rethwisch, *Material Science and Engineering An Introduction*, 9th ed. Wiley, 2014.

[70] J. E. Gruzleski, *Microstructure Development During Metalcasting*. Montreal, Canada: American Foundrymen's Society, Inc., 1999.

[71] K. P. Shah, "Practical Maintenance: Crystallization." [Online]. Available: http://practicalmaintenance.net/?p=1085. [Accessed: 15-Jun-2018].

[72] J. A. Spittle and S. Sadli, "Effect of alloy variables on grain refinement of binary aluminium alloys with Al – Ti – B," *Mater. Sci. Technol.*, vol. 11, no. 6, pp. 533–537, 1995.

[73] T. Chandrashekar, M. K. Muralidhara, K. T. Kashyap, and P. Raghothama Rao, "Effect of growth restricting factor on grain refinement of aluminum alloys," *Int. J. Adv. Manuf. Technol.*, vol. 40, pp. 234–241, 2009.

[74] C. Zhong-wei, H. E. Zhi, and J. I. E. Wan-qi, "Growth restriction effects during solidification of aluminium alloys," *Trans. Nonferrous Met. Soc. China*, vol. 19, pp. 410–413, 2009.

[75] G. K. Sigworth and T. A. Kuhn, "Grain Refining of Aluminum Casting Alloys," vol. 067, no. 02, pp. 1–12, 2001.

[76] P. S. Mohanty and J. E. Gruzleski, "Grain refinement mechanisms of hypoeutectic Al-Si alloys," *Acta Mater.*, vol. 44, no. 9, pp. 3749–3760, 1996.

[77] V. Kumar and L. Bichler, "Effect of TiC Powder Addition on the Grain Refinement Response of B319 Aluminium Alloy," *Light Met. 2014*, pp. 207–211, 2014.

[78] M. J. Mehl *et al.*, "The AFLOW Library of Crystallographic Prototypes: Part 1," *Comput. Mater. Sci.*, vol. 136, pp. S1–S828, 2017.

[79] T. E. Quested, "Understanding mechanisms of grain refinement of aluminium alloys by inoculation," *Mater. Sci. Technol.*, vol. 20, no. 11, pp. 1357–1369, 2004.

[80] T. B. Massalski, H. Okamoto, P. R. Subramanian, and L. Kacprzak, Eds., *Binary Alloy Phase Diagrams*, 2nd ed. Materials Park, OH: ASM International, 1990.

[81] K. Kashyap and T. Chandrashekar, "Effects and mechanisms of grain refinement in aluminium alloys," *Bull. Mater. Sci.*, vol. 24, no. 4, pp. 345–353, 2001.

[82] Z. Fan *et al.*, "Grain refining mechanism in the Al/Al–Ti–B system," *Acta Mater.*, vol. 84,

pp. 292–304, 2015.

[83] X. Wang, Z. Liu, W. Dai, and Q. Han, “On the Understanding of Aluminum Grain Refinement by Al-Ti-B Type Master Alloys,” *Metall. Mater. Trans. B Process Metall. Mater. Process. Sci.*, vol. 46, no. 4, pp. 1620–1625, 2015.

[84] K. Pasciak and G. K. Sigworth, “Role of Alloy Composition in Grain refining of 319 Alloy,” *AFS Trans.*, vol. 109, pp. 567–577, 2001.

[85] S. G. Shabestari and M. Malekan, “Assessment of the effect of grain refinement on the solidification characteristics of 319 aluminum alloy using thermal analysis,” *J. Alloys Compd.*, vol. 492, pp. 134–142, 2010.

[86] G. K. Sigworth and M. M. Guzowski, “Grain refiner for aluminum containing silicon,” US5055256A, 1991.

[87] D. Qiu, J. A. Taylor, M.-X. Zhang, and P. M. Kelly, “A mechanism for the poisoning effect of silicon on the grain refinement of Al-Si alloys,” *Acta Mater.*, vol. 55, no. 4, pp. 1447–1456, 2007.

[88] T. E. Quested, A. T. Dinsdale, A. L. Greer, T. E. Quested, A. T. Dinsdale, and A. L. Greer, “Thermodynamic evidence for a poisoning mechanism in the Al – Si – Ti system,” *Mater. Sci. Technol.*, vol. 22, no. 9, pp. 1126–1134, 2013.

[89] S. A. Kori, B. S. Murty, and M. Chakraborty, “Development of an efficient grain refiner for Al-7Si alloy,” *Mater. Sci. Eng. A*, vol. 280, no. 1, pp. 58–61, 2000.

[90] A. Cibula, “Discussion of ‘the mechanisms of grain refinement in dilute aluminum alloys,’” *Metall. Mater. Trans. A*, vol. 3, no. March, pp. 751–753, 1972.

[91] Y. X. Li, J. D. Hu, H. Y. Wang, Z. X. Guo, and A. N. Chumakov, “Thermodynamic and lattice parameter calculation of TiCx produced from Al-Ti-C powders by laser igniting self-propagating high-temperature synthesis,” *Mater. Sci. Eng. A*, vol. 458, pp. 235–239, 2007.

[92] W. W. Ding, J. T. Zhu, W. J. Zhao, and T. D. Xia, “An Investigation on Grain Refinement Mechanism of Master Alloys Al-Ti, Al-TiC and Al-Ti-C Toward Pure Aluminum,” *Adv. Mater. Res.*, vol. 652–654, pp. 1072–1075, 2013.

[93] B. T. Gezer, F. Toptan, S. Daglilar, and I. Kerti, “Production of Al-Ti-C Grain Refiners with

the Addition of Elemental Carbon and K2TiF6," in *Light Metals 2011*, 2011, pp. 821–825.

[94] G. S. V. Kumar, B. S. Murty, and M. Chakraborty, "Grain refinement response of LM25 alloy towards Al-Ti-C and Al-Ti-B grain refiners," *J. Alloys Compd.*, vol. 472, no. 1–2, pp. 112–120, 2009.

[95] G. S. V. Kumar, B. S. Murty, and M. Chakraborty, "Development of Al – Ti – C grain refiners and study of their grain refining efficiency on Al and Al – 7Si alloy," *J. Alloys Compd.*, vol. 396, pp. 143–150, 2005.

[96] H. Ding, X. Liu, L. Yu, and G. Zhao, "The influence of forming processes on the distribution and morphologies of TiC in Al – Ti – C master alloys," *Scr. Mater.*, vol. 57, pp. 575–578, 2007.

[97] A. Lombardi, F. D. Elia, C. Ravindran, B. S. Murty, and R. Mackay, "Analysis of the secondary phases in the microstructure of 319 type Al alloy engine blocks using electron microscopy and nanoindentation," *Trans. Indian Inst. Met.*, vol. 64, no. April, pp. 7–11, 2011.

[98] M. Qian and P. Cao, "Discussions on grain refinement of magnesium alloys by carbon inoculation," *Scr. Mater.*, vol. 52, no. 5, pp. 415–419, 2005.

[99] E. F. Emley, *Principles of Magnesium Technology*. Oxford: Pergamon Press, 1966.

[100] J. Du, M. Wang, M. Zhou, and W. Li, "Evolutions of grain size and nucleating particles in carbon-inoculated Mg-3% Al alloy," *Journal of Alloys and Compounds*, vol. 592. pp. 313–318, 2014.

[101] Y. Huang, K. U. Kainer, and N. Hort, "Mechanism of grain refinement of Mg – Al alloys by SiC inoculation," *Scr. Mater.*, vol. 64, no. 8, pp. 793–796, 2011.

[102] M. Mansoor and M. Shahid, "Carbon nanotube-reinforced aluminum composite produced by induction melting," *Journal of Applied Research and Technology*, vol. 14, no. 4. pp. 215–224, 2016.

[103] A. B. Elshalakany, T. A. Osman, A. Khattab, B. Azzam, and M. Zaki, "Microstructure and Mechanical Properties of MWCNTs Reinforced A356 Aluminum Alloys Cast Nanocomposites Fabricated by Using a Combination of Rheocasting and Squeeze Casting Techniques," *J. Nanomater.*, vol. 2014, pp. 1–14, 2014.

[104] L. Rong, L. Yong, and Z. Guangming, “Mechanical Properties Affection of Carbon Powder Added into Casting Aluminum Alloy,” *Appl. Mech. Mater.*, vol. 697, no. 2, pp. 27–30, 2015.

[105] I.-J. Shon, “Effects of Direct Current on the Wetting between Molten Al and a Graphite Substrate,” *Korean J. Met. Mater.*, vol. 56, no. 7, pp. 505–510, 2018.

[106] M. Yang and V. D. Scott, “Carbide formation in a carbon fibre reinforced aluminum composite,” *Carbon N. Y.*, vol. 29, no. 7, pp. 877–879, 1991.

[107] M. S. Sidhu, C. M. Bishop, and M. V. Kral, “Formation of aluminium carbide by cast iron and liquid aluminium interaction,” *Int. J. Cast Met. Res.*, vol. 27, no. 6, pp. 321–328, 2014.

[108] J. V. Shugart, R. C. Scherer, and R. L. Penn, “Aluminum-carbon compositions,” US9273380B2, 2016.

[109] Y. Ijichi and K. Ohshima, “Al alloy containing Cu and C and its manufacturing method,” US2017/0253949A1, 2017.

[110] International Carbon Black Association, “Carbon Black User’s Guide,” *International Carbon Black Association*. p. 36, 2016.

[111] J. Robertson, “Amorphous carbon,” *Adv. Phys.*, vol. 35, no. 4, pp. 317–374, 1986.

[112] G. S. Upadhyaya, *Powder Metallurgy Technology*. Cambridge International Publishing Company, 2002.

[113] M. N. Rahaman, *Ceramic processing and sintering*. CRC Press (Taylor & Francis Group), 2003.

[114] S. J. L. Kang, R. Bordia, E. Olevsky, and D. Bouvard, Eds., *Advances in Sintering Science and Technology 2*. Hoboken, NJ, USA: John Wiley & Sons Inc., 2012.

[115] Z. Fu *et al.*, “The SPS Process : Characterization and Fundamental Investigations,” in *Pulse Electric Current Synthesis and Processing of Materials*, Z. A. Munir, M. Ohyanagi, and M. Tokita, Eds. The American Ceramics Society, 2006, pp. 3–21.

[116] R. A. Prasad, “Spark Plasma Sintering of Cerium Dioxide and its Composites,” The University of British Columbia Okanagan, 2017.

[117] M. Tokita, “Mechanism of spark plasma sintering,” in *Proceedings of The International*

Symposium on Microwave, Plasma and Thermochemical Processing of Advanced Materials, 1997, pp. 69–76.

[118] T. Yoshioka, K. Sato, S. Tanaka, S. Yamada, and Y. Makino, “Sintering Behavior of Aluminum Alloy-Carbon Composite by SPS,” in *Pulse electric current synthesis and processing materials*, American Ceramic Society, 2006, pp. 89–99.

[119] I.-S. Ahn, S.-Y. Bae, H.-J. Cho, C.-J. Kim, and D.-K. Park, “Synthesis of Titanium Carbide by Heat Treatment of TiH 2 and Carbon Black Powders,” *Mater. Sci. Forum*, vol. 534–536, pp. 225–228, 2007.

[120] R. Pérez-Bustamante *et al.*, “AA2024-CNTs composites by milling process after T6-temper condition,” *J. Alloys Compd.*, vol. 536, no. SUPPL.1, pp. S17–S20, 2012.

[121] A. Azad and L. Bichler, “Effect of a novel Al-SiC grain refiner on the microstructure and properties of AZ91E magnesium alloy,” *Int. J. Met.*, vol. 7, no. 4, pp. 49–59, 2013.

[122] T. A. Davis, L. Bichler, F. D’Elia, and N. Hort, “Effect of TiBor on the grain refinement and hot tearing susceptibility of AZ91D magnesium alloy,” *J. Alloys Compd.*, vol. 759, pp. 70–79, 2018.

[123] A. K. Dahle, P. A. Tondel, C. J. Paradies, and L. Arnberg, “Effect of Grain Refinement on the Fluidity of Two Commercial AI-Si Foundry Alloys,” *Metall. Mater. Trans. A*, vol. 27A, pp. 2305–2313, 1996.

[124] M. Di Sabatino, “Fluidity of Aluminium Foundry Alloys,” Norwegian University of Science and Technology, 2005.

[125] D. Caliari, G. Timelli, F. Bonollo, P. Amalberto, and P. Giordano, “Fluidity of aluminium foundry alloys: Development of a testing procedure,” *Metall. Ital.*, vol. 107, no. 6, pp. 11–18, 2015.

[126] ASTM Int., “ASTM E384: Standard Test Method for Knoop and Vickers Hardness of Materials,” *ASTM B. Stand.*, 2012.

[127] ASTM Int., “ASTM B557M-15: Standard Test Methods for Tension Testing Wrought and Cast Aluminum- and Magnesium-Alloy Products (Metric),” *ASTM B. Stand.*, 2015.

[128] ASTM Int., “ASTM E23-16b: Standard Test Methods for Notched Bar Impact Testing of Metallic Materials,” *ASTM B. Stand.*, 2016.

[129] D. M. Stefanescu, “Thermal Analysis — Theory and Applications in Metalcasting,” *Int. J. Met.*, vol. 9, no. 1, 2015.

[130] K. Tacke, A. Grill, K. Miyazawa, and K. Schwerdtfeger, “Macrosegregation in strand cast steel: computation of concentration profiles with a diffusion model,” *Arch. Eisenhuttenwes*, vol. 52, no. 1, pp. 15–20, 1981.

[131] C.-M. Raihle, P. Sivensson, M. Tukiainen, and H. Fredriksson, “Improving Inner Quality in Continuously Cast Billets - Comparison Between Mold Electromagnetic Stirring and Thermal Soft Reduction,” *Ironmak. Steelmak.*, vol. 21, no. 6, pp. 487–495, 1994.

[132] N. N. Prokhorov and M. P. Bochai, “Mechanical properties of aluminum alloys in the temperature range of solidification in welding,” *Svarochnoe Proizv.*, vol. 2, pp. 1–2, 1958.

[133] L. Bichler, “Phenomenological studies of hot tearing during solidification of magnesium alloys,” Ryerson University, 2009.

[134] D. Sediako, O. Sediako, and K. J. Lin, “Some Aspects of Thermal Analysis and Technology Upgrading in Steel Continuous Casting,” *Can. Metall. Q.*, vol. 38, no. 5, pp. 377–385, 1999.

[135] ASTM Int., “ASTM E112-13: Standard Test Methods for Determining Average Grain Size,” *ASTM B. Stand.*, 2013.

[136] T. Peng and I. Chang, “Mechanical alloying of multi-walled carbon nanotubes reinforced aluminum composite powder,” *Powder Technol.*, vol. 266, pp. 7–15, 2014.

[137] M. Raviathul Basariya, V. C. Srivastava, and N. K. Mukhopadhyay, “Microstructural characteristics and mechanical properties of carbon nanotube reinforced aluminum alloy composites produced by ball milling,” *Mater. Des.*, vol. 64, pp. 542–549, 2014.

[138] A. P. S. Chauhan and K. Chawla, “Comparative studies on Graphite and Carbon Black powders, and their dispersions,” *J. Mol. Liq.*, vol. 221, pp. 292–297, 2016.

[139] S. Park *et al.*, “Colloidal suspensions of highly reduced graphene oxide in a wide variety of organic solvents.,” *Nano Lett.*, vol. 9, no. 4, pp. 1593–1597, 2009.

[140] M. M. Rahman, H. Younes, N. Subramanian, and A. Al Ghaferi, “Optimizing the Dispersion Conditions of SWCNTs in Aqueous Solution of Surfactants and Organic Solvents,” *J. Nanomater.*, vol. 2014, 2014.

[141] J. Hilding, E. A. Grulke, Z. George Zhang, and F. Lockwood, “Dispersion of Carbon Nanotubes in Liquids,” *J. Dispers. Sci. Technol.*, vol. 24, no. 1, pp. 1–41, 2003.

[142] B. B. He, *Two-Dimensional X-Ray Diffraction*. Wiley, 2009.

[143] J. Goldstein *et al.*, *Scanning Electron Microscopy and X-Ray Microanalysis*, 3rd ed. New York: Springer, 2007.

[144] D. B. Williams and C. B. Carter, *Transmission Electron Microscopy*. Springer, 2009.

[145] T. Davis, L. Bichler, D. Sediako, and L. Balogh, “Solidification analysis of grain refined AZ91D magnesium alloy via neutron diffraction,” in *Magnesium Technology 2018*, 2018, pp. 425–428.

[146] Y. Mirgorod, S. Emelianov, V. Fedosjuk, and S. Bolshanina, “Influence of Size Effects on the Properties of Processed Iron Ore and Schungite Rock,” *J. Nano-and Electron. Phys.*, vol. 8, no. 2, pp. 1–6, 2016.

[147] Z. Q. Li, C. J. Lu, Z. P. Xia, Y. Zhou, and Z. Luo, “X-ray diffraction patterns of graphite and turbostratic carbon,” *Carbon N. Y.*, vol. 45, pp. 1686–1695, 2007.

[148] A. M. Locci, A. Cincotti, S. Todde, R. Orrù, and G. Cao, “A methodology to investigate the intrinsic effect of the pulsed electric current during the spark plasma sintering of electrically conductive powders,” *Sci. Technol. Adv. Mater.*, vol. 11, pp. 1–13, 2010.

[149] N. Chawake, L. D. Pinto, A. K. Srivastav, K. Akkiraju, B. S. Murty, and R. S. Kottada, “On Joule heating during spark plasma sintering of metal powders,” *Scr. Mater.*, vol. 93, pp. 52–55, 2014.

[150] Y. Koizumi, T. Tanaka, Y. Minamino, N. Tsuji, K. Mizuuchi, and Y. Ohkanda, “Densification and Structural Evolution in Spark Plasma Sintering Process of Mechanically Alloyed Nanocrystalline Fe – 23Al – 6C Powder,” *Mater. Trans.*, vol. 44, no. 8, pp. 1604–1612, 2003.

[151] T. B. Holland, U. Anselmi-Tamburini, D. V. Quach, T. B. Tran, and A. K. Mukherjee, “Effects of local Joule heating during the field assisted sintering of ionic ceramics,” *J. Eur. Ceram. Soc.*, vol. 32, pp. 3667–3674, 2012.

[152] G. Lalet, H. Kurita, T. Miyazaki, A. Kawasaki, and J.-F. Silvain, “Microstructure of a carbon fiber-reinforced aluminum matrix composite fabricated by spark plasma sintering

in various pulse conditions," *J. Mater. Sci.*, vol. 49, pp. 3268–3275, 2014.

[153] M. Malekan and S. G. Shabestari, "Effect of Grain Refinement on the Dendrite Coherency Point during Solidification of the A319 Aluminum Alloy," *Metall. Mater. Trans. A*, vol. 40A, no. 12, pp. 3196–3203, 2009.

[154] A. K. Dahle, P. A. Tøndel, C. J. Paradies, and L. Arnberg, "Effect of grain refinement on the fluidity of two commercial Al-Si foundry alloys," *Metall. Mater. Trans. A*, vol. 27, no. 8, pp. 2305–2313, 1996.

[155] C. R. J. Loper, "Fluidity of Aluminum-Silicon Casting Alloys," *AFS Trans.*, vol. 100, pp. 533–538, 1992.

[156] F. R. Mollard, M. C. Flemings, and E. F. Niyama, "Aluminum Fluidity in Casting," *J. Miner. Met. Mater. Soc.*, vol. 39, no. 11, p. 34, 1987.

[157] M. R. Sheshradri and A. Ramachandran, "Casting fluidity and fluidity of aluminum and its alloys," *Mod. Cast.*, vol. 21, pp. 110–122, 1965.

[158] S. Gowri and F. H. Samuel, "Effect of alloying elements on the solidification characteristics and microstructure of Al-Si-Cu-Mg-Fe 380 alloy," *Metall. Mater. Trans. A*, vol. 25, no. 2, pp. 437–448, 1994.

[159] G. Lang, "Casting properties and surface tension of aluminum and binary aluminum alloys," *Aluminum*, vol. 48, no. 10, pp. 664–672, 1972.

[160] G. E. Dieter, *Mechanical Metallurgy*, SI Metric. McGraw Hill Education, 1988.

[161] B. Jung, H. Lee, and H. Park, "International Journal of Solids and Structures Effect of grain size on the indentation hardness for polycrystalline materials by the modified strain gradient theory," *Int. J. Solids Struct.*, vol. 50, no. 18, pp. 2719–2724, 2013.

[162] H. M. Medrano-prieto, C. G. Garay-reyes, and C. D. Gómez-esparza, "Evolution of Microstructure in Al-Si-Cu System Modified with a Transition Element Addition and its Effect on Hardness," vol. 19, pp. 59–66, 2016.